Controlling Charge Carrier Trapping in Polymeric Semiconductors

Connecting Morphology to Device Behavior

Dissertation

zur Erlangung des Grades

„Doctor rerum naturalium (Dr. rer. nat.)“

im Promotionsfach Chemie

am Fachbereich Chemie, Pharmazie, Geographie und Geowissenschaften

der Johannes Gutenberg-Universität Mainz

und

im Arbeitskreis Molekulare Elektronik

am Max-Planck-Institut für Polymerforschung

von

Alexander Kunz

geboren am 05. Mai 1987 in Karaganda/Kasachstan

Mainz, Januar 2021

Erstprüfer: **Prof. Dr. P.W.M. Blom**

Zweitprüfer: **Prof. Dr. R. Zentel**

Betreuer: **Dr. J. J. Michels**

Dekan: **Univ.-Prof. Dr. Tobias Reich**

Tag der mündlichen Prüfung: 04. März 2021

This thesis is dedicated to my children.
You will never outgrow my heart.

Declaration

I hereby declare that except where specific reference is made to the work of others, the contents of this dissertation are original and have not been submitted in whole or in part for consideration for any other degree or qualification in this, or any other university. This dissertation is my own work and contains nothing which is the outcome of work done in collaboration with others, except as specified in the text and Acknowledgements.

Hiermit deklariere ich, dass die vorliegende Arbeit und der Inhalt dieses Werks meine eigene Arbeit darstellen. Arbeiten anderer Personen, auch Kollaborationen, sind in den Quellenangaben, Danksagungen und im Text als solche gekennzeichnet. Weiterhin wurde diese Arbeit und Teile dieser an keiner anderen Universität und zu keinem anderen als dem hier genannten zu errreichenden Grad eingereicht.

Alexander Kunz
March 2021

Acknowledgements

I am deeply grateful to my director Prof. Dr. Paul Blom and my supervisor Dr. Jasper Michels for their invaluable support and advice throughout my whole time at the Max Planck Institute for Polymer Research. Prof. Blom gave me the opportunity to study in this outstanding scientific field of polymeric semiconductors. His tremendous knowledge and help motivated me to deepen my own knowledge in this field. Dr. Michels inspired me almost daily to think "out of the box" and gave enormous personal support as a mentor and friend. His unique and positive way of encouraging me was extremely helpful. It was always a pleasure to work for and with him and Prof. Blom.

I gratefully acknowledge the Max Planck Society and especially the Max Planck institute for Polymer Research for giving me the opportunity to advance my academic studies in this renowned community. Also I would like to express my gratitude to the Molecular Electronics department members with whom we overcame many technical and formal obstacles. To name a few: Petra Pausch, Frank K., Christian B., Hans-Jürgen G., Michelle B. ...

Furthermore, I acknowledge Prof. Dr. Rudolf Zentel from the Johannes Gutenberg University for being my university supervisor. Also, I would like to thank Prof. Dr. T. B. and Prof. Dr. K. H. for being part of the defense committee.

Special acknowledgment goes to my colleagues Elham, Hamed, Anielen, Ann-Kathrin, Irina, Leona, Kai and Deepthi with whom I had a great time at the MPIP and also in my private life. Thank you for cheering me on, the little discussions, the wonderful food and cakes, the great time at conferences and after work in the institute as well as at home.

Words cannot describe how much I want to thank my beloved wife Regina for her endless support, her enormous patience and her "non-scientific" contributions to my well-being. She is my complementary counterpart and a lovely mother to my children which were born during the writing period of this thesis. Thank you so much.

Finally, I would like to say thank you to my parents and my brother for their wholehearted support as a family. Without them I would have never taken the academic path.

Abstract

Performance and efficiency of polymeric optoelectronic devices strongly depends on morphology, mixing behavior and purity of the conjugated polymers used. The transport behavior of electric charge carriers - holes and electrons - can be directly tuned by these properties. It also has great impact on loss processes in polymeric light emitting diodes (PLED) and polymeric photovoltaic devices (OPV). Typically, charge transport in a conjugated polymer is unbalanced, e.g. hole transport along the backbone of a conjugated polymer is of space-charge-limited nature and *trap free*. Electron transport in principle follows the same mechanism, but in contrast to hole transport it suffers trapping of electrons in localized energetic states within the energy band gap of the conjugated polymer, which leads to an overall reduction of electron transport by more than three orders of magnitude. The disparity of hole and electron transport leads to a severe loss process in both PLEDs and OPVs: excitons (bound electron-hole pairs) are generated close to the cathode contact and decay non-radiatively by transfer of their recombination energy to the metallic contact via dipole-dipole interaction mechanism. Additionally, non-radiative trap-assisted recombination occurs as another loss process.

In order to address the loss processes in conjugated polymers, the work in this thesis is focused on tuning the charge carrier transport in conjugated polymers by blending them with other conjugated and non-conjugated polymers. The **first chapter** introduces the work and discusses on the physical and chemical background of conjugated polymers, electrical devices and the phase dynamics of polymer mixtures that are relevant for comprehension.

In the **second chapter** a discussion on the role of morphology of MEH-PPV:PVK blends on charge transport properties in hole and electron only devices. It is demonstrated how morphology evolves from phase dynamics of the different polymer blends and how the intimacy of the blend constituents affects the charge transport properties in solution processed active layers of hole only and electron only devices. It is found that weak segregation of the blend components takes place into coexisting MEH-PPV-rich and PVK-rich phases. Ultimately, it is demonstrated that for MEH-PPV:PVK thin film devices with weight ratios of 1:9 equilibrated electron and hole transport is observed as the negative effect of trapped

electrons is effectively eliminated due to dilution of the low band gap polymer MEH-PPV in the high band gap polymer PVK.

To strengthen and broaden the findings made in chapter 2, in **chapter 3** polystyrene is introduced as an insulating polymer into the blend system with MEH-PPV. Polystyrene is an insulator with an even higher band gap than PVK and available in a wide variety of molecular weights and suitable to prove the generality of the previously reported performance improvement by dilution of the conjugated polymer and its electronic trap states, also in comparison to the MEH-PPV:PVK blends mentioned in chapter 2. First, the third chapter focuses on calculating the phase dynamics in order to qualitatively predict mixing behavior of the MEH-PPV:PS blend when solution processed. Second, it compares the morphological outcome and electronic performance. Two distinct cases are presented and analyzed. The first case , a fully phase separating blend MEH-PPV with a molecular weight of 354 kg/mol and polystyrene with a molecular weight of 35 kg/mol, with no improvement in electronic performance of light emitting devices, independent from weight ratio between the two polymers. The second case, again the same MEH-PPV but in a blend with a low molecular weight polystyrene with 1.1 kg/mol, fully miscible when spin cast from solution and showing improved electron transport properties by three orders of magnitude. Ultimately, this chapter emphasizes the importance of phase dynamics that is directly related to performance of solution processed thin film devices. It also shows that MEH-PPV based PLEDs can be doubled in efficiency by using an insulating diluent polymer such as polystyrene in a weight ratio of 1:9.

The **fourth chapter** concentrates on expanding the previous studies on other conjugated polymer blends such as BEH-PPV:PS. At first glance, BEH-PPV as compared to MEH-PPV looks very similar, but the substitution pattern of side chains is symmetric. The on chain order of BEH-PPV is increased and higher mobility of charge carriers is feasible when used in thin film devices. Lower operating voltages are possible and therefore of practical importance for improved device performance. As a first result, trap free electron transport in BEH-PPV:PS electron only devices is demonstrated successfully. However, BEH-PPV gives rise to different phase dynamics than MEH-PPV when blended with low molecular weight polystyrene. Indeed, though lateral phase separation is not observed experimentally, injection issues of positive charge carriers into BEH-PPV:PS thin films are observed. A systematic study of the origin of these injection issues on thin films of BEH-PPV:PS blends in different weight ratios is performed by Kelvin-Probe and ToF-SIMS analysis. It is revealed that not a mismatch of energetic levels, but rather a surface directed effect on the vertical composition of the blend creates preferential accumulation of insulating polystyrene on the PEDOT:PSS injection contact. Finally, by blending the PEDOT:PSS injection contact with perfluorooctane

sulfonic acid (FOS) in excess a lowering of the surface energy of the PEDOT:PSS contact is achieved. Injection issues are eliminated successfully by fabrication of hole only devices made with PEDOT:PSS:FOS hole injection contacts and BEH-PPV:PS 1:9 as active thin film. Together with the demonstration of trap free electron transport in BEH-PPV:PS 1:9 thin films promising device performances are obtained.

The **fifth chapter** discusses the role of density of structural defects of the conjugated polymer BEH-PPV on electron only device performance. More specifically, a study on electron only device performance as a function of chain end density is performed. The chain end density is seen as a critical origin of energetic trap sites for positive and negative charge carriers simultaneously. Therefore, most synthesis routes focus on creation of high molecular weight BEH-PPV in order to reduce the chain end density to rule out the possible negative effects, accepting the compromise of fairly poor solution processability. Here the electron transport properties of BEH-PPV polymers is studied in electron only devices. The molecular weight of the solution processed BEH-PPV thin films is varied in the range of two orders of magnitude in number average molecular weight, namely BEH-PPV with 52 kg/mol, 123 kg/mol and 521 kg/mol. Device performance is simulated with the extended Gaussian disorder model, where mobility, trap density and electronic disorder is analyzed. Within the chosen molecular weight range no significant change in trap density as well as transport behavior of electrons is observed. As a recommendation, the synthesis of BEH-PPV in the number molecular weight range around 100 kg/mol is proposed. An intermediate molecular weight of BEH-PPV can improve solution processability in terms of repeatability and preparation time without any effective disadvantage of increased structural defects due to increased chain end density.

Zusammenfassung

Verlustprozesse limitieren die Effizienz polymerbasierter Leuchtdioden (PLED) und Solarzellen (OPV). Sie entstehen durch eine Disparität von Loch- und Elektronentransport, wobei letzterer typischerweise drei Größenordnungen kleiner ist, da lokalisierte energetische Fallenzustände innerhalb der Bandlücke eines halbleitenden konjugierten Polymers existieren. Dies hat zur Folge, dass Rekombination von Elektronen mit Löchern strahlungsfrei über Fallenzustände oder Relaxation von Excitonen in der Nähe des Kathodenkontaktes geschehen.

Der Ladungstransport und die Verlustmechanismen können durch geeignete Wahl und Mischung halbleitender konjugierter Polymere kontrolliert und verbessert werden. Prinzipien der *Soft-Matter Dynamics*, wie Mischungsverhalten und Einstellen morphologischer

Eigenschaften werden in dieser Arbeit dazu genutzt Verlustmechanismen in halbleitenden polymerbasierten Bauteilen zu identifizieren und zu reduzieren. Es wird dabei eine Verbindung zwischen Mischungsdynamik, Morphologie und Performance optoelektronischer Bauteile hergestellt.

Im Besonderen wird die Mischungsdynamik Polyphenylenevinylene-basierter Polymere mit halbleitenden und isolierenden Polymeren, wie Polyvinylkarbazol und Polystyrol über Phasendiagramme vorausberechnet. Analysen über die Morphologie und Topologie der Dünnschichten werden hergestellt und herangezogen sowie in optoelektronischen Bauteilen praktisch erprobt. Abschließend kann durch die Verbindung von Mischungsdynamik und Bauteil-Performance gezeigt werden, dass energetische Fallenzustände innerhalb der Bandlücke halbleitender konjugierter Polymere in ihren negativen Eigenschaften neutralisiert werden können. Der Ladungstransport wird homogenisiert und die Effizienz der optoelektronischen Bauteile wird erhöht.

Table of contents

List of figures **xv**

List of tables **xvii**

1 Introduction to Polymer based Semiconductors **1**
1.1 Introduction 1
1.2 Trap-limited charge transport 8
1.3 Polymer materials for semiconductor application 12
1.4 Device Structures 13
1.5 Thermodynamics of polymer mixtures 16

2 Morphology of MEH-PPV:PVK Blends **27**
2.1 Introduction 27
2.2 Experimental 32
2.3 Results & Discussion 33
2.4 Conclusions & Outlook 45

3 Charge Carrier Trapping Controlled by Polymer Blend Phase Dynamics **47**
3.1 Introduction 47
3.2 Experimental 48
3.3 Results & Discussion 49
3.4 Conclusions 55
3.5 Appendix 57

4 Controlling compositional changes in BEH-PPV:PS Blends **61**
4.1 Introduction 61
4.2 Experimental 63
4.3 Results & Discussion 64
4.3.1 Work function modification of PEDOT:PSS injection layer by solvents 68

4.3.2 Depth profiling with ToF-SIMS 71
4.3.3 Changing hole injection properties by fluorination with perfluorooctane sulfonic acid 78
4.4 Conclusions & Outlook 81

5 Influence of chain end density on electron transport behavior in BEH-PPV 83
5.1 Introduction 83
5.1.1 Estimation of defect density caused by chain ends 84
5.2 Experimental 85
5.3 Results and Discussion 86
5.3.1 Modelling of Hole only devices with the Extended Gaussian Disorder Model 86
5.3.2 Modelling of Electron only devices with the Extended Gaussian Disorder Model 87
5.3.3 Comparison between chain end density and trap density 90
5.4 Conclusions 91

References 93

List of figures

1.1 Theoretical Model for Orbital Hybridization 2
1.2 Linear combination of atomic orbitals 3
1.3 Conjugation extension 4
1.4 Change in polymer conjugation 5
1.5 Distribution of energetic states, gaussian and exponential 8
1.6 Typical current density voltage characteristics of an organic semiconducting polymer 10
1.7 Chemical structure of poly(phenylenevinylene) based polymers 12
1.8 Chemical structure of poly(9,9-dioctylfluorene) (PFO) (a) and poly(9,9-dioctylfluorene-alt-benzothiadiazole) (F8BT) (b) as prominent blue and green emitters in PLED application 13
1.9 Chemical structure of poly(9-vinylcarbazole) PVK 13
1.10 Device stack configurations. (a) Electron only device (EOD), (b) Polymer LED (PLED), (c) Hole only device (HOD). 16
1.11 Polymers in a lattice 18
1.12 Polymer chain length 18
1.13 Free energy of mixing for miscible and immiscible systems 21
1.14 Free energy of mixing at metastable conditions 22
1.15 Transferring the Free Energy of mixing into a phase diagram 23
1.16 Schematics of polymer phase diagrams 24

2.1 Energy Diagram MEH-PPV:PVK blend 30
2.2 Ternary Phase Diagrams of MEH-PPV:PVK:chlorobenzene blends 34
2.3 Schematic representation of bifurcation in a ternary MEH-PPV:PVK:CB blend 36
2.4 Ternary phase diagram of the blend system MEH-PPV:PVK:CB 38
2.5 AFM images of MEH-PPV:PVK thin films 38
2.6 TEM images of MEH-PPV:PVK thin films 39
2.7 CLSM images of MEH-PPV:PVK thin films 40

2.8 CLSM images of MEH-PPV:PVK thin films under various excitation intensities 40
2.9 Ternary phase diagram of the blend system MEH-PPV:PVK:CB 42
2.10 Hole and Electron current density vs. applied voltage for MEH-PPV:PVK single carrier devices 43
2.11 Electronic percolation pathways through a MEH-PPV:PVK thin film 44

3.1 Cross-sectional views of device architectures 49
3.2 Ternary Phase Diagrams of MEH-PPV:PS:chlorobenzene blends 50
3.3 AFM and CLSM images of MEH-PPV:PVK and MEH-PPV:PS thin films . 52
3.4 *JV*-characteristics of MEH-PPV:PS thin films 54
3.5 Luminous efficiency of MEH-PPV:PS thin films 55

4.1 Schematic representation of the ToF-SIMS working principle 65
4.2 HO and EO current densities of BEH-PPV:PS1 blend devices 65
4.3 AFM topographical images of BEH-PPV and BEH-PPV:PS blend layers on PEDOT:PSS 67
4.4 ITO work function as a function of time 69
4.5 PEDOT:PSS work function as a function of time 69
4.6 PEDOT:PSS work function after application of organic solvents 70
4.7 PEDOT:PSS work function after application of organic solvents 71
4.8 Typical stack configuration used for ToF-SIMS analysis 72
4.9 TOF-SIMS depth profiles of BEH-PPV and BEH-PPV:PS blend layers on PEDOT:PSS 73
4.10 Calculated composition in blend layer 75
4.11 Thickness corrected depth profiles of BEH-PPV and BEH-PPV:PS blend layers on PEDOT:PSS 77
4.12 Chemical structure of perfluorooctane sulfonic acid. 78
4.13 Desired change in composition of BEH-PPV:PS1 79
4.14 Work function of PEDOT:PSS:FOS 79
4.15 JV current density comparison PEDOT:PSS vs FOS 80

5.1 Chemical structure of BEH-PPV 87
5.2 Simulation versus experiment of hole transport behavior 88
5.3 Simulation versus experiment of electron transport behavior 89
5.4 N_t vs N_{ends} 90

List of tables

3.1 Relative degree of polymerization, monomeric molar volume, and solubility parameter 58
3.2 Flory-Huggins interaction parameters 58

4.1 Layer thicknesses, sputter time and calculated sputter rates for BEH-PPV, BEH-PPV:PS1 blend, PS and PEDOT:PSS films 75
4.2 Calculation of the relative ion sensitivity 76

5.1 BEH-PPV selection with varying polymer length 84
5.2 Estimation of chain end densities for the chosen BEH-PPV polymers 85

Chapter 1

Introduction to Polymer based Semiconductors

1.1 Introduction

The invention of light-emitting organic material began early in the fifties of the last century, where Mette and Pick [51] were among the first researches who synthesized large anthracene crystals and investigated their conductivity whereas Bernanose and Marquet [6] showed electroluminescence from organic compounds e.g. Acridine orange and Quinacrine driven by an alternating current (AC) just one year later. In contrast to that, Pope et al. observed electroluminescence by application of direct current (DC) to thick films of anthracene [64] which laid the foundation to modern OLED design. However, as the films were as thick as 20 µm, voltages around 400 V had to be applied to see light emission. So far, conductivity investigations for organic materials were only done for aromatic compounds, but in 1977 Heeger, Shirakawa and MacDiarmid showed, that conductivity is not limited to these. They chemically doped polyacetylene with bromine and chlorine and showed dramatic rise in the conductivity with the increase of dopant in concentration and type. As their work gained much attention due to its relevancy, it was awarded with the Nobel Prize in the year 2000 [71]. The initial excitement about this new material class dropped quickly as soon as the drawbacks of these materials like their chemical instability and poor processing capability could not be avoided/circumvented.

Nonetheless, progress in research was still made by the Eastman Kodak company on the field of small molecular electronics. Tang and van Slyke presented the first OLED device in 1987 introducing the concept of an evaporated dual layer stack to enhance efficiency [78]. The field of polymeric electronics had one of its breakthroughs in 1990 when Burroughes et al.

fabricated the first polymer light-emitting diode at Cambridge University based on a polymer with alternating phenylene and vinylene moieties (PPV)[10]. The device structure comprises of a solution processed polymeric layer sandwiched between a transparent Indium doped tin oxide anode and a reflecting aluminum cathode. Unlike inorganic materials for electronic applications, that are typically made from Silicon, Germanium or Gallium, organic materials have the advantage of low temperature processing and easier accessible chemical variety. Organic compounds consist mainly of carbon, hydrogen, oxygen and nitrogen. Whereas other elements are introduced to change the original properties slightly, the polymeric backbone is not modified. Organic semiconductors get their unique properties due to their conjugation. Carbon can form three types of bonds, namely sp^3, sp^2 and sp hybrid orbitals forming single, double and triple bonds, respectively. Each is characterized by different hybridization levels. Unbound carbon consists of a fully filled 1s and 2s orbital while two of the three 2p orbitals are only filled with one electron (see fig. 1.1 a)). This changes when carbon interacts with bonding partners. To form single bonds all three 2p orbitals hybridize with the 2s orbital to consequently create four degenerate sp^3-hybrid orbitals (see fig. 1.1 b)) which in turn form four σ bonds with bonding partners (a prominent example is methane, CH_4). In contrast, double bonding is possible through creation of three sp^2 hybrid orbitals and one remaining p orbital (see fig. 1.1 c)). In this case, two single bonds are established via σ bonding through overlap of sp^2-hybrid orbitals with s-orbitals, whereas the remaining double bond is formed through a σ and a π-bond. Triple bonds are described analogously. Two sp-hybrid orbitals are created through hybridization of two s-orbitals with two p-orbitals so that two p-orbitals are left (see fig. 1.1 d)). One single bond is created through a σ-bond with one bonding partner. The other bond is established through a σ and two π-bonds forming the triple bond.

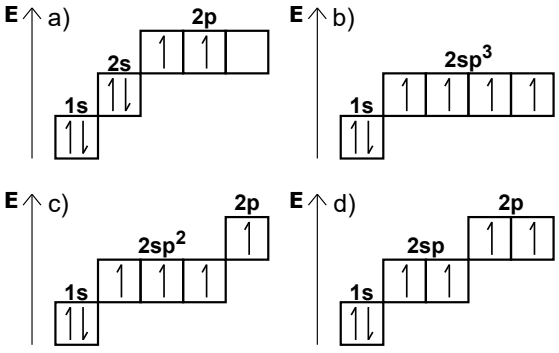

Fig. 1.1 The theory of hybridization of a) carbon atomic orbitals when describing b) sp^3, c) sp^2 and d) sp-hybrid orbitals.

To describe covalent bond types the theory of linear combination of atomic orbitals (LCAO) is used. Molecular orbitals are considered as a linear combination of individual

orbitals which can be visualized for valence electrons of ethylene in fig. 1.2. The central bond of ethylene is a sp^2-hybridized double bond. The linear combination of two sp^2-hybrid orbitals forms a bonding σ and an antibonding σ^*-molecular orbital, the first being lower in energy and the latter much higher. The same happens to the p-orbitals of both carbon atoms. They form an energetically lower lying bonding π and an energetically higher lying antibonding π^*-molecular orbital. The π-molecular orbital is the so called highest occupied molecular orbital (HOMO), whereas the π^*-molecular orbital is the so called lowest unoccupied molecular orbital (LUMO). As long as the bonding molecular orbitals are lower in energy than their initial equivalents a stable bond is formed.

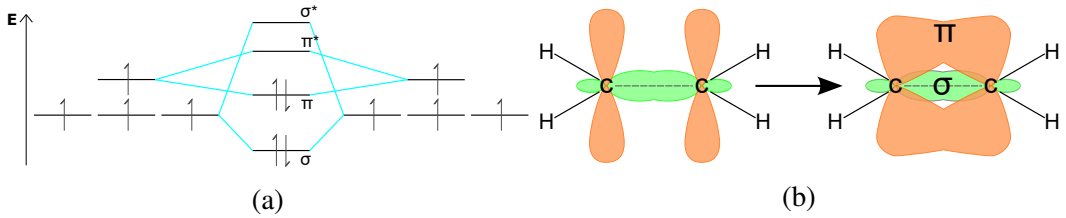

(a) (b)

Fig. 1.2 Linear combination of atomic orbitals for ethylene.

The extension of this concept forming alternating double bonds and single bonds (eg. 1,3-pentadiene, 1,3,5-heptatriene and so on) is called conjugation. Conjugation stabilizes the whole molecule as electrons are not bound to one individual atom but rather delocalized over the whole molecule (see fig. 1.2 b)). On larger molecules or even macromolecules such as polymers like polyacetylene conjugation leads to a smaller energetic gap between the HOMO and the LUMO and a simultaneous increase in density of energetic states for both the HOMO and the LUMO [9]. Theoretically, for an infinite long polymer with perfectly alternating bonds, overlapping valence and conduction bands would lead to continuous energetic states and metal like transport would be possible. Real polymers never exhibit ideal behavior. The Peierls distortion of polymers [8] circumvents an overlap of the HOMO and LUMO levels, but more importantly, real polymers suffer from chemical impurities, kinks and torsions, introducing even more deviations from the ideal behavior. Effectively, the description of the electronic structure of a polymer has to be limited to segments of the polymer chain with an effective conjugation length. Furthermore, the interaction between polymer chains is rather weak and often limited to van-der-Waals forces. Intermolecular interaction across different polymer chains is somewhat weak and energetic distribution is narrow. Thus, charge transport is expected to be much slower than for inorganic electronics made from conventional materials such as silicon. The distribution of energetic states in organic/polymeric materials is often described with a Gaussian function as formulated in eqn. 1.1:

$$DOS(E) = \frac{N}{2\sqrt{\pi}\sigma} exp(\frac{-(E - E_{\mathrm{HOMO}})^2}{2\sigma^2}) \tag{1.1}$$

with N as the density of transport sites and σ as the width of the Gaussian *DOS*. Moreover, energetic states within the *DOS* are rather localized and charge transport happens via thermally assisted tunneling between the states (see fig. 1.3 (a) and (b)).

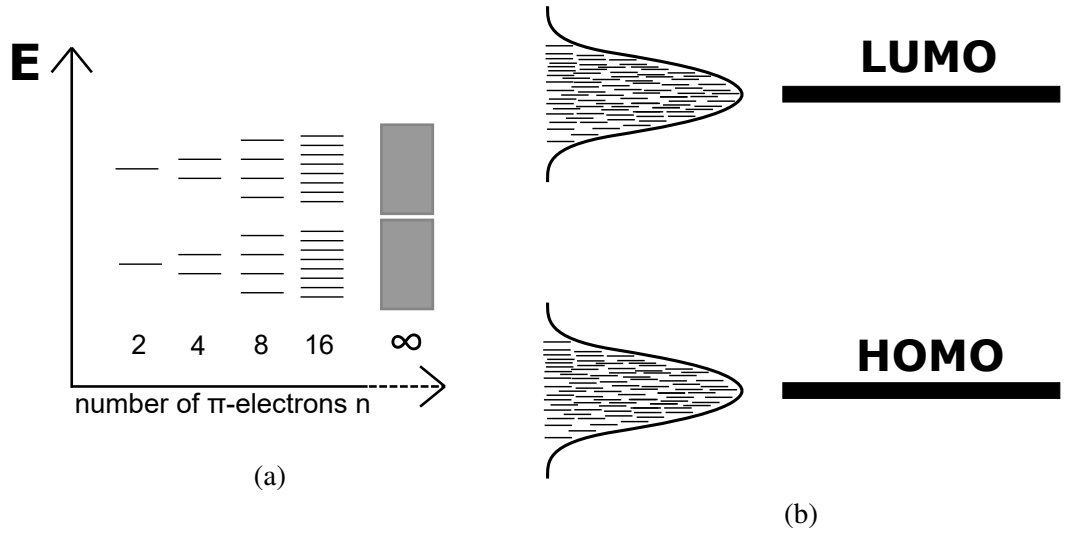

(a) (b)

Fig. 1.3 Extended conjugation for longer molecules

The major difference of organic and inorganic semiconductors is the energetic order in the system. The latter usually exhibiting 3D coupling between the covalently bound atoms resulting in broad conduction and valence bands. In contrast, even highly ordered organic semiconductors show a narrow width of energetic distribution for the HOMO and the LUMO levels. The energetic gap that is present between the HOMO and the LUMO is also called band gap and ranges typically between 1 eV and 4 eV for conjugated polymers.

Highly disordered systems such as polymers are dielectrics and usually used for insulation of metallic conductors. Conjugated polymers like polyacetylene or polyphenylenevinylenes exhibit somewhat different behavior. When charges are injected into disordered conjugated systems, a space charge region is formed. Due to very low concentration of charge carriers, charges cannot be neutralized with counter charges as in metals. As a result, a limited conduction is possible. The injected charges create an electric field that further limits the charge injection. This so called space charge limited current (SCLC) is present in all dielectric materials and well described by the Mott-Gurney-Law [56] and specified in eqn. 1.2:

$$J = \frac{9}{8}\varepsilon_0\varepsilon_r\mu\frac{V^2}{L^3} \tag{1.2}$$

with ε_0 as the permittivity of the vacuum, ε_r as the dielectric constant of the material, μ as the mobility of charge carriers, V as the voltage and L as the film thickness. Special attention should be given to the mobility parameter. The product $v = F \cdot \mu$ with F being the applied electric field gives the drift velocity v of charge carriers and tells how fast charge carriers are transported through a material. Accordingly, conductivity is defined as $\sigma = n \cdot e \cdot \mu$ with n as carrier density and e as the elementary charge. To further understand how charges are transported through a polymer semiconductor one has to consider energetic disorder. HOMO and LUMO levels in polymers consist of localized energetic states. The spread in energy is caused by differently sized polymeric segments with each segment contributing differently to the energetic gap (see figure 1.4 (a)). The energetic distribution of these states is in the order of 0.1 eV to 0.2 eV. In order to transport charges through the localized energetic states of the polymeric material, a small energetic barrier has to be surpassed with the help of phonons (thermal energy causing lattice vibrations). Consequently, increased thermal energy in the polymeric system increases the conductivity.

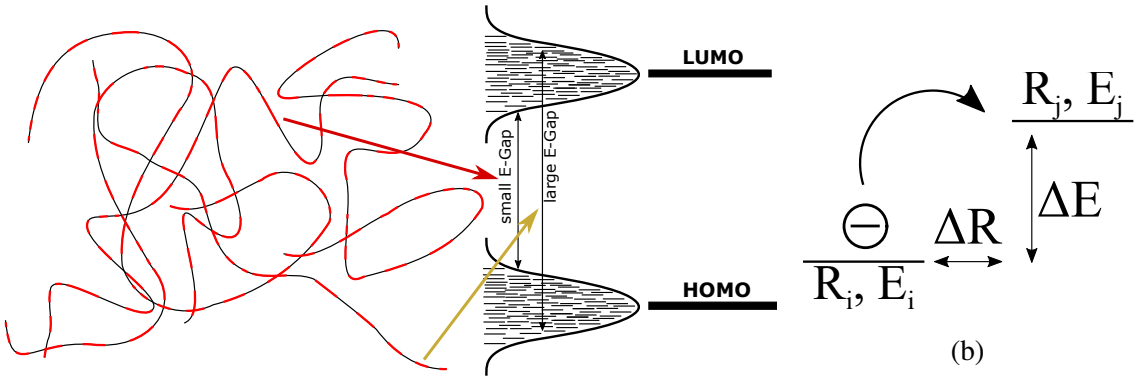

Fig. 1.4 Conjugation change in Polymers and Thermal hop

Such thermally assisted conduction was proposed for impurities in inorganic materials in 1956 by Conwell and Mott [14, 55] after which Miller and Abrahams [53] formulated an expression for the hopping rate W_{ij} between two energetic states, E_i and E_j, eqn. 1.3:

$$W_{ij} = \nu_0 \cdot exp(-2\alpha|\vec{R_{ij}}|) \begin{cases} exp(\frac{-E_j - E_i}{kT}), & E_j > E_i \\ 1, & E_j < E_i \end{cases} \tag{1.3}$$

with R_{ij} as the distance between the energetic states, ν_0 the attempt-to-escape frequency, α the localization length and k the Boltzmann constant. The first term represents the exponential tunneling probability when the wave functions of the states i and j overlap, whereas the second term accounts for the energetic barrier or better the phononic distribution as a function of temperature, a classical Boltzmann behavior. First successful attempts to use this model for disordered systems were done by Bässler in 1993 [5]. He used the Miller-Abrahams formalism and applied it to a Gaussian distributed density of states description as it is shown in equation 1.4. He proposed a Monte Carlo simulation approach to calculate the actual mobility and found an analytical description in the form of eqn. 1.4:

$$\mu = \mu_\infty exp\left[-(\frac{2\sigma}{3kT})^2\right] \begin{cases} exp\left[C\left((\frac{\sigma}{kT})^2\right) - \Sigma^2\right) F^{1/2}\right], & \Sigma \geq 1.5 \\ exp\left[C\left((\frac{\sigma}{kT})^2\right) - 2.25\right) F^{1/2}\right], & \Sigma < 1.5 \end{cases} \tag{1.4}$$

with μ_∞ being the mobility at infinite temperature, C a constant value describing the lattice spacing and Σ as a positional disorder parameter. This approach was named Gaussian Disorder Model (GDM). It shows that mobility depends inversely to the square root of the temperature and is non-Arrhenius type. Although good agreements were found for high electric fields (typically > 10^8V/m) showing that mobility has a significant field dependency, discrepancies for low fields could not be addressed. To improve the modelled mobility description also at low electric fields, Gartstein and Conwell used a different description taking spatially correlated energetic states into account [20]. Their model is called correlated disorder model (CDM). Carrier density in disordered polymeric semiconductors is usually low which in the past lead to the assumption that mobility is density independent. However, in 2003 experimental evidence was found that indeed mobility increases with charge carrier density [76]. Yet, a study of the influence of electric field and charge carrier density on mobility at the same time is not straightforward possible for a diode structure. Hence, Tanase et al. [76] combined mobility measurements for field effect transistors (FET) and diodes. In FETs, charge carrier density increases in the channel with rising voltage at the gate contact, whereas the electric field between source and drain contact remains almost constant. This special setup made it possible to dissect the influence of charge carrier density without changing the electric field. They showed that despite using the same material

as semiconductor, the charge carrier mobility is orders of magnitude higher in FET than in diodes. They concluded that FET charge carrier density increased significantly due to increasing gate bias, whereas hopping transport in diodes happens solely through tail states of the Gaussian distributed DOS, which eventually limits the amount of neighboring states with a relatively flat energy barrier. In contrast, FET energetic states are filled to a much higher energy level, in which the Fermi-level is located at an energetic state with much higher density of neighboring states than in diodes. As a result, hopping transfer increases due to a higher density of neighboring states with relatively flat energy barriers. Later, Pasveer et al. [62] applied the above mentioned assumptions in model calculations and proposed a model showing strong density dependency of the mobility at high temperatures (for instance 295K). However, at lower temperatures mobility is more dependent on electrical field than on density. Their model uses a numerical solution of the Pauli master equation (eqn. 1.5), which reads:

$$\sum_{i \neq j} = \left[W_{ij} n_i (1 - n_j) - W_{ji} n_j (1 - n_i) \right] = 0 \tag{1.5}$$

n_i is the probability that site i is occupied and $1 - n_j$ is the probability that state j is unoccupied. The sum equals to zero only if the system finds itself in equilibrium state. To correct for the applied electric field the term $-eFR_{ijx}$ is added to the Miller-Abrahams equation (see equation 1.3). Furthermore, hopping to an occupied energetic state is avoided by taking strong repulsive forces into account so that Fermi-Dirac statistics remain valid. Numerical solution of the Pauli master equation in a three dimensional lattice the mobility is obtained as follows:

$$\mu = \sum_{ij} W_{ij} n_i (1 - n_j) R_{ijx} / nFV, \quad n = \frac{< n_i >}{a^3} \tag{1.6}$$

with a as lattice constant and V as the volume. Further parametrization separates the density relation from the field dependency as shown in eqn. 1.7:

$$\mu(T, n, F) = \mu(T, N) f(T, F) \tag{1.7}$$

Individual charge carrier mobility is given by:

$$\mu(T,n) \approx \mu_0(T,n) exp(-C\hat{\sigma}^2) exp\left[\frac{1}{2}(\hat{\sigma}^2 - \hat{\sigma})(2na^3)^{\delta}\right]$$
$$\hat{\sigma} = \frac{\sigma}{kT}, \quad \delta = 2\frac{ln(\hat{\sigma}^2 - \hat{\sigma}) - ln(ln(4))}{\hat{\sigma}^2} \tag{1.8}$$

with $a = \frac{1}{\sqrt[3]{N}}$ as the intersite distance and $C = 0.42$. The parametrized field dependency reads as:

$$f(T,F) = exp\left\{0.44(\hat{\sigma}^{\frac{3}{2}} - 2.2)\left(\sqrt{1 + 0.8\left(\frac{eaF}{\sigma}\right)^2} - 1\right)\right\} \tag{1.9}$$

μ_0 is the zero field, zero density and infinite temperature mobility. In the limit of zero carrier density this model equals to the expressions developed by Bässler. To sum up, the described model considers temperature, density and field dependency and is therefore called the extended Gaussian disorder model (EGDM).

1.2 Trap-limited charge transport

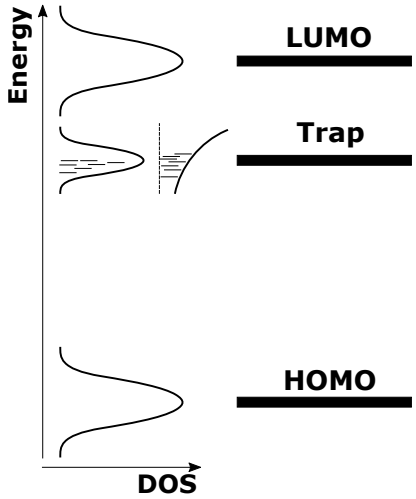

(a)

Fig. 1.5 Distribution of energetic states in an organic semicondutor. The DOS description for trap states is shown in a gaussian and an exponential shape, respectively.

It has been shown previously that charge transport through a highly disordered conjugated polymer system follows a space-charge-limited current description (see 1.1). Trapping of charge carriers in energetic states within the bandgap of the polymer has been observed for many polymers. In the mid 90-s of the last century Blom et al. [7] observed that conduction for individual charge carriers, namely holes and electrons, differs by several orders of magnitude. The hole transport is considered to be sufficiently described by SCLC characteristics (eqn. 2.1) and bulk limited instead of injection limited. In contrast, electron transport suffers severe trapping behavior. Electrons that are conducted through the LUMO level of the polymer eventually fall into a localized energetic state below the LUMO level, a so called energetic trap. Transport through these states is highly unlikely as the density of these trapping energetic states is rather low (in the range of 10^{18}cm^{-3}). Despite the small number of trapping states, their effect on electron transport is extremely severe. Trapping of electrons can be analyzed from the current density vs. voltage dependency, as shown in figure 1.6.

The current density of such devices shows strong voltage and thickness dependency. A high slope in current voltage (JV curve) characteristics, differs strongly from the regular SCLC behavior with a slope of 2 in a log-log plot which is related to the distribution of trapping states (see 1.6). Additionally, a hysteresis behavior is observed for the JV characteristics of electrons. The downward sweep of the voltage results in a lower current density than the preceding upward sweep. A possible explanation for the latter effect is charge trapping in deep trap states. Electrons that fall into deep trap states reside in the device and disturb the internal electrical field, which in effect results in a lower current density for the downward scan compared to the upward scan [16].

In 2012 Nicolai et al. [58] investigated different conjugated polymers with special focus on the slope of electron JV characteristics as a function of the LUMO level for the polymers. They found that the double logarithmic slope for electron current voltage characteristics decreases with decreasing LUMO level, ultimately resulting in a slope of 2 for LUMO levels around -3.8 eV or lower. The characteristic slope of 2 is a strong indication for trap free SCLC. Moreover, all polymers showed comparable trap densities of $N_t \approx 3-5\cdot 10^{23}$ m^{-3} and the energy level for the trap states was found to be at a depth of -3.6 eV throughout the whole study. They concluded that the origin of such trap states may be of extrinsic nature which speak for impurities that were introduced during the synthesis procedure. To date, no clear explanations are found for these traps, but $(H_2O)_2-O_2$ complexes were identified as possible candidates in comparison to less like structural defects (kinks) in the polymer. First attempts to describe trap-limited currents were done in 1956 by Lampert for inorganic systems [42]. He assumed a system with a discrete trap level which showed SCLC behavior

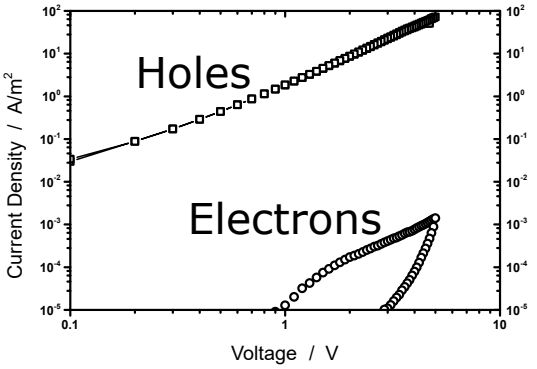

(a)

Fig. 1.6 Typical current density versus applied voltage characteristics of an organic semiconducting polymer. The current density for holes is several orders of magnitude higher than the current density for electrons.

but reduced by a factor ϑ, that scales exponentially with the trap depth E_{tc} (with respect to the valence- or conduction band, for hole or electron conduction, respectively) and reads as follows:

$$\begin{aligned} J &= \frac{9}{8}\varepsilon_0\varepsilon_r\mu\vartheta\frac{V^2}{L^3} \\ \vartheta &= \frac{N}{N_t}exp\left(\frac{-E_{tc}}{kT}\right) \end{aligned} \tag{1.10}$$

N is the density of transport and N_t the density of trap sites. The current in this system is lowered due to traps until it reaches a state where all trap states are filled. In this trap-filled limit, drastic increase of current is observed and finally ends in SCLC. Similar behavior cannot be studied for organic or polymeric semiconductors. As already mentioned, trap states in polymers are not discrete in nature but rather a distribution of localized states. To account for a distribution, Mark and Helfrich used a description of exponentially distributed trap states in organic solids [47]:

$$D_{exp,t} = \frac{N_t}{kT_t}exp\left(\frac{|E-(E_c-E_{tc})|}{kT_t}\right) \tag{1.11}$$

with T_t being the characteristic trap temperature defining the exponential shape of the distribution. In combination with the Poisson equation a description for trap-limited current

was found:

$$J_{TLC} = N_c q \mu_n \left(\frac{\varepsilon_0 \varepsilon_r}{q N_t exp\left(\frac{E_{tc}}{kT_t}\right)} \right)^r \left[\left(\frac{2r+1}{r+1} \right)^{r+1} \left(\frac{r}{r+1} \right)^r \right] \frac{V^{r+1}}{L^{2r+1}} \tag{1.12}$$
$$r = \frac{T_t}{T}$$

q equals to the elementary charge and μ_n is the free electron mobility. The slope of a double logarithmic plot of JTLC versus applied voltage relates directly to the value of r. As previously mentioned, charge transport through HOMO and LUMO levels is mainly described by hopping transport through a Gaussian DOS. Therefore, a description of Gaussian distributed trap states instead of an exponential distribution is reasonable. In fact, studies were carried out to introduce Gaussian trap state description [30] and later how these compare to discrete and exponential trap distribution [59]. Researchers found that a discrete trap level gives approximately the same effect as a Gaussian distribution of trap states under the assumption of very low trap density. At rather high values (and typical voltages) it deviates strongly. In contrast, the exponential distribution of trap states has low deviation with the Gaussian description at rather high trap density. The exponent r in equation 1.12 for a Gaussian distribution of trap states can be expressed in the following form, including the width of the Gaussian trap distribution σ_t:

$$r = \sqrt{1 + 2\pi \left(\frac{\sigma_t}{4kT} \right)^2} \tag{1.13}$$

It is important to be mentioned that several assumptions had to be made to obtain the preceding relations. Firstly, it was assumed that diffusion current had negligible effects. Secondly, the mobility was kept constant and third, it was stated, that the density of trapped charges is significantly higher than free charge carrier density ($n_t \gg n$). It is of high importance to discuss the effect of charge carrier trapping, as trapping in polymer based light-emitting diodes (PLED) is a major reason for efficiency loss. Charge carriers that are trapped lead to a nonradiative recombination process, a so called Shockley-Read-Hall-recombination (SRH recombination), also known as trap-assisted recombination, first described in 1952 [72, 24]. In PLEDs it is a competing process to the bimolecular radiative recombination, which is of Langevin-type [43].

1.3 Polymer materials for semiconductor application

This work discusses the use of polymers of organic nature where chemical synthesis is straightforwardly possible. Diversification and tuning of individual properties compared to inorganic semiconductors is achievable with comparably less effort. Routes to synthesize conjugated molecules and especially polymers are as manifold as the number of molecules that can be created. Conjugation, as discussed in previous chapters, is the responsible property of organic materials for feasible charge transport. Conjugation is usually established along the backbone of the polymer and sidechains are generally attached in order to tune specific properties such as solubility and processability. In contrast, the optoelectronic properties are tuned by changing the species of the backbone. A prominent class of orange-red emitting polymers are poly(p-phenylenevinylene) (PPV) based polymers. Their common chemical structure can be found in figure 1.7. Non derivatized PPV, on its own, is poorly synthesizable and insoluble. The polymerization procedure stops at early stages and short conjugation lengths due to strong pi-pi stacking and results in an oligomer with greenish light emission. In order to circumvent the pi-pi stacking behavior, conjugated polymers are synthesized with sidechain functionalized monomeric units, resulting in a vast variety of different polymers with much increased solubility. The most well known PPV derivatives are poly[2-methoxy-5-(2-ethylhexyloxy)-p-phenylenevinylene] (MEH-PPV), poly[2-(ethylhexyloxy)-p-phenylenevinylene] (BEH-PPV) and poly(2-[3'-(3,7-dimethyloctyloxy)]5-methoxy-p-phenylenevinylene)-co-(2-[3'-(3,7-dimethyloctyloxy)]-phenyl-p-phenylenevinylene) (SY-PPV) [73]. The most important route to synthesize PPV based polymers is the so called Gilch route, which is a radical dehydrohalogenation polymerization [21] and has been recently studied kinetically by Schönbein et al. [68]. All of these polymers are under strong investigation since more than two decades and serve as almost ideal systems to study charge transport as well as photo-physics of conjugated polymers.

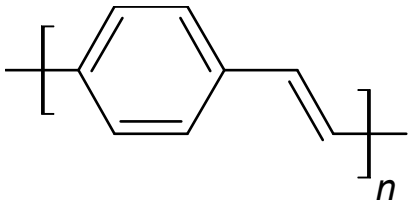

Fig. 1.7 Chemical structure of poly(phenylenevinylene) based polymers

Next to PPV based polymers, other conjugated polymers exist. Blue and green polymer emitters are typically represented by the group of poly-p-phenylenes (PPP) with the subgroup of polyfluorenes. Especially, poly(9,9-dioctylfluorene) (PFO) has been studied extensively

due to its possibility to change morphology from amorphous to semi-crystalline state [63] . The blue emission of PFO originates from its deep HOMO level of 5.7 eV [11] and shallow LUMO (2.9 eV). It creates an injection barrier with most hole injection electrodes like PEDOT:PSS (5.1 eV). Shifting of the LUMO level can be done by introducing benzothiadiazole (BT) moieties into the backbone of PFO, which results in another prominent copolymer called F8BT (see figure 1.8 (b)) with green emission. The synthesis procedure for these polymers is usually done by Suzuki coupling [54].

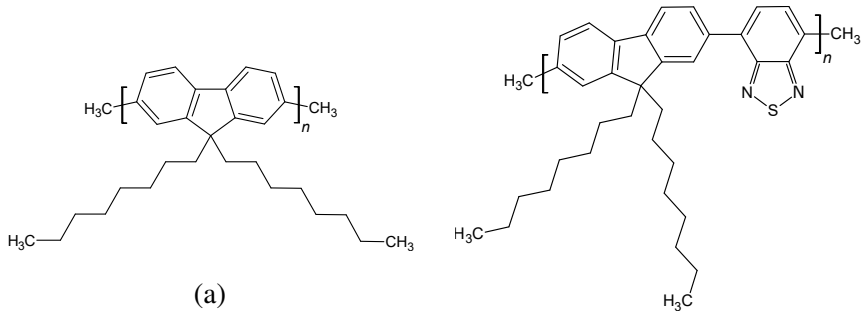

Fig. 1.8 Chemical structure of poly(9,9-dioctylfluorene) (PFO) (a) and poly(9,9-dioctylfluorene-alt-benzothiadiazole) (F8BT) (b) as prominent blue and green emitters in PLED application

Charge carrier transport is not limited to polymers with conjugated backbone. Poly(9-vinylcarbazole) (PVK) (figure 1.9) as an example, has a non-conjugated backbone and a conjugated carbazole sidechain through which charges are transported. This polymer was studied as photoreceptor in xerographic applications and will be of importance in chapter 3.

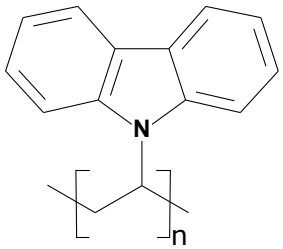

Fig. 1.9 Chemical structure of poly(9-vinylcarbazole) PVK

1.4 Device Structures

A convenient way to study performance properties of organic semiconductors is to fabricate electrical devices, where semiconducting, transporting and buffer layers are sandwiched

between an anode and a cathode. Due to low mobility of typical materials and for the sake of low operating voltages, device thickness should be limited to approximately 100 - 200 nm. Next to other device architectures, a polymer light-emitting diode (PLED) can be fabricated. This device type is a so called dual carrier device. Electrons are injected by the cathode and holes by the anode. Both charge carriers are transported through the material. Eventually, hole and electron can form an exciton, which is a bound electron-hole pair stabilized by Coulomb attraction forces. The exciton can decay radiatively by recombination of the hole and the electron. This is the desired process in a PLED, but unfortunately it is competing with several loss processes that limit the device efficiency.

For small-molecule based organic light-emitting diodes (OLED), it is common to use vacuum deposited multilayer structures in order to tackle at least some of the loss processes. For instance, distinct hole and electron transport layers are introduced. All of these layers have the purpose to disentangle charge transport from light emission. A good example is the thickness of the emissive layer. It is kept as thin as possible (on the order of 5 to 10 nm) to confine the recombination zone where light is generated. Charge transport in this layer becomes a minor (or even negligible) factor for overall device performance. On the other hand, transport layers with varying thicknesses are used to tune electron and hole transport in order to have balanced charge transport to the emissive layer and good out-coupling efficiency. OLED devices are fabricated by vacuum deposition techniques, which is on the one hand a complicated and material intensive process, but on the other hand very scalable and therefore industry relevant. PLED devices, as an alternative, also have the potential for mass production as solvent casting methods are potentially cheap methods for polymeric materials, but purity and especially ways for multilayer fabrication are limited. Subsequently cast polymeric layers damage underlying layers due to the similar solvent. Several successful attempts to circumvent this problem were demonstrated in the literature, some using orthogonal solvents [22, 50] and others like Kasparek et al. using a UV-curable host-guest system [35, 34, 36].

In order to study more fundamental properties than simply overall efficiency other device structures can be fabricated. Charge transport properties of individual charge carriers are important. In previous chapters, we have seen that one major loss process is caused by energetic trap states affecting electrons during their transport process in polymeric semiconductors. Holes, in contrast, are transported trap-free. To individually investigate single charge carrier transport, it is possible to fabricate so called hole-only (HO) or electron-only (EO) devices. Together with the classic PLED structure, those three complementary device structures can give useful insight into bulk properties and open the possibilities to investigate charge transport for individual charge carriers. Both for HO and EO devices, it is important to establish ohmic contacts to the polymer semiconductor. For the case of a HO device,

holes are transported solely through HOMO levels of the polymer. To build such a device, efficient injection and extraction of holes has to occur. High work function materials with small or no injection barriers (ohmic injection) to the HOMO level of the polymer need to be applied as contact. Well known injection contacts for PPV based semiconductors are indium doped tin-oxide (ITO), poly(3,4-ethylenedioxythiophene):poly(styrenesulfonic acid) (PEDOT:PSS) (Clevios™ P VP AI 4083) and MoO_3, with work functions $W_{ITO} \approx 4.1 - 5.2$ eV, $W_{PEDOT:PSS} \approx 5.1$ eV and $W_{MoO_3} \approx 6.7$ eV, respectively. The work function of ITO varies significantly large depending on the oxygen vacancy density at the surface, therefore it is common practice to activate it in an oxygen plasma and to coat it immediately with a buffer layer of PEDOT:PSS. The semiconducting polymer is sandwiched between these contacts to form an ITO/PEDOT:PSS/Polymer/MoO_3/Al stack (see figure 1.10 (c) for comparison). Injection of electrons into the LUMO of the polymer is almost impossible due to large injection barriers.

On the other side, to fabricate an EO device low work function electrodes have to be used to exclusively inject electrons into the LUMO states of the polymer. The range of employable low work function materials is comparably low as they are typically earth-alkali metals or alkali salts (Ba, Ca, LiF, $CsCO_3$), with high reactivity towards oxygen and water. In this work, Barium with a work function of $W_{Ba} \approx 2.7$ eV and Aluminum ($W_{Al} \approx 4.3$ eV) are mainly used. Similar as in HO devices, the conjugated polymer is sandwiched between the metal electrodes, with Aluminum as bottom and Barium as top contact. The Barium top contact additionally is covered with an Aluminum layer, to protect the underlying Barium from fast oxidation. The final stack configuration is Al/Polymer/Ba/Al from bottom to top (see figure 1.10 (a) for comparison). Barium as cathode material easily injects electrons into the LUMO states of the polymer; an ohmic top contact for electrons is established. The anode (bottom electrode) in contrast cannot inject holes nor electrons efficiently.

A PLED is a dual carrier device, which means both electrons and holes are injected simultaneously. A typical device stack consists of ITO/PEDOT:PSS/Polymer/Ba/Al (see figure 1.10 (b) for comparison). As in HO devices, PEDOT:PSS is used as ohmic contact to inject holes into the device. The top contact (cathode) is made from Ba and efficiently injects electrons into the polymer layer.

All three device types together behave complementary to each other. With both single carrier devices one can study individual charge transport properties and in particular trapping behavior. PLEDs give additional information on recombination processes, i.e. radiative and non-radiative recombination, as well as on excitonic quenching and intrinsic life time.

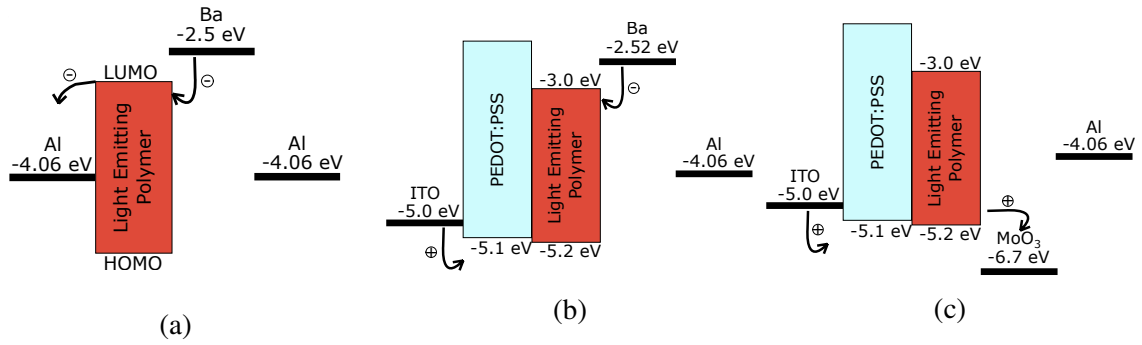

Fig. 1.10 Device stack configurations. (a) Electron only device (EOD), (b) Polymer LED (PLED), (c) Hole only device (HOD).

1.5 Thermodynamics of polymer mixtures

Thermodynamics of polymer mixtures in PLEDs will play a crucial role in the coming chapters of this work. Historically seen, polymer mixtures, also called polymer blends, were mainly used in organic photovoltaic devices (OPV), where the separation of charge carriers at interfaces of two materials plays an important role to increase device efficiency. A brief discussion of the field of OPV devices will be done to outline the importance of using polymer blends in organic electronics.

Morphology of polymer blends is a crucial ingredient to tune efficiency in OPV devices and extensive studies have been carried out to investigate the interplay of different parameters of morphology on device efficiency (for example [38]). Absorbed photons in OPV devices lead to the generation of bound electron hole pairs, so called excitons. Excitons have no net charge and therefore cannot be extracted from the device to generate electrical energy. To split such an exciton into its individual free charge carriers, it is necessary to offer energetically more favorable states for the charge carriers which simultaneously are spatially separated. Therefore, great effort was invested to use polymer blends in OPV devices. Polymer blends usually undergo phase separation as in most cases intimate mixing of the blend components is energetically unfavorable (a prominent example is the mixture of water and oil). An interface between the two polymers is created. One of the materials transports holes (donor material) and the other electrons (acceptor material), depending on their HOMO (for holes) or LUMO levels (for electrons). For such devices, it is crucial to have as much interface as possible between the blend components to efficiently separate the generated excitons into holes and electrons. With the application of a small electric field electrons are driven towards the cathode and holes towards the anode; the OPV device can be used as an electrical power source. Absorption of light, charge transport as well as recombination of free and bound charge carriers can be influenced by the morphology and the individual phase composition of

the blend. The process of mixing and demixing of the blend components plays a key role to tune efficiency of OPV devices. Not less important is the use of polymer blends in PLEDs as the material properties that are used to separate charge carriers in OPV devices can also be utilized to enhance controlled radiative recombination in PLEDs. Surely, the material properties have to be somewhat different and structure and morphology of the blend has to be tuned in order to increase charge carrier mobility and PLED efficiency. Practical application and further details will be part of following chapters.

The shape and nature of phase behavior in blends gives numerous variations which influence emission color, efficiency and structure size. Prediction of polymer blend morphologies is still a difficult task. The understanding of processes in the dynamics of blend morphology formation is based on mostly phenomenological observations, especially in the field of polymer electronics. Optimization of morphology has become a skill rather than by application of rational understanding. To improve understanding of polymer mixtures, the thermodynamics of mixing needs to be considered.

Two independent studies done by Flory and Huggins in 1942 [19, 29] used a lattice theory for long-chain polymers to develop an expression calculating the free energy of mixing for polymers. Their approach was to separate a polymer into chain units that can occupy consecutively connected lattice sites (see figure 1.11 (a)). Initially, their description of the free energy of mixing was defined for mixing of long chain polymers but is also applicable for polymers mixed with solvents as it is done in this work. First assumptions have to be made. One chain unit occupies the same volume as a solvent molecule (or another monomeric unit in a binary polymer blend) and the volume is incompressible:

$$\nu_{monomers} = \nu_{solvent} \tag{1.14}$$

The orientation of bonds between chain units is totally random, but the next unit cannot overlap with one of the previous ones (see figure 1.11 (b)). This is similar to a description of a non-reversing random walk.

The quantification of such as system is given by the Helmholtz free energy of mixing and can be described as follows:

$$\Delta F_{mix} = \Delta U_{mix} - T\Delta S_{mix} \tag{1.15}$$

The change of free energy ΔF_{mix} consists of an energetic ΔU_{mix} and an entropic part $T\Delta S_{mix}$. In order to calculate the statistical thermodynamics for such a system, every spatial

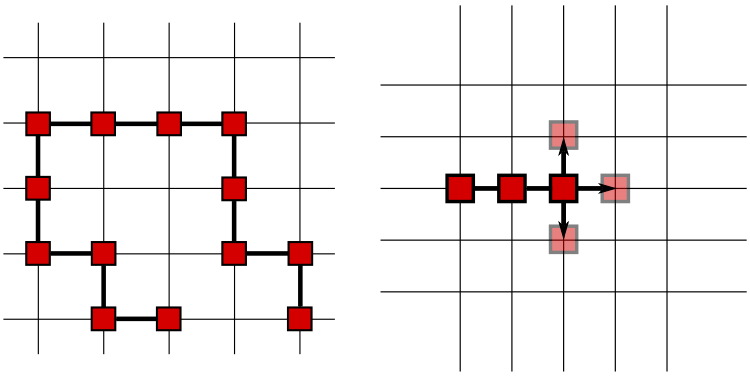

Fig. 1.11 (a) Schematic description of a polymer chain on a 2D lattice occupying lattice sites, (b) the chain end can occupy neighboring lattice sites but cannot overlap an occupied site.

arrangement with various energetic levels for each molecule has to be considered. To date, such calculations are almost impossible. To facilitate such calculations, a mean-field approach is chosen. It assumes that every molecule experiences an average force field. Spatial arrangement of molecules becomes independent of the number of molecules in the same energetic level. This opens the possibility to calculate the entropy and energy individually. According to Boltzmann's relationship $S = k_B ln\Omega$, summation of all possible spatial arrangements determine the entropy of the system. The energy of the system is determined by summation of all energetic contributions given by mutual interactions between all sites.

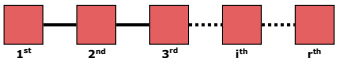

Fig. 1.12 Schematic description of the chain length.

In order to calculate the entropy, a lattice with N sites is created and j chains are put into that lattice. Assuming that all polymer chains are of equal length (also called monodisperse), every chain has r equally sized segments. The first segment of the next chain $(j+1)$ has to be placed into one of the $N - r \cdot j$ vacant sites. Now there are limited ways to put the second segment of the $(j+1)$th chain. The first monomer has z coordination sites whereas the second and every following monomer only $z-1$ coordination sites (under the assumption of a non-branched chain). The fraction of vacant sites reduces with every additional monomer that is put into the lattice. In effect, the probability to find a vacant site for the r-th monomer is $1 - ((r \cdot j + r - 1))/N$; multiplied with the amount of coordination sites it results in $(z-1)[1 - ((r \cdot j + r - 1))/N]$ possibilities to place the r-th monomer on the lattice. To sum up, there are W_{j+1} possibilities to put the $(j+1)$th chain on the lattice:

$$W_{j+1} = z(z-1)^{r-2}(N-rj)\prod_{i=1}^{r-1}\left(1-\frac{r\cdot j+i}{N}\right) = \frac{z(z-1)^{r-2}}{N^{r-1}}\cdot\frac{(N-r\cdot j)!}{(N-r\cdot j-r)!} \tag{1.16}$$

Now if we consider N_2 chains that have to be placed homogeneously on a lattice with N sites, then the total ways of arrangement of the solution system Ω are equivalent with the number of possible ways to arrange N_2 chains. For solvent molecules there is only one way to arrange them on the single lattice sites as they are identical. The resulting expression reads as:

$$\begin{gathered}\Omega = \frac{1}{2^{N_2}N_2!}\prod_{j=0}^{N_2-1} W_{j+1} \\ \Omega = \frac{z^{N_2}(z-1)^{N_2(r-2)}}{2^{N_2}N^{N_2(r-1)}N_2!}\cdot\prod_{j=0}^{N_2-1}\frac{(N-rj)!}{[N-r(j+1)]!} = \frac{z^{N_2}(z-1)^{N_2(r-2)}}{2^{N_2}N^{N_2(r-1)}N_2!}\cdot\frac{N!}{(N-rN_2)}\end{gathered} \tag{1.17}$$

With Boltzmann's description for entropy $S_{mix} = k\cdot ln\Omega$ and application of Stirling's approximation $lnA! \approx AlnA - A$ for $A \gg 1$ we obtain:

$$\frac{S_{mix}}{k} = ln\Omega = -N_1 ln(\frac{N_1}{N}) - N_2 ln(\frac{N_2}{N}) - N_2(r-1) + N_2 ln(\frac{z}{2}) + N_2(r-2)ln(z-1) \tag{1.18}$$

where N_1 corresponds to the number of solvent molecules. In order to calculate the change in entropy upon mixing ΔS_{mix}, the entropy of the pure compound needs to be subtracted from the entropy in the mixed state S_{mix}. With $N_1 = 0$ (no solvent molecules present) and when all lattice sites are occupied by polymer segments $N = rN_2$, the entropy of the purely disordered polymer is obtained:

$$\left.\frac{S_{mix}}{k}\right|_{N_1=0} = -N_2(r-1) + N_2 ln(\frac{z\cdot r}{2}) + N_2(r_2-2)ln(z-1) \tag{1.19}$$

The mixing entropy ΔS_{mix} is the difference between the total entropy and the disordered bulk phase entropy and reads as:

$$\frac{\Delta S_{mix}}{k} = \frac{S_{mix}}{k} - \frac{S_{mix}}{k}\bigg|_{N_1=0} = -N_1 ln(\frac{N_1}{N}) - N_2 ln(\frac{rN_2}{N}) = -N_1 ln\phi_1 - N_2 ln\phi_2 \tag{1.20}$$

with ϕ_1 and ϕ_2 being the volume fractions of the small molecule and the polymer chains, respectively. For a binary blend of two polymers A and B with polymerization degree N_A and N_B an analogous expression is obtained [69, 79]:

$$\frac{\Delta S_{mix}}{k} = -\frac{\phi_A}{N_A} ln(\phi_A) - \frac{\phi_B}{N_B} ln(\phi_B) \tag{1.21}$$

An expression to account for the entropy is found, but another essential part to describe the free energy of mixing is to find an expression for the energetic term in equation 1.15 (Helmholtz free energy upon mixing). The mean-field assumption where every segment experiences an averaged force field on a lattice needs to be used. Neighboring segments have associated interaction energies; ε_{AA} stands for two neighboring A segments, ε_{BB} for two neighboring B segments and ε_{AB} for a segment A next to a segment B. The volume fractions ϕ_i give the average probability of a site being next to another site. The site energy is then defined as:

$$U_{site} = z(\varepsilon_{AA}\phi_A^2 + \varepsilon_{BB}\phi_B^2 + 2\varepsilon_{AB}\phi_A\phi_B) \tag{1.22}$$

To get the energy of mixing, subtraction of the energy of the unmixed state needs to be done, which results in:

$$\Delta U_{mix} = U_{site} - U_{unmixed} = z(\varepsilon_{AA}\phi_A(\phi_A - 1) + \varepsilon_{BB}\phi_B(\phi_B - 1) + 2\varepsilon_{AB}\phi_A\phi_B) \tag{1.23}$$

As already stated in the beginning, each site has to be occupied by one species and the total mixture is incompressible, which means the sum of all volume fractions is 1, $\Sigma_i\phi_i = 1$. The expression for ΔU_{mix} can be simplified as follows:

$$\begin{aligned} \Delta U_{mix} &= \phi_A\phi_B\chi kT \\ \chi &= z(2\varepsilon_{AB} - \varepsilon_{AA} - \varepsilon_{BB})/kT \end{aligned} \tag{1.24}$$

The dimensionless number χ is the famous Flory-Huggins interaction parameter. It describes the energy change of the system when a segment A is taken from a position surrounded purely by segments of A and is placed in a pure environment of B segments and the other way around. Mixing gets energetically unfavorable for χ values larger than 0 and conversely mixing is energetically favorable for $\chi < 0$.

It is now possible to express the equation for the free energy of mixing per lattice site as follows:

$$\frac{\Delta F_{mix}}{kT} = \frac{\phi_A}{N_A} ln(\phi_A) + \frac{\phi_B}{N_B} ln(\phi_B) + \chi \phi_A \phi_B \tag{1.25}$$

This equation is the so called Flory-Huggins equation for free energy of mixing. With this equation it is possible to construct phase diagrams. But first descriptions of the free energy of mixing for the case of a miscible composition and for an immiscible composition need to be found.

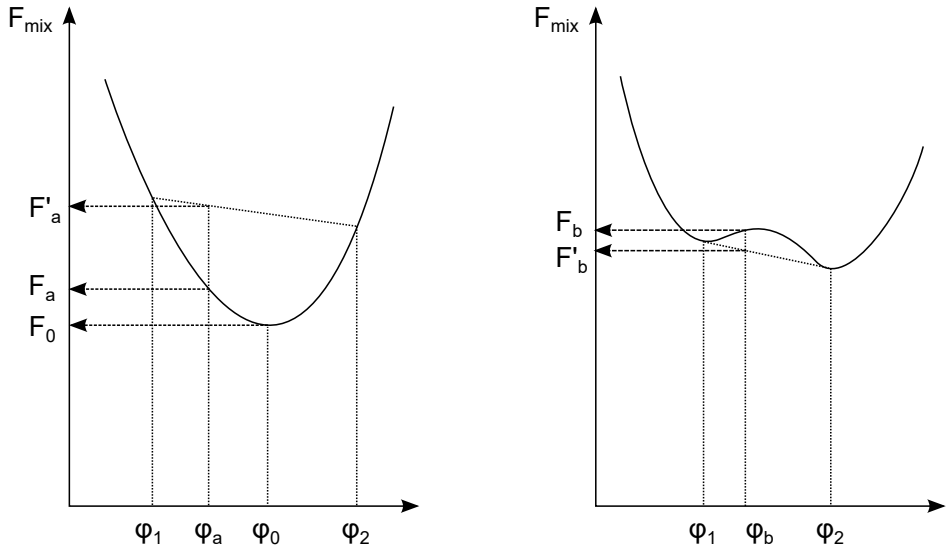

Fig. 1.13 Free energy of mixing for miscible (a) and immiscible (b) systems.

The free energy of mixing in the system can be described as a function of composition as it is shown in figure 1.13. A miscible system is characterized by a single minimum in the free energy curve as shown in figure 1.13 left hand side. A single phase with a composition ϕ_a has a free energy F_a. Every fluctuation of the composition leading to two phases with compositions ϕ_1 and ϕ_2 will lead to an increase in energy, denoted as F'_a. Demixing into two phases is therefore thermodynamically unfavorable. The lowest mixing free energy of the system F'_0 is reached for a single phase composition ϕ_0.

On the other hand, in a system where the free energy curve expresses two minima (see figure 1.13 right hand side) demixing is possible. A homogeneous composition ϕ_b with an energy F_b that is located between the two minima of the free energy curve will undergo separation into two coexisting phases with equilibrium compositions ϕ_1 and ϕ_2 in order to minimize the free energy of the system to a value of F_b'. A tangential line drawn between the two minima defines the region within which a single phase composition is not stable. Between these two limits, the free energy of a single phase has a higher value and is therefore out of equilibrium. The two minima are also called *binodal* points.

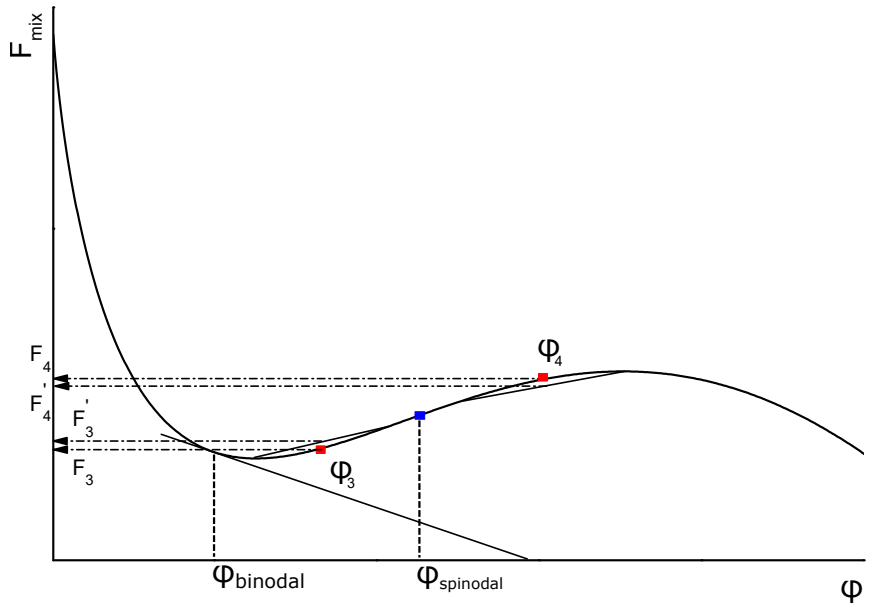

Fig. 1.14 Free energy of mixing in the metastable regime.

Another important part within the coexistence region has to be considered. The curvature of the free energy $\frac{d^2F_{mix}}{d\phi^2}$ is either positive, negative or zero. For compositions ϕ_4 close to the maximum, where curvature is negative, small fluctuations in composition lower the energy and immediately drive the system into a phase separated state (see figure 1.14). This is different for the regions between the minima of the free energy and the points of inflection (positive curvature). Every composition ϕ_3 within these limits is in a metastable state. Small fluctuations in composition lead to a small increase in energy. In effect, to reach global equilibrium an energy barrier needs to be surmounted. The point of inflection where $\frac{d^2F_{mix}}{d\phi^2} = 0$ and this small barrier equals zero is called *spinodal* point.

Another important point is the transition from a system with coexisting phases to a single-phase system. In the upper part of figure 1.15 several free energy curves are plotted as a function of temperature. With increased temperature the free energy curves develop

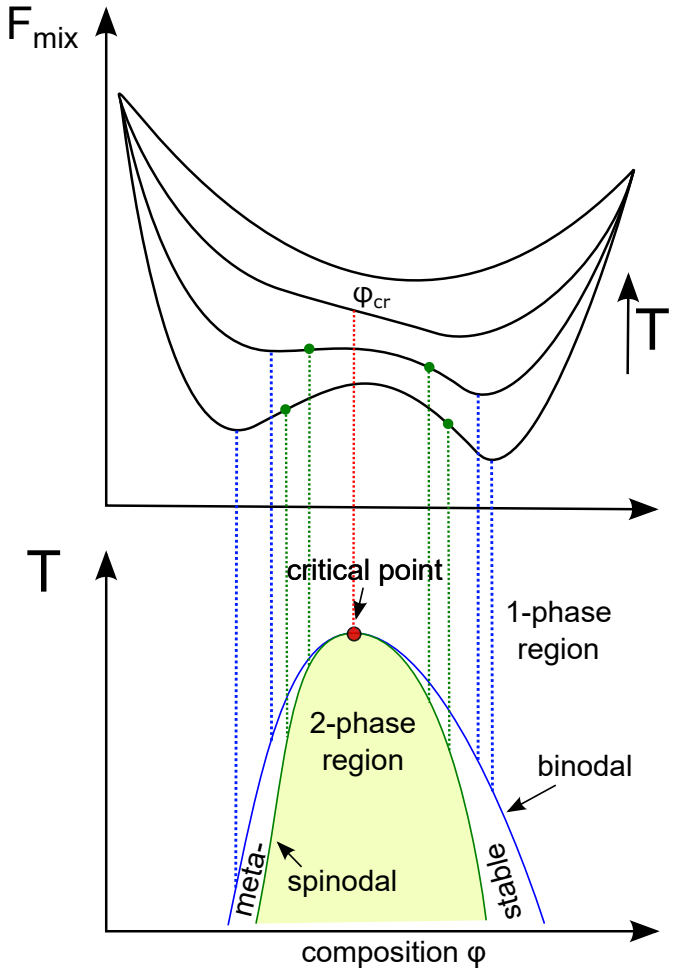

Fig. 1.15 A phase diagram is constructed of binodal and spinodal points of free energy curves at different temperatures. The free energy curve with a flat region (red dashed line) denotes the curve at the critical temperature. It separates the one-phase system (miscibile) from the phase separating system.

from a shape with two minima to a shape with only one minimum at elevated temperature. The curve with a broad flat region (red dashed line) is the free energy curve at the critical temperature T_{cr}. It separates the two situations shown in figure 1.13. The curvature of the free energy is zero at the critical composition ϕ_{cr}, thus a critical point is defined by $\frac{d^3F_{mix}}{d\phi^3} = 0$. Binodal/coexistence and spinodal curve meet at this point.

Translation of all spinodal and binodal points together with the critical point into a temperature as a function of composition plot is done in the lower part of figure 1.15. Thus, a so called *phase diagram* is constructed which summarizes the thermodynamics of polymer mixtures. All binodal points form a binodal line, which separates the one phase region from the 2-phase region. All spinodal points form the spinodal line which denotes the border between the metastable region and the two phase region. The critical point is located at the point where binodal and spinodal line meet.

In figure 1.16 (a) an example of a binary mixture is shown where phase behavior is described as a function of temperature and composition. In a similar way (see figure 1.16 (b)), phase behavior of a binary polymer mixture can be described as a function of solvent content in a ternary phase diagram at constant temperature.

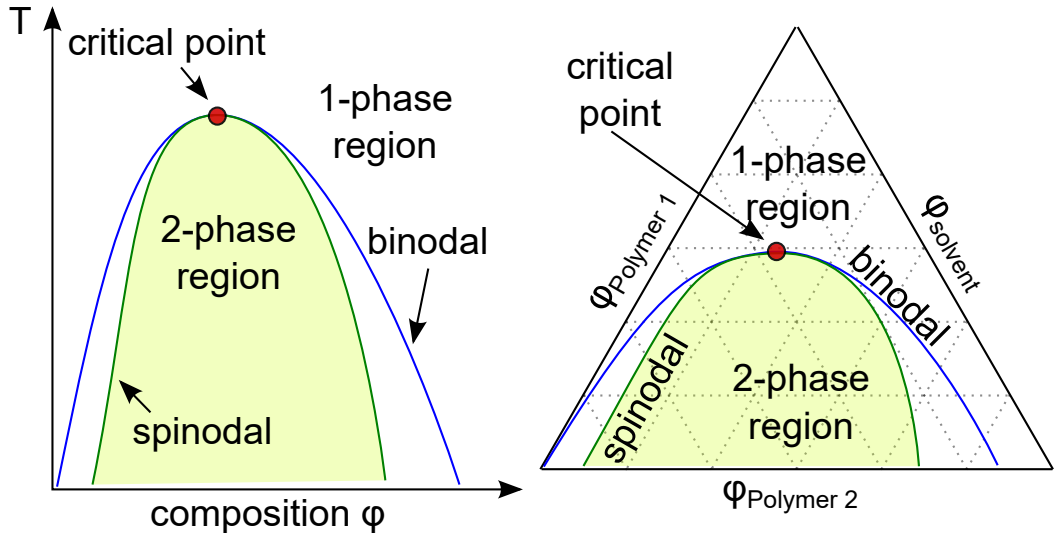

Fig. 1.16 Schematic demonstration of a phase diagram for a binary mixture of polymers as a function of temperature (a) and a binary solution as a function of solvent fraction (b).

Model calculations based on the previously mentioned *Flory-Huggins Theory* are not fully sufficient to quantitatively describe a real polymer system, but they are at least qualitatively embodying the thermodynamics of polymer mixtures. Also, when taking local packing constraints at the polymer segments level into account, an entropic component

to the interaction parameter needs to considered. To date, more refined versions of the Flory-Huggins-Theory did not achieve universal applicability, but included important considerations such as composition dependency of χ [70]. More details and sophisticated thoughts on mixing thermodynamics and derivations of the Flory-Huggins model can be found in [18, 32, 28].

Chapter 2

Morphology of MEH-PPV:PVK Blends

This chapter was published in 2016 as:
Abbaszadeh, D., Kunz, A., Wetzelaer, G. A. H., Michels, J. J., Craciun, N. I., Koynov, K., Lieberwirth, I., and Blom, P. W. M. (2016). Elimination of charge carrier trapping in diluted semiconductors. *Nature Materials*, 15(6):628–633.

2.1 Introduction

Performance of optoelectronic devices such as organic photovoltaics (OPV) and polymer light emitting diodes (PLED) strongly depends on morphological properties of their active layers. Mixing behavior, crystallinity and concentration gradients in polymer blend based devices strongly changes efficiency and overall performance. In this chapter we will discuss how morphology of solution processed active layers in PLEDs evolves from phase dynamics of polymer blends made from poly[2-methoxy-5-(2-ethylhexyloxy)-p-phenylenevinylene (MEH-PPV) and poly(9-vinylcarbazole) (PVK) (see chapter 1.3). In addition, we will show how the intimacy of mixing of the blend constituents will dramatically change charge transport for electrons in the originally trap limited device ultimately improving the current efficiency of blend based PLEDs. All of this will be accompanied by thermodynamic calculations on phase dynamics of the MEH-PPV:PVK blend.

The electrical performance of polymeric semiconductors relies on the charge transport characteristics of the materials used. Charge transport in polymer based devices can be separated into hole and electron conduction. Structural defects and impurities alter transport properties which result in lowering of the mobility and other negative side effects. In a first approach the hole current density is sufficiently well described by the Mott-Gurney-Law [56] within the space-charge-limited regime:

$$J = \frac{9}{8}\varepsilon_0\varepsilon_r\mu_p\frac{V^2}{L^3} \tag{2.1}$$

with μ_p as the hole mobility, ε_0 the permittivity of the vacuum and ε_r the dielectric constant of the polymer. A different description applies to electron transport. In most conjugated polymers electron transport is trap-limited, which dramatically reduces overall efficiency in PLED applications due to strong disparity of hole and electron transport. Though not fully certain, very prominent candidates for traps are chemical impurities. They form energetically localized states inside the band gap of the polymer. The localization of electrons on these electronic states is called trapping. Lampert evaluated in 1956 the influence of discrete trap levels inside the band gap of a semiconductor ([42]). It was found that the current density description by Mott and Gurney had to be modified with an additional factor ϑ:

$$J = \frac{9}{8}\varepsilon_0\varepsilon_r\mu_p\vartheta\frac{V^2}{L^3} \tag{2.2}$$

Lampert's description was discussed for positive charge carries, namely hole transport, but can be equally applied for electrons. The SCLC scales with ϑ, which reads as follows:

$$\vartheta = \frac{p}{(p+p_t)} = \frac{N}{N_t}exp(-\frac{E_t}{kT}) \tag{2.3}$$

p describes the free hole density and p_t the density for trapped holes. N is the density of transport and N_t for trapping sites, with E_t the energy of a hole trap above the edge of the valence band (for electron traps below the edge of the conduction band). The SCLC is reduced by the ratio of free (p) and total hole density, the latter being the sum of free and trapped hole density ($p+p_t$). Traps in polymers are not well described with discrete trap levels. Even for structural defects it has to be assumed that polarization energies for a charge carrier in the vicinity of a defect are different compared to the polarization energy far away from a defect site (perfect lattice) [74]. It means that energetic depth and concentration of traps is not discrete but rather distributed. Mark and Helfrich took the first attempt in 1962 to describe energetic trap states for charge carriers in organic crystals with an exponential distribution [47]. Their description of the relation between trapped and free charge carriers included an effective trap temperature T_t, a discrete trap depth E_{tc} below the edge of the conduction band E_c and reads as follows:

$$\frac{n}{N_c} = \left(\frac{n}{N_t exp(\frac{E_{tc}}{kT_t})} \right)^r \tag{2.4}$$

Combined with the Poisson equation one can derive an expression for the trap-limited current (TLC) as a function of voltage:

$$J_{TLC} = N_c q \mu_n \left(\frac{\varepsilon_0 \varepsilon_r}{q N_t exp(\frac{E_{tc}}{kT_t})} \right)^r \left[(\frac{2r+1}{r+1})^{r+1} (\frac{r}{r+1})^r \right] \frac{Vr+1}{L^{2r+1}} \tag{2.5}$$

With N_c the effective density of states in the conduction band and r the ratio of effective trap temperature and room temperature ($r = T_t/T$). An equally well applying description for J_{TLC} can be given in case of trap states that follow a Gaussian distribution. In that case r has to be modified to account for depth and width of the Gaussian trap DOS [30].

An interesting fact points out when it comes to analyze J_{TLC} described in equation 2.5. The current density for trap-limited charge transport scales with $J_{TLC} \sim N_c/(N_t^r)$. This is very special, as it only applies to trap states that are distributed in energy. For comparison, in the case of discrete trap states scaling goes with $\frac{N_c}{N_t}$, as seen in equation 2.2 and 2.3. The exponent r is missing in the latter. Hence, semi-conducting polymers where $r > 1$ would benefit from reducing N_c and N_t simultaneously. For typical polymeric semiconductors such as poly(phenylenevinylene) (PPV), the exponent r is normally around 4. According to this, a reduction of the density of transport sites N_c and trap sites N_t by a factor of ten, the trap limited current density J_{TLC} in PPV based polymers would increase by three orders of magnitude. The effect of charge trapping in such polymers would be drastically reduced. Although, hole transport would suffer slightly due to the reduced transport site density, disparity of electron and hole transport would diminish to a minimum. The question that arises at this point is: how to lower the density of trap and transport sites practically? For classical semiconductors such as silicon this is not feasible, but for polymer systems blending with an insulator may be the answer. Solution processing of semi-conducting polymer systems opens the possibility to mix two polymers forming a blend and to take advantage of the above-mentioned reduction of N_c and N_t through dilution of the semi-conducting polymer. In a polymer blend of MEH-PPV and PVK the first polymer would act as the semiconductor and the latter a diluent.

The band gap of MEH-PPV lies completely within the bandgap of PVK. The HOMO and LUMO values for MEH-PPV are -5.3 eV and -3.0 eV [12]. In comparison, those of PVK are: -5.8 eV and -2.2 eV, respectively [83]. Holes and electrons that are injected into such a

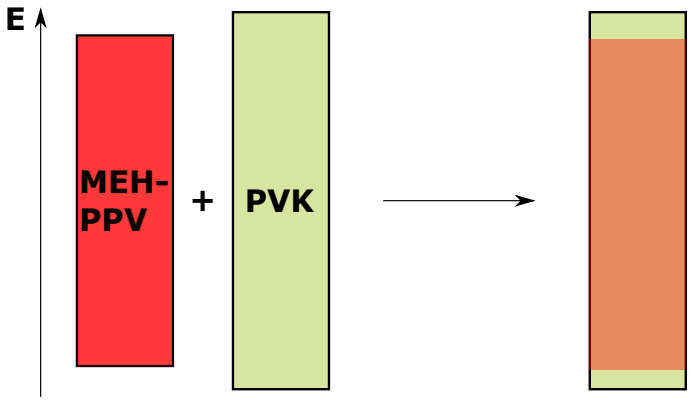

Fig. 2.1 Schematic representation of the energetic band gaps of the low band gap polymer MEH-PPV and the large band gap semiconductor PVK. When mixed in a blend system, the band gap of MEH-PPV lies completely within the band gap of PVK.

polymer blend are transferred directly to MEH-PPV where charge transport occurs. PVK effectively acts as an insulator. Intimate mixing of both components will lead to a reduction of transport and trapping sites of MEH-PPV, with the benefit of reduced negative effect of trapping sites. Nonetheless, at a higher degree of dilution electrical percolation of the semi-conducting polymer will be interrupted and charge transport will be either conducted by the high band gap polymer or not be possible at all. Although one might think that the blending procedure is straightforwardly achievable, some obstacles have to be taken into account. A major problem is the fact that most polymers are not fully miscible with each other. This issue originates from the chemical difference of monomeric units. Each monomeric unit has an interaction energy with its neighboring units and either energetically favors or unfavors them. Furthermore, mixing entropy for polymer blends is rather low due to the macromolecular nature of the molecules [18]. First attempts to account for the thermodynamics of polymer mixtures were described independently in 1942 by Flory and by Huggins [19, 29]. Their model is a description of the thermodynamics of mixing of polymer blends that can be used to qualitatively predict, whether two polymers in a solvent mixture will mix or end up in a demixed state at thermodynamic equilibrium. The free energy of mixing according to their model includes the volume fraction ϕ_i and effective degree of polymerization N_i of each component and reads as follows:

$$\frac{\Delta f_{mix}}{kT} = \frac{\phi_A}{N_A} ln(\phi_A) + \frac{\phi_B}{N_B} ln(\phi_B) + \frac{\phi_C}{N_C} ln(\phi_C) + \chi_{AB}\phi_A\phi_B + \chi_{AC}\phi_A\phi_C + \chi_{BC}\phi_B\phi_C \qquad (2.6)$$

The first three terms of equation 2.6 account for the entropic contribution, whereas the terms including χ account for the enthalpy. χ is the so-called Flory-Huggins interaction parameter. It is a dimensionless number and a free energy parameter that explains the entropic contribution of the interaction between the components:

$$\chi = z(2\varepsilon_{AB} - \varepsilon_{AA} - \varepsilon_{BB})/kT \tag{2.7}$$

With z as the coordination number, k as the Boltzmann constant, T as the temperature and ε_{ij} as the interaction energy of neighboring segments. ε_{ij} describes the energy change of the system when a segment A is taken from a position surrounded purely by segments of polymer A and is placed in a pure environment of polymer B segments. For a polymer blend with $\chi > 0$ the monomeric interaction is effectively repulsive. In contrast, a negative χ represents an attractive mutual interaction between A and B monomers. Since for an amorphous mixture the entropy change is always favorable upon mixing, a blend with a negative χ will never demix. In chapter 1.5 we have explained how to construct ternary phase diagrams according to the theory of Flory and Huggins. *Ternary* in this case means that we take a ternary mixture as a whole considering two polymers and calculate mixing behavior as a function of a third component, namely the solvent fraction in the system. In this chapter we will study the mixing dynamics of the solution processed polymer blend MEH-PPV:PVK as a function of blend ratio and varying molecular weight of the PVK component.

2.2 Experimental

MEH-PPV with a weight-average molecular weight of $\overline{M}_{w,MEH-PPV} = 300$ kg/mol was used. For blend preparation PVK with a weight-average molecular weight of $\overline{M}_{w,PVK} = 30$ kg/mol was used. MEH-PPV:PVK blend solutions were prepared by dissolving the weighed polymers in chlorobenzene and adjusting the weight ratios to 1:0, 1:1, 1:3 and 1:9. Films with thicknesses between 100 – 200 nm were prepared by adjusting the polymer concentration in solution and were spin-coated on prepared substrates. For hole only device preparation, pre-patterned ITO-glass substrates were ultrasonically cleaned in neutral soap solution, acetone, isopropanol and de-ionized water. After drying, the cleaned substrates were activated by applying an UV/Ozone treatment. Subsequently, PEDOT:PSS (Heraeus Clevios 4083) was spin cast from a water based dispersion to form a hole injection layer with a work function of 5.1 eV. After solution casting the MEH-PPV:PVK:CB solution in a glove box atmosphere (nitrogen), a MoO_3 (10 nm) electrode and aluminum protection layer (100 nm) were evaporated through a shadow mask onto the functional polymer blend thin film at a base pressure of $p \approx 10^{-7}$ mbar. Electron only devices were prepared accordingly by sandwiching the polymer blend layer between aluminum (30 nm) and barium (5 nm) electrodes which were thermally evaporated through a shadow mask, capped with a aluminum protection layer. Confocal laser scanning microscopy was done with a Carl Zeiss Axiovert 200 microscope equipped with an LSM 510 module using an -Plan-Fluar 100x oil immersion objective (Numerical Aperture 1.46).
For AFM imaging a Bruker Dimension 3100 setup equipped with a silicon cantilever (300 kHz) in the intermittent analysis mode was used. The software analysis tool Gwyddion v. 2.49 was utilized to plot the acquired AFM raw data.
Transmission scanning electron microscopy images were recorded using a Phillips EM-420 TEM.

2.3 Results & Discussion

In the introduction section 2.1 we hypothesized that charge transport properties of polymer based semiconductor devices can be improved by blending a low band gap semiconductor with a high band gap semiconductor. Electron transport, which dominantly limits the device performance, in such a system would improve dramatically due to the reduced trap and transport site density. According to equation 2.5 the trap limited current of electrons J_{TLC} can be elevated to a three order of magnitude higher value when trap N_{tc} and transport site density N_c are reduced by a factor of ten simultaneously. In order to dilute solution processed semiconductors (*i.e.* low band gap polymer such as MEH-PPV) by blending with an insulator (*i.e.* high band gap polymer such as PVK), it is necessary that the polymers are miscible to some extend, to spatially separate trap and transport sites. But as we have stated in the introduction it can be very challenging to achieve a polymer blend in a fully mixed state. With the help of the *Flory-Huggins Theory* (see chapter 1.5) we can calculate mixing behavior of MEH-PPV:PVK blends in chlorobenzene solution and construct ternary phase diagrams. The phase diagrams will help us to qualitatively predict the mixing behavior and show at which compositions of MEH-PPV, PVK and solvent (chlorobenzene) miscibility or at least only weak segregation into different phases is given. Nonetheless, even within the limits of weak segregation, namely a system of a polymer blend where macro-phase separation takes place but phases are sufficiently well mixed, our hypothesis of reduction of charge carrier trapping should be verifiable. In the case of weak segregation, macro-phase separation results in mixed coexisting or so called binodal phase compositions, where one phase is rich in semiconductor and the other phase rich in insulator. Significant dilution of the semiconductor is true for the insulator rich phase, but nonetheless also the semiconductor rich phase should contribute to improved electron transport. The ideal case of full miscibility, where no macro-phase separation takes place during film casting ending in a single-phase configuration, most likely will only be feasible with low molecular weight polymers ($M_w \ll 20$ kg/mol).

In figure 2.2 we plot four exemplary ternary phase diagrams for the system MEH-PPV:PVK:chlorobenzene, where figure 2.2 a), b), c) and d) represent ternary phase diagrams for blends with molecular weights of $\overline{M}_{w,PVK} = 20$ kg/mol, $\overline{M}_{w,PVK} = 30$ kg/mol, $\overline{M}_{w,PVK} = 60$ kg/mol and $\overline{M}_{w,PVK} = 120$ kg/mol, respectively. All phase diagrams were calculated using the Flory-Huggins theory assuming concentration-independent interaction parameters (see chapter 1.5 on how to construct ternary phase diagrams). Effective degrees of polymerization were obtained by normalizing the weight-average polymer molar volume by that of chlorobenzene (*i.e.* $101\frac{\text{cm}^3}{\text{mol}}$): $N_{MEH-PPV} = 2900$, $N_{PVK} = 400$ (for PVK30), $N_{chlorobenzene} = 1$. Binary Flory interaction parameters (χ_{ij}) were estimated based on the Hildebrand solubility parameters (δ) using: $\chi_{ij} = V_s/RT(\delta_i - \delta_j)^2$ (further discussion on

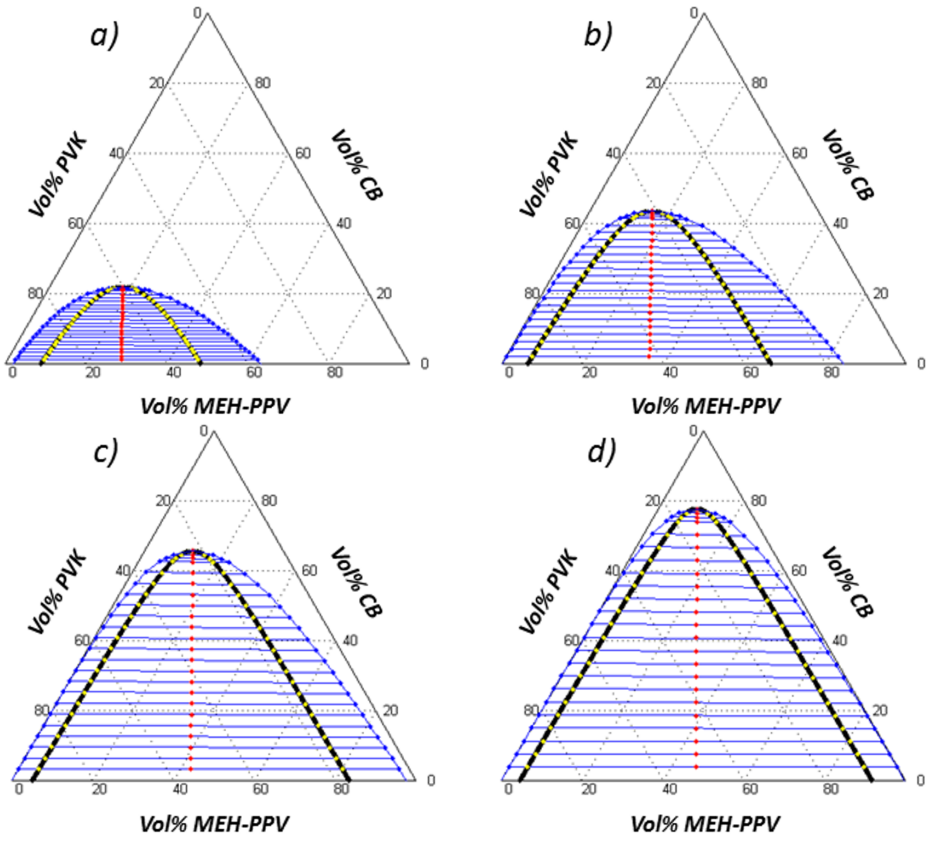

Fig. 2.2 Ternary phase diagrams calculated using Flory-Huggins theory for the blend MEH-PPV:PVK:CB with varying PVK molecular weight: M_w (kg/mol) = 20 (a), 30 (b), 60 (c), and 120 (d); the blue curve represents the binodal, the black curve represents the spinodal, and the thin blue solid lines represent tie-lines; the white area "above" the binodal represents the single phase region

estimation of χ in [44] Chapter 4.2.3), where V_s is the segmental molar volume, here taken to be the molar volume of chlorobenzene. The solubility parameters $\delta_{MEH-PPV} = 18.6\text{MPa}^{\frac{1}{2}}$, $\delta_{PVK} = 19.0\text{MPa}^{\frac{1}{2}}$ (*i.e.* taken similar to that of chloroform), and $\delta_{chlorobenzene} = 19.6\text{MPa}^{\frac{1}{2}}$ were retrieved from reference [15], [61] and [4], respectively. The resulting interaction parameters are: $\chi_{MEH-PPV_PVK} = 4.0 \cdot 10^{-3}$, $\chi_{MEH-PPV_CB} = 3.9 \cdot 10^{-2}$ and $\chi_{PVK_CB} = 1.5 \cdot 10^{-2}$.

During solution casting of binary polymer blends, solvent is reduced continuously from the mixture through evaporation. In a ternary phase diagram this can be represented by an arrow pointing from the top of the triangle (very high solvent fraction) to the polymer blend ratio without solvent (see figure 2.4). The arrow crosses, depending on polymer ratio, the coexistence/binodal line as well as the spinodal at certain spots. Crossing the spinodal line means, that the system phase separates due to lower free energy in the demixed state into phases with compositions that are given through the tie lines- a PVK rich and a MEH-PPV rich phase, respectively. The compositions at the binodal line or between spinodal and binodal are called meta-stable. The meta-stable region is characterized by a coexistence of the homogeneous one phase state and the demixed state. Small local composition fluctuations of the homogeneous mixed state do not immediately phase separate, but rather separate via a nucleation and growth mechanism. The PVK batch that was used in this work with a molecular weight of $\overline{M}_{w,PVK} = 30$ kg/mol shows a relatively small mixing gap (area underneath the coexistence curve (blue) in figure 2.2 (b)). Additionally, the coexistence curve coincides only partially with the edge of the composition domain at the PVK rich side. The MEH-PPV rich side does not coincide at all with the edge. Such a system is a formidable example to study the effects of phase composition and segregation behavior on charge transport. Weak segregation or even a freeze of the one-phase state due to lack of solvent for this system is most likely to occur upon solvent reduction. For blends with higher molecular weight than $\overline{M}_{w,PVK} = 100$ kg/mol we can predict, that drying during device processing (solvent reduction) will lead to phase separation at high solvent contents, where phase compositions overlap with the edge of the composition domains - leading to PVK-rich and MEH-PPV-rich domains that are nearly pure. The desired dilution of the semiconductor would not happen or electrical percolation would not be retained.

We want to go into more detail of the MEH-PPV:PVK:CB phase diagram with PVK having a molecular weight of $\overline{M}_{w,PVK} = 30$ kg/mol shown in figure 2.4. The events occurring during spin coating have to be outlined. At very high solvent content the system resides in the stable single phase region. Ongoing reduction of the solvent during evaporation drives the system into the miscibility gap. When the composition of the ternary blend crosses the binodal line (blue curve in 2.4), two scenarios may happen depending on the ratio of MEH-PPV an PVK used. On the one hand, for the 1:3 blend it is highly likely that during

solvent reduction the blend immediately phase separates due to *spinodal* demixing. The red arrow for this ratio crosses the borders of the mixing gap very close to the calculated critical point, where spinodal (black curve in figure 2.4) and binodal curve overlap. On the other hand, we see that the red arrows for polymer ratios of 1:1 and 1:9, first cross the binodal before entering the spinodal region. Demixing in this case does not necessarily have to happen immediately as the solution might be meta-stable for a short while and prediction of actual point of bifurcation (demixing into two phases) and composition can be difficult. Additionally, successive demixing and domain growth takes place as long enough residual solvent is present to allow for sufficiently high mobility of the polymer chains. The viscosity of the blend diverges with decreasing solvent content, upon which a “frozen” state is obtained wherein mass transport is eventually no longer possible. Global thermodynamic equilibrium is never reached, as the amount of interface between the phases is still relatively high. Considering the relatively large feature sizes in the morphological studies (figures 2.5), the system seems to freeze well within the "late stage" coarsening regime. This means that for all blend ratios local thermodynamic equilibrium is achieved, giving phases with binodal (ternary) composition away from the interface regions. Both the time to drift in the binodal composition and bifurcation point depend on average blend composition. The time is measured between the moment of first reaching the binodal and fixation of the morphology due to viscosity divergence (see figure 2.3 for schematic representation). Finally, the eventual phase composition is different for each blend ratio. In general, increased purity of phases is obtained with a "deeper" quench.

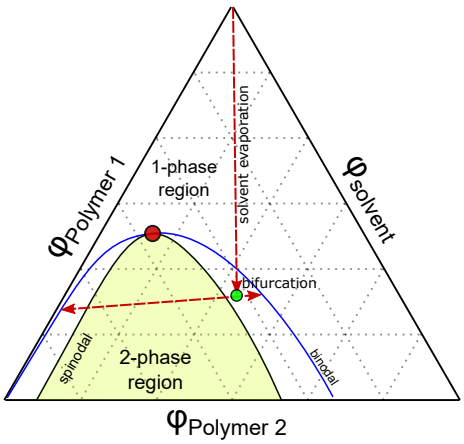

Fig. 2.3 Schematic representation of solvent evaporation and bifurcation in a ternary phase diagram. The red arrow shows the composition change when solvent fraction is reduced due to evaporation. At the bifurcation point two phase separated domains with binodal compositions evolve.

Revealing the blend morphology upon solution casting needs sophisticated techniques with possibilities to resolve features on the micrometer scale as well as slightly below. Microscopic methods that fulfill this condition are scanning probe (SPM) or scanning electron microscopy (SEM). Both of which are mostly imaging surface properties and are somewhat limited when it comes to speak of composition or material contrast. In contrast to that, transmission electron microscopy (TEM) measurements are in principle able to reveal material differences when film thickness is low enough, but chemical identification is weak, especially when both chemical components, as in this study, are of organic nature with chemical properties that are relatively close to each other. Our methods of choice were a combination of several complementary techniques. First, we used atomic force microscopy (AFM) and TEM in order to get high resolution images in the nanometer scale. Additionally, we used confocal laser scanning microscopy (CLSM). The latter technique lacks the ability to produce images with a resolution below the micrometer scale, but it embodies an important advantage. CLSM uses laser light of adjustable wavelength to scan a sample and is therefore capable of selective excitation of one of the components. The excited species can fluoresce, which make it possible to create an optical image of the phase separated morphology. That means, for the blend of MEH-PPV:PVK we can selectively excite MEH-PPV and study phase morphology. Furthermore, together with the topological information acquired using AFM it is possible to roughly estimate the composition of the phases.

Reconsidering the ternary phase diagram in figure 2.4, we prepared four different blend ratios, namely 1:0, 1:1, 1:3 and 1:9 by weight of MEH-PPV:PVK. As already explained previously in this section, the red arrows represent the composition change during solvent evaporation for the different polymer:polymer ratios. Reading the phase diagram reveals that for the chosen ratios macro-phase separation is most likely to occur as in all cases the coexistence curve as well as the spinodal are crossed and the phase separated state is preferred under thermodynamic considerations. Indeed, the AFM images in figure 2.5 clearly reveal the blend to macro-phase separate into two morphological domains.

Height differences between domains typically amount to a few tens of nanometers on total film thicknesses of 200 – 300 nm. With increasing PVK concentration domains with larger thickness increase in area, signifying that the dispersed phase is PVK-rich. We note that phase inversion takes place when comparing figure 2.5 c) and d), which correspond to blend ratios of 1:3 and 1:9, respectively. Since AFM is a surface sensitive measurement technique and scans the domain structure only at the top surface, we made TEM images to better image the bulk of the layer.

In figure 2.6 TEM images for the blend ratios 1:3 and 1:9 are shown. The morphology appears in similar shaped features as already shown by AFM. TEM does not allow for height

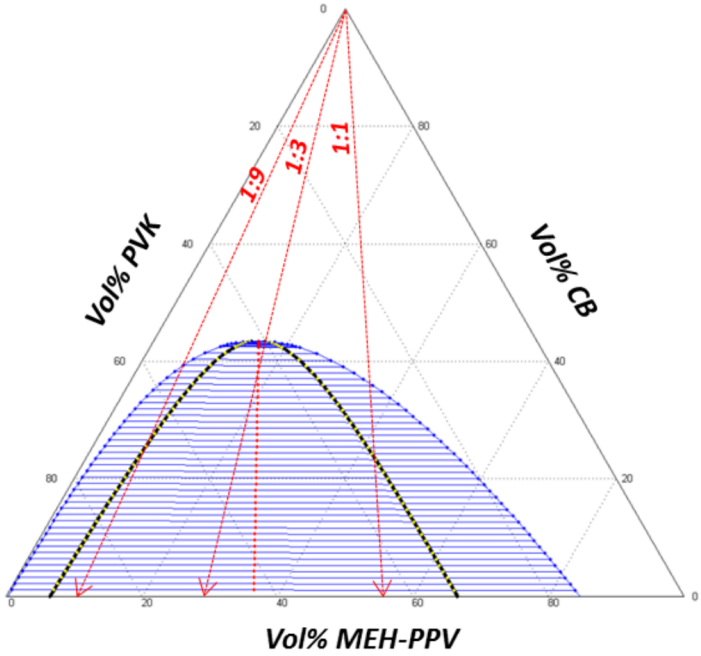

Fig. 2.4 Ternary phase diagram of the blend system MEH-PPV:PVK:CB for $M_{w,PVK}$=30 kg/mol. The red arrows represent the change in composition during solvent evaporation for different polymer ratios.

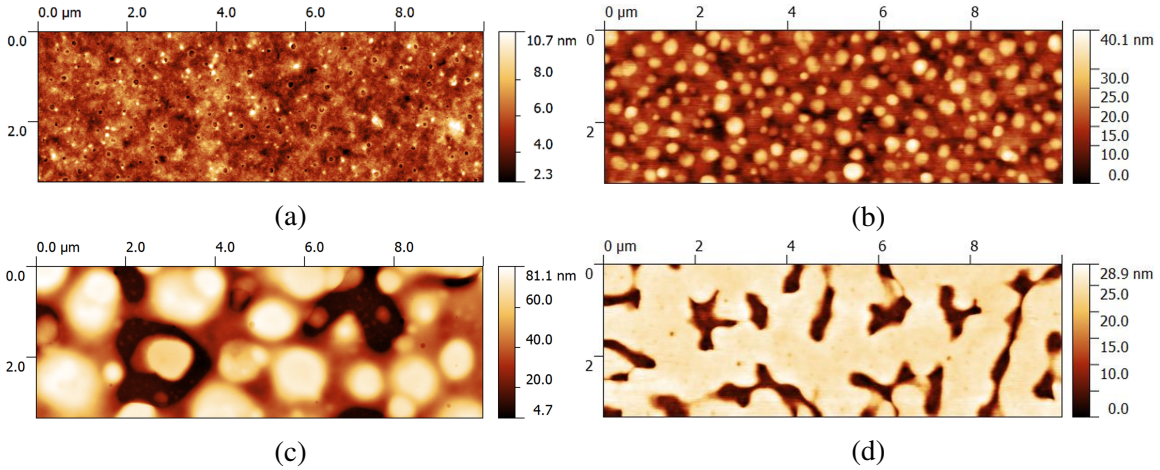

Fig. 2.5 AFM images taken from MEH-PPV:PVK thin films with blend ratios of (a)1:0, (b)1:1,(c) 1:3 and (d)1:9.

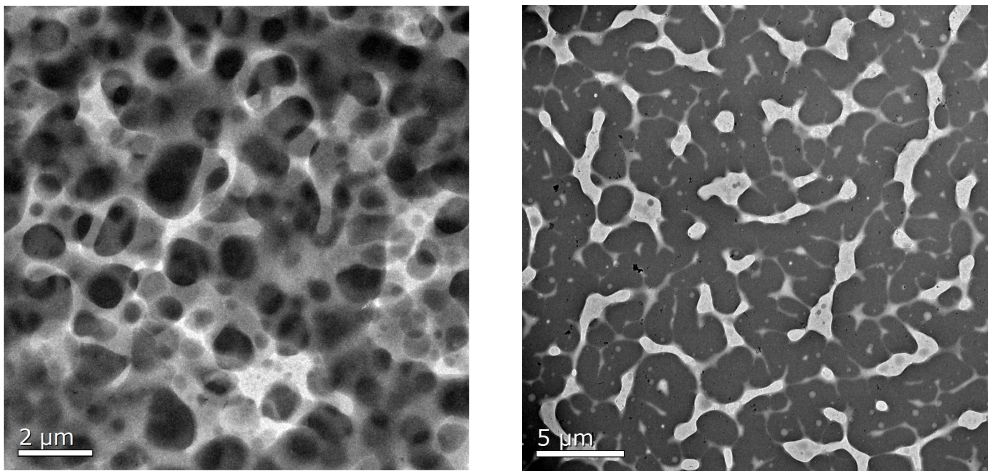

(a) (b)

Fig. 2.6 TEM images of MEH-PPV:PVK thin films with blend ratios of (a)1:3 and (b)1:9

determination. Instead, it confirms that the domain structure not only concerns the top surface, but extends throughout the bulk of the film. In addition, we use CLSM to probe local fluorescence intensity in order to study the spatial distribution and concentration of MEH-PPV in different domains of the blend film.

With increasing amount of PVK the PVK-rich domain changes from dispersed (1:1 and 1:3 blends) to continuous (1:9 and beyond). The MEH-PPV-rich phase exhibits the opposite trend. When it comes to comparing all representations of the phase morphology, all images acquired by AFM, TEM and CLSM are internally fully consistent. As mentioned above, in order to answer the question whether the PVK-rich domain contains a fraction of MEH-PPV (as suggested by the phase diagram in Figure 2.4), also CLSM qualifies as analysis technique. The dark PVK-rich regions of the morphology images reveal residual fluorescence at normal (Figure 2.8 a) as well as increased (Figure 2.8 b) excitation intensity. In contrast, we show that after bleaching part of the film (Figure 2.8 c) residual emission is absent. This shows that backscattered excitation light is too low in intensity to be detected, so that we can safely conclude that the low-intensity emission from the darker phase is due to a minority fraction of MEH-PPV in the PVK-rich phase.

In the further course of the discussion, we want to analyze the composition of the individual phases in a more quantitative assessment. We first determine the effective volume of the PVK- and MEH-PPV-rich phases from CLSM and AFM data as shown in figure 2.5 and figure 2.7. The effective surface area of each phase is determined using the image analysis software ImageJ 1.49v. The volume of each phase was then calculated by multiplying its surface area with the average height, as estimated from the corresponding AFM image. By

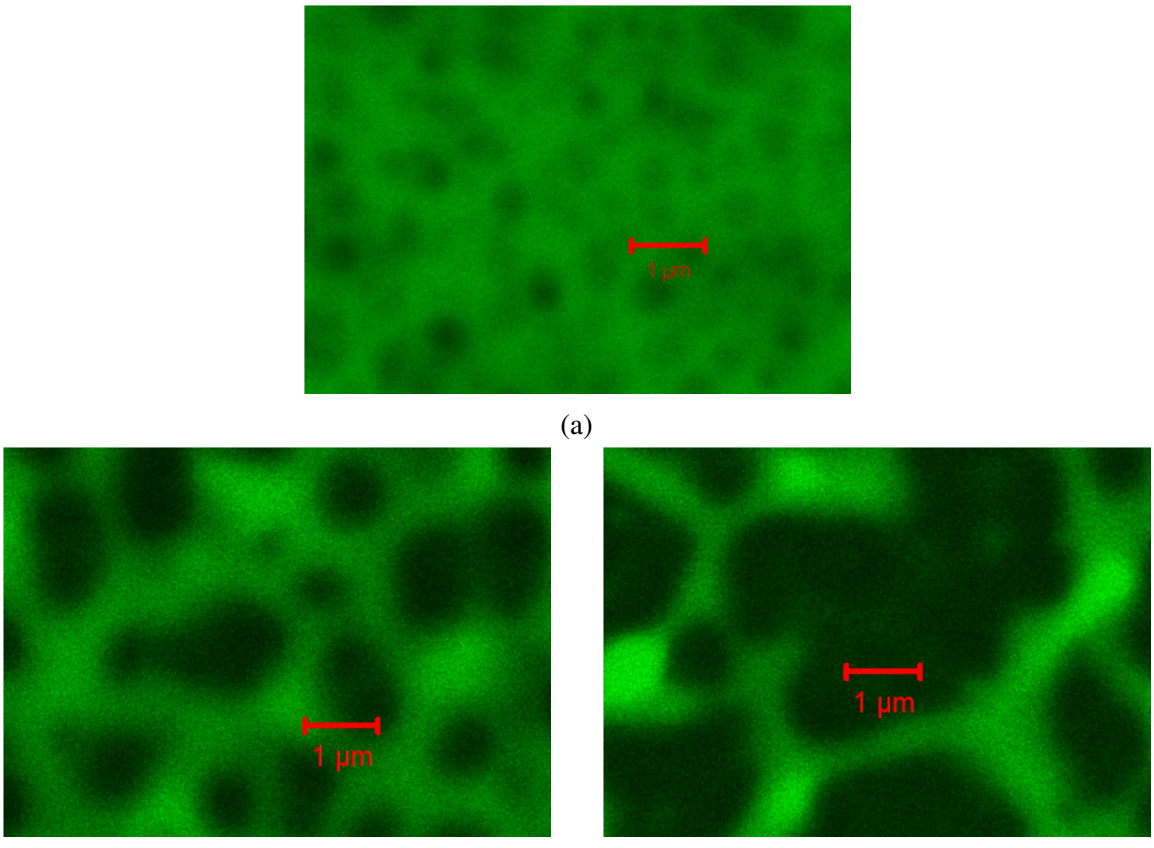

(a) (b) (c)

Fig. 2.7 CLSM images of MEH-PPV:PVK thin films with different polymer weight ratios. (a)1:1, (b) 1:3, (c) 1:9. Green domains denote MEH-PPV-rich phases and darker domains denote PVK-rich phases.

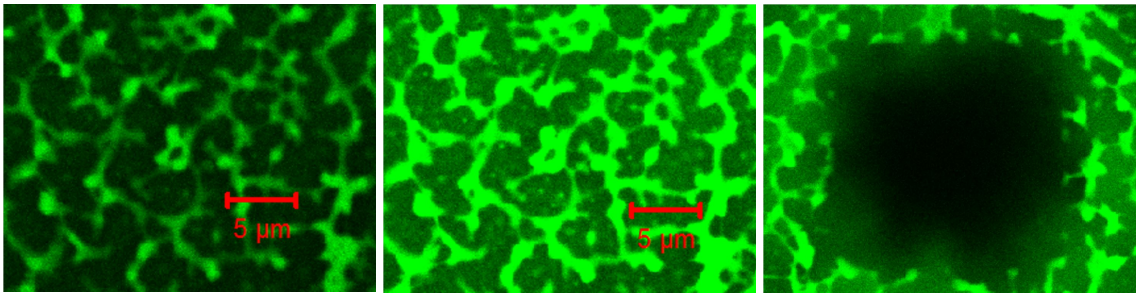

(a) (b) (c)

Fig. 2.8 CLSM images of MEH-PPV:PVK 1:9 thin films, recorded under excitation with 488 nm laser light at normal (a) and elevated intensity (b). Image (c) represents an area with deliberately bleached region to show that the detected emission is not contaminated with backscattered excitation light. Intensity of fluorescent light emitted by the MEH-PPV is expressed by the green color scale and therefore a direct measure for the local concentration of low band gap polymer.

doing this exercise, we can provide a range of possible compositions for both phases. For all three blends (1:1, 1:3 and 1:9 MEH-PPV:PVK), the volume of the MEH-PPV phase undercuts the respective volume ratio of the polymer blend. Under the assumption that the MEH-PPV-rich phase consists of pure PPV (100%) the lower limit for the MEH-PPV concentration range in the PVK-rich phase was obtained. The remainder of the MEH-PPV is then assumed to be mixed in the PVK-rich phase. Naturally, an estimate of the MEH-PPV fraction in the PVK-rich phase has to be a lower limit, since the MEH-PPV-rich phase according to the binodal line in the phase diagram (figure 2.4) also contains PVK. Furthermore, the respective average volume fraction of MEH-PPV in the blend is considered as upper limit of MEH-PPV fraction in the PVK-rich phase, which would correspond to absence of phase separation. By following this procedure a lower limit of 5 and 11% for the 1:9 and 1:3 MEH-PPV:PVK blends were determined, respectively. The upper limits logically amount 10 and 25%. Considering the calculated phase volume ratio of the dry film and the intensity ratio of emitted light in the CLSM images, a calculation of the solvent fraction at which the morphology effectively vitrifies is possible. Reconsideration of the ternary phase diagram and replotting it in figure 2.9 visualizes the change in blend composition during solvent evaporation indicated by the colored arrows (red for 1:1, green for 1:3 and blue for 1:9). From the corresponding points of bifurcation, marked in green and blue for polymer ratios of 1:3 and 1:9, respectively, and the corresponding end points of the tie-lines on the binodal curve (blue) the composition of both phases is determined. For the 1:9 MEH-PPV:PVK blend the MEH-PPV fraction in the PVK-rich phase and the PVK fraction in the MEH-PPV-rich phase amount to 7 and 25%, respectively. The same procedure was followed for the 1:3 blend ratio, leading to a MEH-PPV fraction of 18% in the PVK-rich phase. Unfortunately, this method could not be applied to the 1:1 blend due to lack of optical contrast in the CLSM image (see figure 2.7). The PVK-rich domains are considerably smaller for this blend than for the other two, which leads to the assumption that charge transport will approach that of a homogeneous mixture, which in effect is also true for the other two blend ratios. The MEH-PPV fraction in the PVK-rich phase gradually increases with MEH-PPV:PVK blend ratio (higher MEH-PPV content in the blend).

In order to investigate charge transport behavior in the MEH-PPV:PVK blend, single carrier devices were fabricated by confining the semiconductor or the blend films between two high work function electrodes or two low work function electrodes, one forming a hole-only (HO) device and the other an electron-only (EO) device, respectively (see more information on single carrier devices in chapter 2.2). In figure 2.10 current-voltage (*JV*) characteristics of MEH-PPV:PVK blend based HO and EO devices are shown. We want to

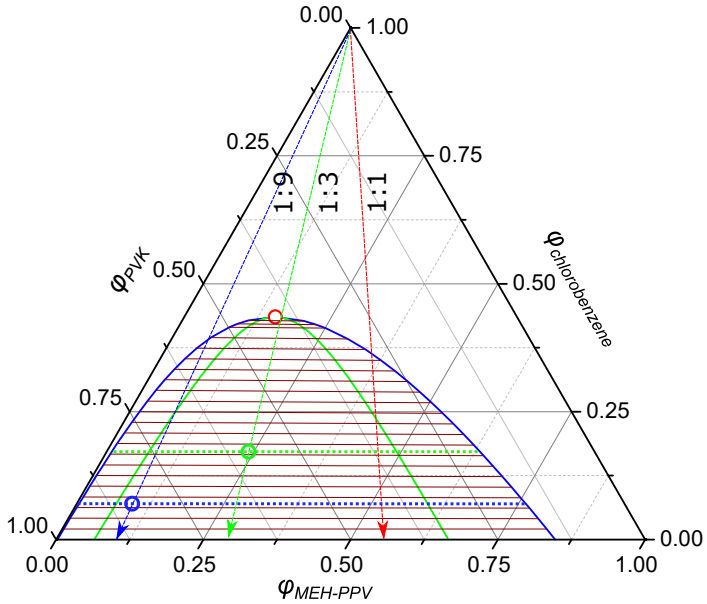

Fig. 2.9 Ternary phase diagram of the blend system MEH-PPV:PVK:CB for $M_{w,PVK}$=30 kg/mol. The colored arrows represent the change in composition during solvent evaporation for different polymer ratios. The green and blue dashed lines represent the tie lines that correspond to the marked bifurcation points (green and blue dot). A red tie line and a red bifurcation point corresponding to the 1:1 MEH-PPV:PVK blend cannot be drawn as optical contrast for composition determination in figure 2.7 is missing. Binodal compositions at the ends of each tie-line amount to equal chemical potential and determine coexisting, separated phases.

verify the effect of dilution by comparing the charge transport properties in single carrier devices.

The black solid lines in figure 2.10 are a fit of the hole current to the SCLC. Accordingly, black dots are measured experimental values for the hole current density. Red dots are measured experimental values for the electron current density. Solid red lines are a fit of the electron current density to the trap limited current density equation 2.5, where the mobility is calculated using the extended Gaussian disorder Model (EGDM, see the end of chapter 1.1). The inset numbers in figure 2.10 (a)-(d) show simulation parameters for the trap limited current densities of electrons. Electron transport through MEH-PPV is strongly trap limited as seen in figure 2.10 (a). The current density for electrons is almost three orders of magnitude lower than the one for holes.

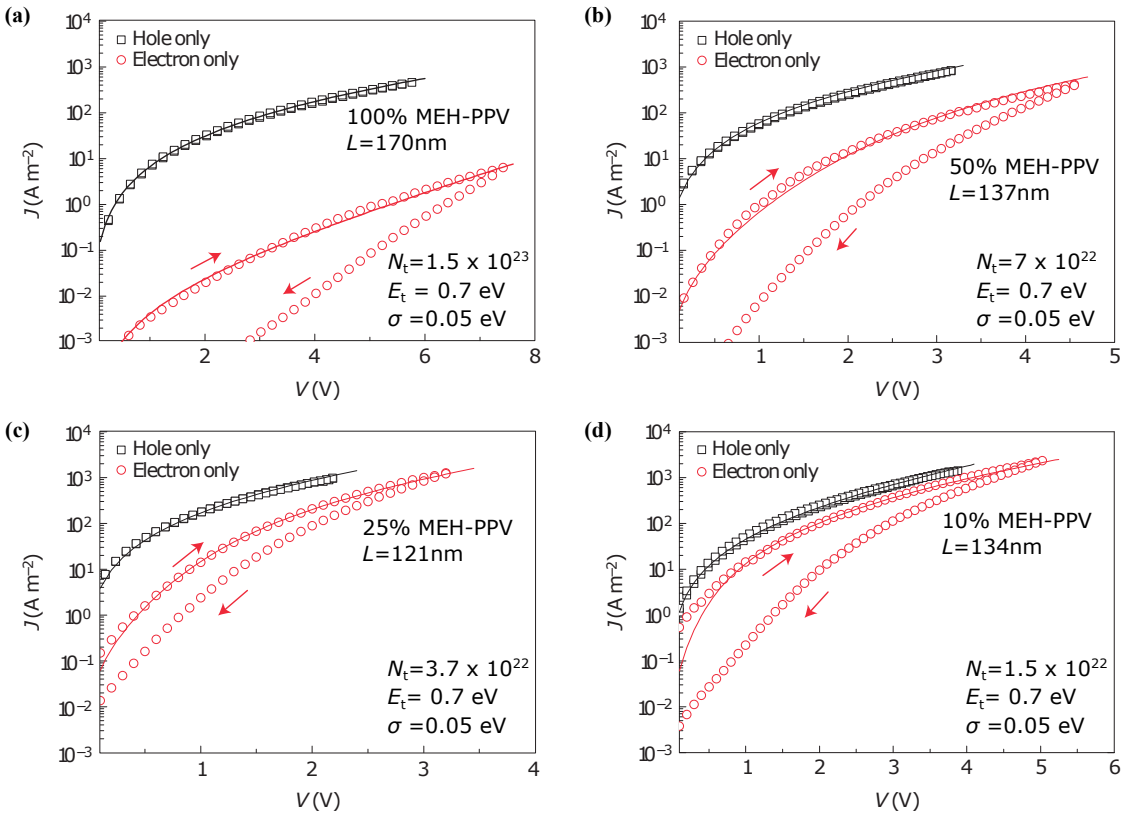

Fig. 2.10 Hole and electron current density as a function of applied voltage for MEH-PPV:PVK single carrier devices with MEH-PPV fractions of (a) 100 wt%, (b) 50 wt%, (c) 25 wt% and (d) 10 wt%. Reproduced with permission from [1].

The situation is dramatically changed when the fraction of PVK in the MEH-PPV:PVK blend is increased. Injection and transport of electrons will take place only in MEH-PPV as the LUMO value of PVK is higher in energy. In figure 2.10 (b) to (d) the electron current

densities increase gradually with increasing weight fraction of PVK, from 50%, over 75% to 90%, respectively. Current densities for holes and electrons in MEH-PPV:PVK in a 1:9 ratio are almost on top of each other demonstrating the trap-limited nature of the electron transport to be effectively eliminated by blending with PVK. Reconsidering the parameters used to simulate the electron current densities, we can see that the trap density N_t is the only fitting parameter which needs to be changed in order to acquire a reasonable agreement between the fit and experimental values. Furthermore, N_t follows the adjusted weight ratio of the polymers in the respective blends. That means, compared to a pristine MEH-PPV based EO-device with a trap density of $N_t = 1.5 \cdot 10^{23}$, N_t for the blend based EO-devices is reduced by a factor of ≈ 2, ≈ 4 and 10, for the 1:1, the 1:3 and the 1:9 blend, respectively. Nonetheless, it has to be mentioned, that the hysteresis loop which is caused by deep trap states for electron currents cannot be eliminated. Deep trap states in polymeric semiconductors have a different chemical and physical origin than the energetically distributed trap states discussed in this work. The energetic distribution for deep trap states is rather discrete in nature, which makes it difficult to effectively reduce their negative contribution to charge transport of electrons through dilution with an insulating host material. Further discussion on how to eliminate the hysteresis loop is conducted by Craciun et al. in [16].

Holes that are transported through the active layer, whether the homopolymer or the blend system, are well described by trap free charge transport according to the SCLC in equation 2.1. Hole transport does not suffer with increasing the fraction of PVK in the blend, but rather stays unchanged or is even increased. The increase of hole transport could be explained by enhanced molecular ordering, avoiding ring-like structures as reported earlier for the very similar polymer MDMO-PPV blended with PCBM [37]. The weakly ordered stacking of asymmetrically substituted polymers in ring-like structures might be hindered by the presence of low M_w PVK leading to enhanced charge transport properties with decreased energetic disorder [1].

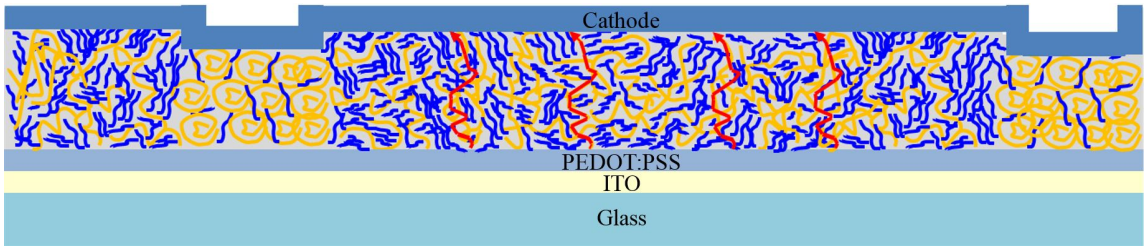

Fig. 2.11 Schematic representation of the blend morphology and dominant charge transport path in MEH-PPV:PVK. MEH-PPV is indicated in orange and the host material in blue. Red arrows indicate the dominant current path.

The combined results of charge transport, morphology and phase diagram investigations lead to a schematic representation for the charge transport in MEH-PPV:PVK blend films as seen in figure 2.11. Phase separation into MEH-PPV-rich and PVK-rich domains occurs during the deposition of MEH-PPV:PVK blends from solution due to their partial miscibility. PVK-rich domains result in slightly higher thickness. Simultaneously, the energetic disorder of MEH-PPV in the latter domains is reduced leading to enhanced mobility for holes and reduced trap density N_t for electrons. With increased PVK fraction, PVK-rich domains start to grow in area which results in an enhancement in total current density through in blend. We note, the desired dilution effect occurs in PVK-rich domains that also provide the dominant current path. The increase in electron current (decrease in trap density N_t) scales with the average PVK fraction and results in almost equivalent hole and electron current for the 1:9 MEH-PPV:PVK blend.

2.4 Conclusions & Outlook

In summary, we have shown that dilution of MEH-PPV by blending it with a high band gap semiconductor such as PVK leads to a reduced density of trap states in blend based devices. The reduced density of trap states eliminates the negative effect of trap states. As a result, balanced charge transport for holes and electrons could be achieved. In order to achieve proper reduction of trap states, the mixing behavior of the MEH-PPV:PVK blend had to be studied, where in first place, calculations on ternary phase diagrams of the blend system MEH-PPV:PVK:chlorobenzene were done. The conclusion was: ideally, phase separation in polymer blends should be avoided in order to have proper dilution characteristics. But this certain polymer blend was identified to be "on the border", as phases are segregated though still mixed inside the segregated domains. With molecular weights of MEH-PPV with $\overline{M}_{w,MEH-PPV} = 300$ kg/mol and PVK with $\overline{M}_{w,PVK} = 30$ kg/mol the blend is a formidable example to study the effects of phase composition and segregation behavior on charge transport characteristics simultaneously. The ternary phase diagram calculations were supported by experimental imaging techniques, such as AFM, TEM and CLSM. Morphological properties of the polymer blend thin films could be sufficiently well investigated to identify the composition at which the polymer blends effectively vitrify. It was found that electrical percolation could be sustained even for PVK-rich domains reaching a minimum MEH-PPV fraction as low as 7% for the MEH-PPV:PVK 1:9 blend. Current-Voltage characteristics of single charge carrier devices were recorded and subsequently simulated by the EGDM to show the increased electron current density with decreased trapping density for blend films retaining an increased PVK-fraction. Ultimately, it was demonstrated that for MEH-PPV:PVK thin

film devices with weight ratios of 1:9 hole and electron current densities are almost equal and trapping behavior for electrons is effectively eliminated. The trap density, according to conducted JV simulations, almost linearly decreased with the amount of MEH-PPV in the blend. Charge transport, despite the occurring phase separation, approached that of a homogeneous mixture of the polymer blends.

As an outlook for further studies, we recommend to investigate a polymer blend system where the mixing gap of the system is very small or even absent in order to get fully mixed polymer blend thin films as active layer for charge transport. Furthermore, a host material with even a higher band gap, a real insulator, could be used to clearly separate charge transport characteristics from phase behavior.

Chapter 3

Charge Carrier Trapping Controlled by Polymer Blend Phase Dynamics

This chapter was published in 2017 as:
Kunz, A., Blom, P. W. M., and Michels, J. J. (2017). Charge carrier trapping controlled by polymer blend phase dynamics. *J. Mater. Chem. C*, 5:3042–3048.

3.1 Introduction

Notably, we observed reduced electron trapping despite the fact that the MEH-PPV:PVK blend exhibited pronounced macro-phase separation during solution casting. This is surprising at first glance, as it is understood that the necessary spatial separation for the dilution of adjacent trapping sites should rely on intimate mixing of semiconductor and host at the segmental level, rather than dispersion on macroscopic length scales. We explained the fact that the electron current increased nonetheless, by assuming that for the MEH-PPV:PVK blend under consideration demixing occurred in the limit of weak segregation. This implies that under thermodynamic control the phase domains comprise mixed phases containing both polymers, be it one in excess to the other. The occurrence of macro-phase separation itself was demonstrated by microscopy analysis, where the typical drop-like shapes convincingly showed phase separation to have occurred via liquid–liquid demixing. In this respect the choice of PVK as polymeric host material to dilute a polymeric semiconductor was a little unfortunate, as polymers are usually difficult to mix due to the low mixing entropy [18].

In this work we elaborate on the miscibility of insulating host and semiconducting guest and demonstrate that we can actually control the dilution of the electron traps once the thermodynamics of the ternary blend of semiconductor, host and solvent is properly

understood. Using Flory–Huggins theory we show that the blend's calculated phase diagram represents a qualitative but effective means to predict whether the electron current in the dry blend material would increase upon mixing due to dilution. For the present study we choose polystyrene (PS) as insulator, not only owing to its availability in a range of molecular weights, but also to prove the generality of our method of increasing OLED device performance by dilution. By comparing the present results with the mentioned recent findings on MEH-PPV:PVK blends [1], we show that the phase composition, rather than the question whether or not macro-phase separation occurs during solution casting, provides for the deciding argument governing the elimination of electron trapping.

3.2 Experimental

Poly[2-methoxy-5-(2-ethylhexyloxy)-1,4-phenylenevinylene] (MEH-PPV) with a weight-average molecular weight of $\overline{M}_{w,MEH-PPV} = 354$ kg/mol and a polydispersity index (PDI) of 4 was synthesized according to the Gilch route [21]. Polystyrene (PS) samples $\overline{M}_{w,PS} =$ 35 kg/mol, PDI = 1.09 and $\overline{M}_{w,PS} = 1.1$ kg/mol, PDI = 1.15) were synthesized in house via anionic polymerization of styrene. In this work these PS samples are respectively named "PS35" and "PS1", the number index referring to their weight-average molecular weight. MEH-PPV:PS blend solutions were prepared simply by dissolving weighed amounts of the polymers in chlorobenzene. Semiconductor-to-polystyrene weight ratios of 1:0, 1:1, 1:3 and 1:9 were used. Polymer concentrations were tuned so as to obtain a final dry film thickness of ~ 200 nm.

For the fabrication of hole-only (single carrier) devices (HO, Fig. 3.1 (a)) and polymer light-emitting diodes (PLEDs, Fig. 3.1 (c)), glass–ITO substrates were cleaned using neutral soap and successively rinsed with de-ionized water, acetone, and 2-propanol. Each cleaning or rinsing step was performed for 10 min in an ultrasonic bath. Cleaned substrates were activated in UV-Ozone for 20 minutes for better wettability as well as removal of organic contaminants. A 55 nm thick film of poly(3,4-ethylenedioxythiophene)polystyrene sulfonate (PEDOT:PSS) (Heraeus Clevios 4083) was applied on top of the ITO layer by spin-coating from aqueous dispersion and subsequent annealing at 140° C for ten minutes.

The substrates for electron-only (single carrier) devices (EO devices, Fig. 3.1 (b)) were fabricated using a slightly oxidized aluminum electrode as bottom contact, which was deposited onto the glass slide through a shadow mask by thermal evaporation. A ~ 200 nm thick layer of the light-emitting polymer (LEP) or polymer blend was spin-coated on top of the PEDOT:PSS (HO devices and PLEDs) or aluminum oxide (EO devices). For the PLEDs and the EO devices a top electrode of barium (nominally 5 nm) covered with 100 nm

aluminum was evaporated through a shadow mask. Top electrodes for the HO devices were fabricated by evaporating 10 nm MoO_3, followed by a 100 nm Al capping layer.

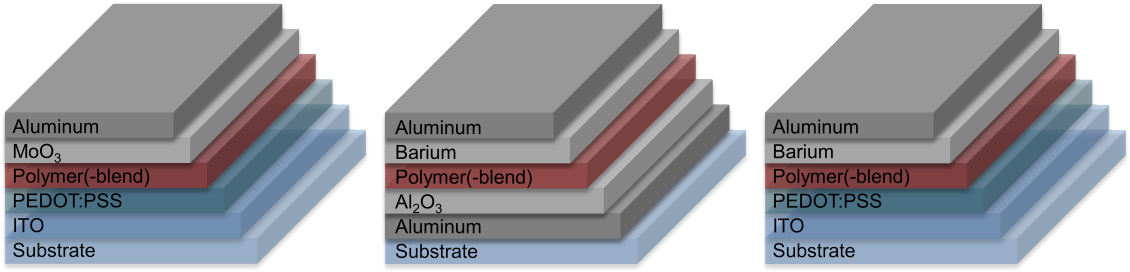

(a) (b) (c)

Fig. 3.1 Schematic cross-sectional images displaying the architecture of single and dual charge carrier devices used for electrical characterization: (a) hole-only, (b) electron-only, (c) dual carrier (OLED).

3.3 Results & Discussion

Many examples exist in literature where details on phase dynamics and morphology of semiconducting and electroactive blends provide for an *a posteriori* explanation of electronic phenomena observed on the device level [45, 38, 52, 82, 66, 81]. Here, we take the inverse approach and show that *a priori* estimation of a blend's phase behavior based on thermodynamic considerations can be used to predict optoelectronic behavior. We hence commence with calculating the ternary phase diagrams for the MEH-PPV:PS:chlorobenzene blends using Flory–Huggins theory [18]. In order to tune the miscibility between semiconductor and insulator, two different PS samples are considered (see Experimental section 3.2), one with a 'high' molecular weight, $\overline{M}_{w,PS} = 35$ kg/mol (denoted PS35), and one with a low molecular weight, $\overline{M}_{w,PS} = 1.1$ kg/mol (denoted PS1). Analogously, we here name the previously reported PVK-based sample "PVK30", the number index referring to: $\overline{M}_{w,PVK} = 30$ kg/mol [1]. Details on the calculations of the ternary phase diagrams can be found in the Appendix 3.5.

The phase diagrams calculated for the corresponding ternary blends are presented in figure 3.2 (a) and (b), together with the one for the recently studied MEH-PPV:PVK30:chlorobenzene blend (figure 3.2 (c)). The limit of full miscibility is indicated by the binodal curve (solid blue line) above which a stable, single phase exists. In the region below the binodal, the miscibility gap, a driving force for demixing is present. For mean blend compositions beneath the greenline, *i.e.*, the spinodal, demixing is spontaneous. The positive tilt in the lines connecting the compositions of coexisting phases ("tie-lines", brown), observed in figure 3.2

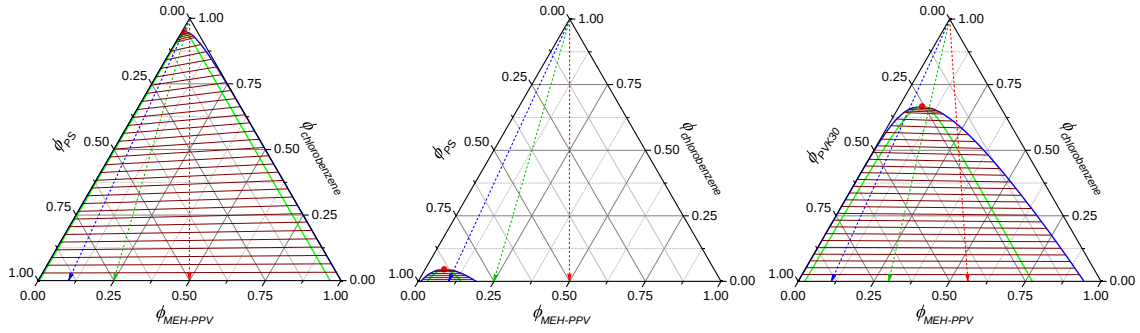

(a) (b) (c)

Fig. 3.2 Ternary phase diagrams of the blends MEH-PPV/PS35/chlorobenzene (a), MEH-PPV/PS1/chlorobenzene (b) and MEH-PPV/PVK30/chlorobenzene (c), calculated using Flory–Huggins theory (see Appendix); the blue and green curves represent the binodal and the spinodal lines, respectively; the red symbol denotes the critical point and the brown lines ("tie-lines") connect the binodal compositions of coexisting phases. The dashed red, green and blue arrows indicate the change in overall composition upon solvent evaporation for a 1:1, 1:3 and 1:9 MEH-PPV:insulator weight ratio

(a), is a consequence of MEH-PPV having a more favorable interaction with the solvent than polystyrene has (see Appendix 3.5). In contrast, figure 3.2 (c) reveals hardly any solvent partitioning when using PVK instead of PS.

Comparing the phase diagrams in figure 3.2 (a) and (b) shows that the size of the miscibility gap strongly depends on polystyrene molecular weight:[1] whereas it covers almost the phase diagram in case of PS35, it is (nearly) absent for PS1. The difference is explained by the increase in statistical entropy upon decreasing molecular size. Figure 3.2 (c) shows that the MEH-PPV:PVK30:chlorobenzene blend has a miscibility gap of intermediate size.[2] The fact that it is smaller than the one for MEH-PPV:PS35:chlorobenzene, despite the similar insulator molecular weight, is mainly a result of the less repulsive interaction between semiconductor and insulator (see Appendix 3.5).

During solution-casting of the blend, the mean polymer concentrations continuously increase due to on-going solvent evaporation. The mean composition-trajectory followed as a consequence of solvent evaporation is indicated in each phase diagram by the dashed arrows. The color of the arrows corresponds to different semiconductor:insulator weight ratios: 1:1 (red), 1:3 (green) and 1:9 (blue). Initially, all compositions lie in the single phase region above the binodal. Once evaporation pushes the composition into the miscibility

[1] The molecular weight of the MEH-PPV is not varied throughout this study.

[2] The miscibility gap of the MEH-PPV:PVK:chlorobenzene blend is somewhat larger than reported earlier (see reference [1]), as in the present study the input parameters for the Flory–Huggins model were calculated in a slightly different, however more consistent, manner.

gap phase separation may occur if the solvent fraction remains high enough to allow for sufficient molecular mobility. During evaporation the viscosity of the solution rises steeply as the polymer concentration increases. Eventually, mass transport completely arrests upon which the blend film solidifies, irrespective of phase separation to have occurred or not. This implies that the smaller the miscibility gap, the lower the probability of significant demixing to occur prior to solidification.

Considering the above, for the MEH-PPV:PS1:chlorobenzene blend thermodynamic as well as kinetic arguments can be given for the polymers to remain mixed during film formation. In contrast, in case of MEH-PPV:PS35:chlorobenzene demixing is highly likely considering the very large miscibility gap. In this case even at high solvent concentrations a strong driving force for spontaneous demixing exists, irrespective of the polymer:polymer ratio. Furthermore, the fact that the binodal branches largely coincide with the axes of the composition domain suggests phase separation to result in virtually pure phases of MEH-PPV and PS35. Admittedly, due to the, at best, semi-quantitative nature of the Flory–Huggins model we cannot calculate the exact phase compositions. The important thing however is that the model predicts that should demixing result in a PS35-rich phase containing a residual amount of MEH-PPV, it is likely too little to overcome the percolation threshold for charge conduction. *Vice versa*, a possible residual fraction of PS35 in the MEH-PPV-rich phase is probably too small to cause noticeable trap dilution.

Again, also with respect to phase composition the PVK30-based blend represents an intermediate case: although its miscibility gap is still rather substantial, the binodal curve is to a large extent remote from the axes of the composition domain. The latter feature is especially true for the branch representing the MEH-PPV-rich phase. For this blend the model hence predicts formation of coexisting phases having a mixed composition rather than comprising only one constituent each. Indeed, as we have recently shown [1], for this blend trap dilution and concomitant rise in electron current does occur, despite large scale demixing. Concerning the polystyrene-based blends, the above given analysis shows that without performing any prior measurements or morphological investigation, the calculated ternary phase diagrams predict electron trap dilution to be likely when blending MEH-PPV with PS1 and not if PS35 is used as host material.

Before verifying this prediction with electrical measurements on actual thin film devices, we first present the morphological characterization of the spin-coated blend layers. To this end we chose a combination of atomic force microscopy (AFM) and confocal laser scanning microscopy (CLSM) as complementary techniques to reveal both the surface and bulk characteristics of the films. AFM guarantees a high lateral resolution but probing is limited to the top surface of the film. In contrast, CLSM, which visualizes regions rich

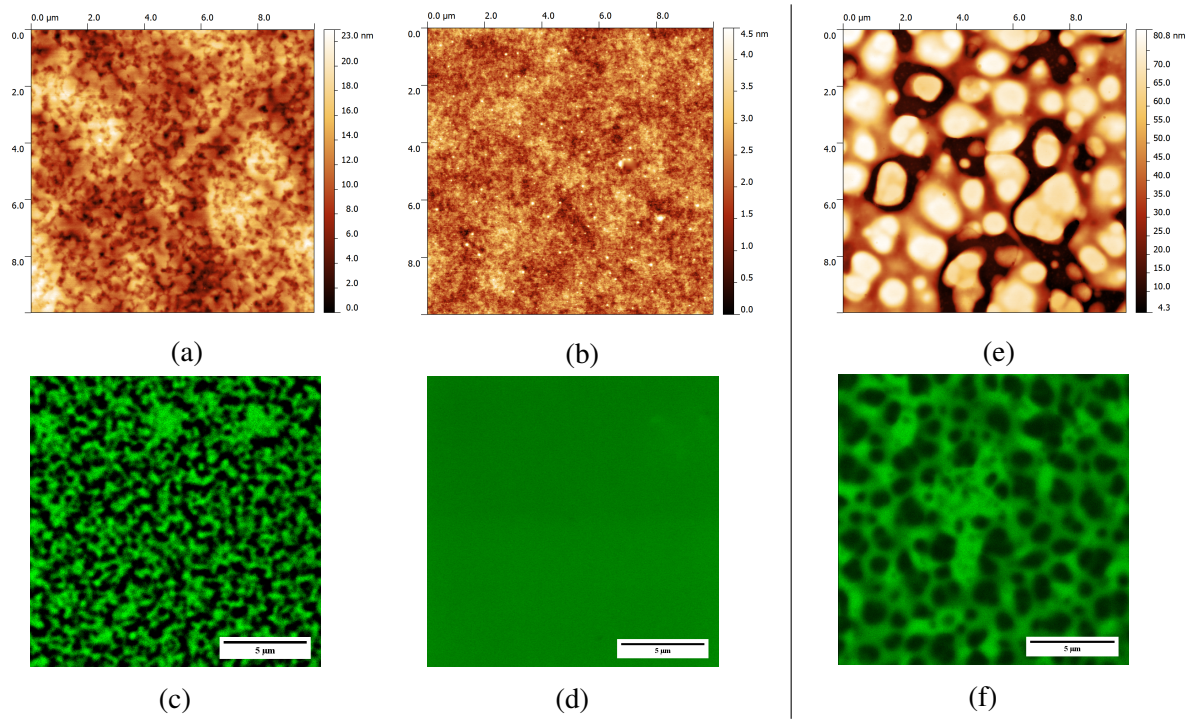

Fig. 3.3 AFM surface topography (top) and CLSM (bottom) images of thin films of the 1:3 MEH-PPV:polystyrene and 1:3 MEH-PPV:PVK blends, spin-coated from chlorobenzene using polystyrene with a weight-average molecular weight of $\overline{M}_{w,PS} = 35$ kg/mol ((a) and (c)), $\overline{M}_{w,PS} = 1.1$ kg/mol ((b) and (d)) and PVK with $\overline{M}_{w,PVK} = 30$ kg/mol ((e) and (f)). In the CLSM images the green regions represent enhanced photoluminescence and hence indicate the MEH-PPV-rich phase domains; the dark regions are rich in insulator.

in photoluminescent material (here: MEH-PPV) via local excitation with laser light, has a lower lateral resolution but provides for morphological information associated with the bulk of the layer. Figure 3.3 shows the AFM (topology) and CLSM images obtained for the PS-based blends (panels (a)–(d)). Again, for comparison we have included the images for the MEH-PPV:PVK30 blend (panels (e) and (f)). For reasons of space we limit ourselves to presenting the data corresponding to a 1:3 blend ratio.

Before expanding on structural details, comparison between the images corresponding to a high and low insulator molecular weight immediately reveals pronounced morphological differences. Whereas the MEH-PPV:PS35 and MEH-PPV:PVK30 blend films are rough and strongly corrugated (panels (a), (c), (e), (f)), the film based on MEH-PPV:PS1 (panels (b) and (d)) is featureless and smooth. In line with the predictions based on the ternary phase

diagrams, we explain this difference by macro-phase separation only to occur for the former blends and not for MEH-PPV:PS1.[3]

As mentioned in the introduction, the drop-like features characterizing the morphology of the MEH-PPV:PS35 and MEH-PPV:PVK30 films strongly suggest phase separation to occur via liquid–liquid demixing. Close inspection of corresponding AFM and CLSM images reveals that for both demixed blend films (i) the topologically elevated regions represent the non-photoluminescent, and hence dark, insulator-rich phase and (ii) that the surface topology matches the structure in the bulk. We further emphasize that the typical width of the phase domains significantly exceeds the film's average thickness ($\tilde{2}$00 nm), from which we conclude that both morphologies are effectively two-dimensional.

It is noted that for MEH-PPV:PS35 demixing results in a bicontinuous morphology, whereas for MEH-PPV:PVK30 a structure is obtained in which the insulator-rich phase is dispersed in a PPV-rich matrix. The fact that for a 1:3 blend ratio mass conservation alone would suggest the semiconductor-rich phase to be dispersed and the insulator to be continuous, *i.e.*, opposite to what is observed, indicates the presence of dynamic asymmetry during demixing. Expanding on this would go beyond the scope of this paper, but it has been shown that a difference in (instantaneous) elastic modulus between the two phases [60], *e.g.*, due to transient network formation or difference in glass transition temperature, can give rise to the observed morphological characteristics [75].

As shown above, the morphologies of the MEH-PPV:PS blend films are in good qualitative agreement with the predictions based on the calculated ternary phase diagrams. Nevertheless, the morphological analysis does not teach us whether the MEH-PPV:PS35 blend indeed demixes into phases that are too pure to allow for a reduction in the trap- and transport site density with concomitant rise in electron current. Conversely, although the above given analysis demonstrates large scale phase separation to be unlikely for MEH-PPV:PS1, it does not answer the question whether mixing of the two polymers is sufficiently intimate to achieve trap dilution.

In order to resolve these matters and to complete the validation of our predictions, we proceed with discussing electrical measurements on single charge carrier devices based on the above discussed MEH-PPV:insulator blends. Details on the architecture and fabrication of these devices are given in the Experimental section. Figure 3.4 presents the current densities of holes (lines) and electrons (symbols) as a function of voltage (V). As a reference, the single carrier JV-curves measured for pristine MEH-PPV (black) are included as well. As expected, the electron current density in pristine MEH-PPV is about three orders of

[3]Hypothetically, featureless AFM and CLSM images would also be obtained if phase separation were to occur exclusively in the vertical direction. However, as we shall see below, such stratified phase morphology can be ruled out based on the observed electrical characteristics of the blend.

magnitude lower than the hole current density due to the trap-limited nature of the former. Besides, the electron current exhibits a significant hysteresis due to permanent capture of electrons by deep trap states.

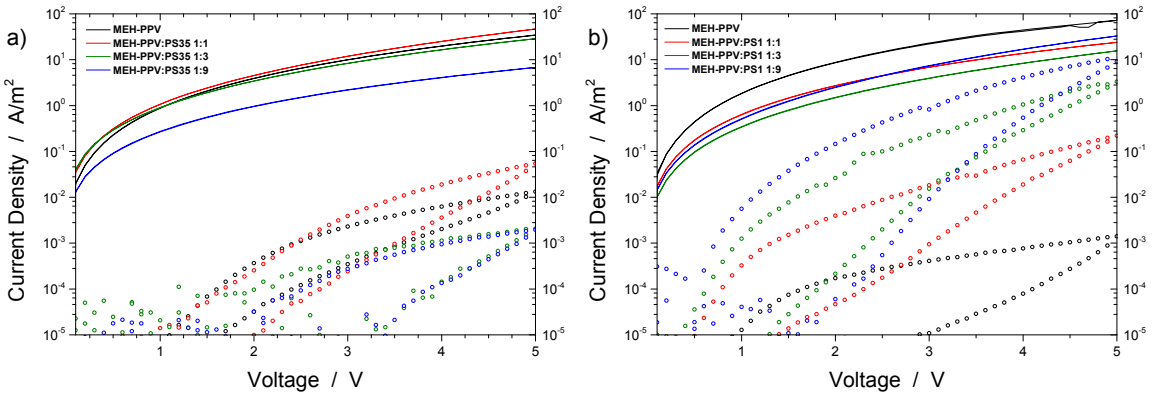

Fig. 3.4 Current density (J) of positive (lines) and negative (dots) charges plotted as a function of applied voltage (V), measured on single carrier devices based on (a) MEH-PPV:PS35 and (b) MEH-PPV:PS1. The colors represent different MEH-PPV:polystyrene weight ratios.

Figure 3.4 (a) shows that in contrast to what we observed earlier for PVK30, no rising trend in electron current is obtained when blending MEH-PPV with an increasing fraction of PS35. In case of the 1:3 and 1:9 blend ratios the electron current density even drops below that of the pure semiconductor. Hence, for MEH-PPV:PS35 a more or less opposite behavior is observed compared to MEH-PPV:PVK30, for which the electron current density consistently increases with the insulator content (see Figure 2 in [1]). The absence of a rise in electron current density with increasing polystyrene fraction shows that indeed no trap dilution occurs when blending MEH-PPV with 35 kg/mol polystyrene. This observation is in excellent agreement with the above given prediction that for this particular blend liquid–liquid demixing likely results in coexisting phases consisting of virtually pure semiconductor and insulator.

In contrast to what we observe for MEH-PPV:PS35 and in further agreement with our predictions, a consistent increase in electron current is obtained when blending MEH-PPV with the low molecular weight polystyrene sample PS1 (Figure 3.4 (b)). In case of the 1:9 blend ratio the electron current density approaches the hole current density even within an order of magnitude. The removal of the trap-limited nature of the electron current shows that mixing between MEH-PPV and PS1 is indeed sufficiently intimate to allow for spatial separation of transport- and trap sites within the semiconductor, without violating electrical percolation. These measurements demonstrate that electrically the MEH-PPV:PS1 blend

behaves very similar to the earlier studied MEH-PPV:PVK30 blend, despite the fact that the latter exhibits pronounced demixing whereas the former does not.

Figure 3.4 (b) shows that blending MEH-PPV with PS1 results in a balanced transport of positive and negative charges. To demonstrate that this is beneficial to the performance of the actual OLED, we plot the luminous efficiency of dual carrier devices (see Experimental section 3.2) as a function of voltage and blend ratio (Figure 3.5). Just as we observed before for the MEH-PPV:PVK30 blends and in line with theoretical predictions [40], the device based on the 1:9 blend of MEH-PPV and PS1 (blue curve) exhibits a roughly doubled efficiency compared to the one comprising pristine MEH-PPV. The inclination of the green and blue curves at voltages exceeding 3 V is consistent with charge recombination occurring closer to the anode due to the strongly increased electron current. As a result, at high voltages the efficiency reduces somewhat due to exciton quenching by the anode [4].

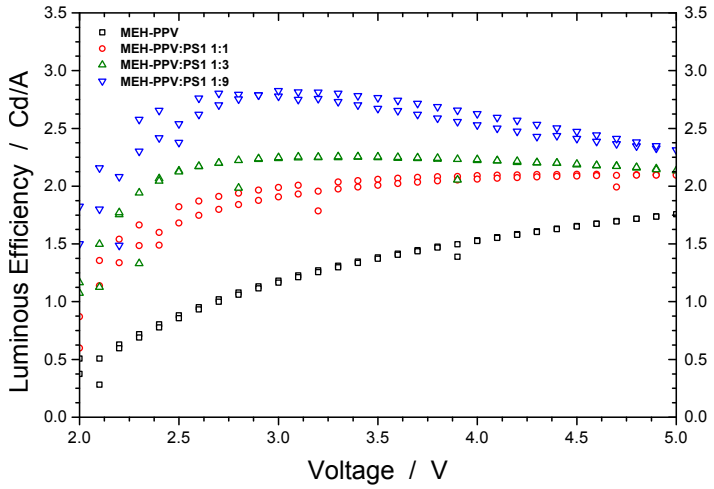

Fig. 3.5 Luminous efficiency plotted as a function of voltage (V) for OLED devices based on pristine MEH-PPV (black) and MEH-PPV:PS1 with a 1:1 (red), 1:3 (green) and 1:9 (blue) w/w blend ratio.

3.4 Conclusions

This work underlines the importance of the relation between the phase dynamics during solution-casting and thin-film device performance. We show that electron trapping in OLEDs based on disordered luminescent semiconductors such as MEH-PPV, can be eliminated by blending with low molecular weight polystyrene as insulating host. As this effect, which we

[4] We are aware of the fact that anode quenching can be avoided by making use of an electron blocking layer as described in [2], but this is outside the scope of this work.

have recently demonstrated using PVK as insulator, relies on spatial separation of transport and trap sites on a (near) monomeric or segmental level, mixing between semiconductor and host should be sufficiently intimate. The effect is not observed if high molecular weight polystyrene is used as host, in which case the blend shows pronounced liquid–liquid demixing during solution casting. We show that with this respect the calculated phase diagram provides for a means to predict whether the mixture of semiconductor, insulator and solvent is likely to exhibit the appropriate phase dynamics to ultimately give trap dilution and concomitant increase in OLED performance. Morphological and electrical characterization of MEH-PPV:insulator films not only validates our predictions, but also reveals that not the occurrence of demixing itself, but rather the (co)existence of (a) mixed phase(s) in the dry film determines whether electron trapping is reduced upon blending.

3.5 Appendix

The ternary phase diagrams in figure 3.2 were obtained via calculation of the mixing free energy, as defined by the Flory–Huggins model [18]. This model takes as input molecular size and interaction, which respectively determine the entropic and enthalpic contributions to the mixing free energy. Molecular size is represented by a relative degree of polymerization in terms of the number sites occupied per molecule on an imaginary molecular lattice. Interaction between monomers (sites) is captured by the dimensionless Flory–Huggins (binary) interaction parameters. Formulated per lattice site and given in units of kT, the mixing free energy is expressed as:

$$f = \frac{\phi_1}{N_1} ln\phi_1 + \frac{\phi_2}{N_2} ln\phi_2 + \frac{\phi_3}{N_3} ln\phi_3 + \chi_{12}\phi_1\phi_2 + \chi_{13}\phi_1\phi_3 \tag{3.1}$$

here, ϕ represents the volume fraction, N_i the relative degrees of polymerization and χ_{ij} the interaction parameters. Subscripts 1, 2 and 3 respectively refer to MEH-PPV, insulator (polystyrene or PVK) and solvent (chlorobenzene). The values for N_i were obtained by normalizing all molecular volumes by that of the solvent, *i.e.* $N_3 = 1$. Polymer–solvent and polymer–polymer interaction parameters were calculated using (Hildebrand) solubility parameters (δ) available from literature *via* equation 3.2 (solvent–solvent) and 3.3 (polymer–polymer).

$$\chi_{i3} = \frac{V_3}{RT} (\delta_3 - \delta_i)^2 + 0.34 \tag{3.2}$$

$$\chi_{12} = \frac{\sqrt{V_1 V_2}}{RT} (\delta_1 - \delta_2)^2 \tag{3.3}$$

Here, V_m ($m = 1, 2, 3$) denotes the monomeric molar volume of each species. The second term on the RHS of equation 3.2 represents an entropic correction [31], which is non-negligible when considering polymer–solvent interaction. It becomes negligibly small when the interaction between two polymers is considered [23, 46, 57]. Tables 1 and 2 collect all input parameter values, with literature references given where appropriate.

It should be realized that different authors have reported different values for the solubility parameter of polystyrene (see [17] for more discussion on this). We have adopted the one recently obtained by Emerson et al. [17]. This choice is supported by the fact that the

Table 3.1 Relative degree of polymerization, monomeric molar volume, and solubility parameter

Material	N	V_i $(\frac{\text{cm}^3}{\text{mol}})$	δ $(\text{MPa}^{\frac{1}{2}})$
MEH-PPV	3000	250.1 [3]	18.6 [15]
Polystyrene (35 $\frac{\text{kg}}{\text{mol}}$)	350	97.9 [3]	17.9 [17]
Polystyrene (1.1 $\frac{\text{kg}}{\text{mol}}$)	15	97.9 [3]	17.9 [17]
PVK (30 $\frac{\text{kg}}{\text{mol}}$)	225	154.9 [3]	19.0 [61]
Chlorobenzene	1	101 [3]	19.6 [25]

Table 3.2 Flory-Huggins interaction parameters

Material	MEH-PPV	Polystyrene	PVK	Chlorobenzene
MEH-PPV	$\chi_{11}=0$	$\chi_{12}=0.04$	$\chi_{12}=0.01$	$\chi_{13}=0.38$
Polystyrene	–	$\chi_{22}=0$	–	$\chi_{23}=0.47$
PVK	–	–	$\chi_{22}=0$	$\chi_{23}=0.35$
Chlorobenzene	–	–	–	$\chi_{33}=0$

resulting value for χ_{23} is consistent with the one reported earlier by Kubo and Ogino [39] ($\chi_{23}=0.454$, at $T=303$ K).

The ternary phase diagrams were calculated the usual way [18, 66]. The spinodal is obtained by applying the condition:

$$\det(\mathbf{H})=0 \tag{3.4}$$

$\mathbf{H}$ denoting the Hessian matrix: $\mathbf{H}=\partial_{\phi\phi}f$. Here, use is made of the incompressibility assumption: $\sum_{i=1}^{3}\phi_i=1$, so that: $\phi_3=1-\phi_1-\phi_2$. The binodal is obtained using a common tangent construction following an iterative procedure that converges to satisfy the following constraints for the exchange chemical potential and osmotic pressure of coexisting phases I and II:

$$\left.\frac{\partial f}{\partial\phi_m}\right|_{\phi=\phi_m^{\text{I}}}=\left.\frac{\partial f}{\partial\phi_m}\right|_{\phi_m=\phi_m^{\text{II}}},m=1,2 \tag{3.5}$$

$$f^{\text{II}}=f^{\text{I}}+\sum_{m=1}^{2}(\phi_m^{\text{II}}-\phi_m^{\text{I}})\left.\frac{\partial f}{\partial\phi_m}\right|_{\phi=\phi_m^{\text{I}}} \tag{3.6}$$

This exercise "automatically" gives the tie-lines. The critical point follows from condition 3.5, together with: $\det(\mathbf{M}) = 0$, with $\mathbf{M}$ the matrix resulting from replacing any of the rows of $\mathbf{H}$ by the derivatives of $\det(\mathbf{M}) = 0$.

Chapter 4

Controlling compositional changes in BEH-PPV:PS Blends

This chapter is in preparation for publication with contributions from Kunz, A., Michels, J.J. and Blom, P.W.M.. Part of this chapter was published in 2020 as:
Ribeiro, A. H., Fakih A., van der Zee, B., Veith, L., Glaser, G., Kunz, A., Landfester, K., Blom, P. W. M., and Michels, J. J. (2020). Green and stable processing of organic light-emitting diodes from aqueous nanodispersions. *J. Mater. Chem. C*, 8:6528–6535.

4.1 Introduction

In the previous chapters a discussion on reduction of electronic trap states within MEH-PPV based polymer blends was demonstrated. Large band gap semiconductors, *i.e.* PVK, or insulators such as polystyrene can be used to effectively eliminate the negative effect of electron trap states within the band gap of MEH-PPV, when the latter is diluted sufficiently in a polymer blend with one of the first components. An important observation that was made is that not the occurrence of demixing, but rather the existence of mixed phases determines whether electron trapping is reduced upon blending.

It is of high interest to study this so called *dilution effect* with other semi-conducting polymers to provide evidence for the generality of this concept. Here poly[2,5-bis(2-ethylhexyloxy)-1,4-phenylene vinylene] (BEH-PPV), a PPV derivative with symmetric ethylhexyloxy substitution pattern of the aromatic ring in the backbone, is used and blended with the insulator polystyrene with an average molecular weight of $\overline{M}_{w,PS} = 1.1$ kg/mol. BEH-PPV compared to MEH-PPV has a higher charge carrier mobility due to lower energetic on-chain disorder originating from the symmetrically substituted conjugated backbone

[49]. So far, high charge carrier mobility for BEH-PPV could only be demonstrated for holes [48]. Electron mobility in contrast, is assumed to be as high as hole mobility, but the realization of an electron only device from BEH-PPV with equivalent *JV* characteristics could never be demonstrated empirically due to presence of energetic trap states within the energetic gap between HOMO and LUMO. For the similar polymer MEH-PPV, Zhang et al. demonstrated equal electron and hole mobility via n-doping with decamethylcobaltocene [84]. With the concept of diluting the semi-conducting polymer in an insulating host polymer (we will use the term insulating polymer equivalent to large band gap polymer) a method was established to get rid of the negative effect of trap states. PLED devices made from a MEH-PPV:PS with superior device performance and equilibrated *JV* characteristics for both HO and EO devices were demonstrated in the previous chapter and in [41]. The same concept is now transfered to a blend of BEH-PPV and PS to investigate, whether similar observations can be made. PLED devices fabricated from a BEH-PPV:PS blend can benefit from lower operation voltages due to higher charge carrier mobility, compared to MEH-PPV based devices and are therefore of practical interest to improve device performance.

Nevertheless, each different material combination in a blend gives rise to different phase dynamics and changing morphology of the blend system as a function of preparation history, solvents used and additional post treatment. For instance, surface-directed spinodal decomposition may occur due to a difference in surface energy between the blend components [33] in which one of the components is attracted by either the interface with air or the underlying substrate. At equilibrium condition in such a system a bilayer structure is formed. Under practical conditions fast evaporation rates of solvents in solution processed thin films inhibit the formation of equilibrated structures and as a result intermediate structures are formed. Compositional changes of the blend will have a direct effect on the electrical properties of the blend system in a device stack and should be therefore controlled properly.

In this study we observed unexpected hole injection issues by poly(3,4-ethylenedioxy-thiophene)poly(styrenesulfonate) (PEDOT:PSS) into BEH-PPV:PS blends with various PS fractions ranging from 0 to 90 wt%, when building hole only devices. Initial measurements of the surface topology (see figure 4.3) gave no hint on lateral phase separation of the blend components. Instead, we observed an overly increased fraction of highly insulating PS at the PEDOT:PSS-blend interface in thin films spin cast from chlorobenzene solution that prevents injection of holes from PEDOT:PSS into the blend. Dynamic time of flight secondary ion mass spectrometry (ToF-SIMS) is used to identify the vertical composition of the layers and blend components. The compositional change in the vertical direction is determined by correlation of individual mass fragments that unambiguously identify certain blend components and the underlying layer of PEDOT:PSS. PS is preferentially attracted

to the interface with PEDOT:PSS, while the fraction of BEH-PPV is higher at the air-blend interface. It is naturally to think that the surface on which the blend is spin cast directs the composition of the blend and influences the final film morphology. By changing the surface properties of PEDOT:PSS via blending it with perfluorooctane sulfonic acid (FOS) in excess, we avoid preferential accumulation of PS at the interface to PEDOT:PSS. As a result, we are able to demonstrate blend based hole only devices with equilibrated charge injection properties for BEH-PPV:PS 1:9 blends as previously shown for the MEH-PPV:PS system. In effect, we show that the concept of reducing charge carrier trapping by diluting a semiconducting polymer with an insulator type polymer is transferable to other polymer systems and not only limited to MEH-PPV:PS.

4.2 Experimental

Poly[2,5-bis(2-ethylhexyloxy)-1,4-phenylene vinylene] (BEH-PPV) was synthesized in house via the Gilch route [21]. The number average molecular weight of BEH-PPV was measured with a gel permeation chromatography setup against polystyrene standards and resulted in $\overline{M}_{n,BEH} = 521$ kg/mol and a polydispersity index of $D = 3.53$. Polystyrene was synthesized in house via anionic polymerization of styrene. The resulting weight average molecular weight is $\overline{M}_{w,PS} = 1.1$ kg/mol with a narrow polydispersity of $D = 1.15$.

Thin films of polymers and their blends were produced by spin casting from chlorobenzene solution under nitrogen protected glove box atmosphere. Concentrations were set to result in film thicknesses in the range between 100 and 200 nm after drying. The glass substrate cleaning procedure followed a standardized protocol of cleaning in neutralized soap, rinsing in de-ionized water and consecutive ultrasonic bath cleaning in acetone, and isopropanol- each step for 10 minutes. Before further application, UV-Ozone activation was performed for 20 minutes in order to achieve better wettability and residual organic compound removal.

If not stated different in further notice, hole only device fabrication included spin casting poly(3,4-ethylenedioxythiophene)polystyrene sulfonate (PEDOT:PSS) (Heraeus Clevios 4083) dispersion on activated ITO substrates (precoated and prepatterned) with a final PEDOT:PSS film thickness of approximately 55 nm. The film thickness was acquired after dry- and bake out in a 140° C temperature controlled oven. Glass substrates for electron only devices were coated with partially oxidized aluminum in a vacuum coater via thermal deposition of the metal and patterning using a shadow mask. A thin film of BEH-PPV or BEH-PPV:PS blend with a thickness between 100 and 200 nm was spin cast onto the

ITO/PEDOT:PSS (for PLED or HO devices) or aluminum coated (EO devices) substrates in a nitrogen purged glove box.

Without breaking the inert atmosphere, the substrates were transfered into the vacuum coater in order to deposit the top electrode. For HO devices 10 nm of MoO_3 and additional 100 nm of aluminum were deposited through a shadow mask on top of the polymer(-blend) layer. For EO devices 5 nm of barium were deposited and capped with a 100 nm aluminum layer likewise.

The work function of materials was measured with a Kelvin-Probe setup using a vibrating gold tip that was calibrated against a freshly produced highly oriented pyrolytic graphite surface (HOPG). Details of the measurement method are described more thoroughly in the work of Hansen and Hansen [26].

ToF-SIMS measurements were performed with a TOF.SIMS 5 by IONTOF. A schematic representation of the setup is shown in figure 4.1. A primary ion beam is generated in a so called *Liquid Metal Ion Gun*. The beam is accelerated and focused in a focusing and raster optic onto the target surface. Bombardment of primary ions causes emission of charged surface target molecules and atoms that are focused in a transport optics systems as secondary ion beam. The secondary ions are separated in a time of flight detector by their mass to charge ratio $\frac{m}{z}$ and recorded as mass spectrogram. Additional surface ablation (sputtering) with another primary ion source enables the technique to dynamically scan the chemical composition of the target substrate as a function of sputter depth. In this work primary ion bombardment and analysis was done using Bi_3^+ ions at an ion energy of 30 keV and a current of 0.25 pA. The analysis area was chosen to be 200 x 200 μm^2. Ar_{1200}^+ clusters with an ion energy of 5 keV were used to sputter an area of 400 x 400 μm^2 with a sputter current of 1.52 nA after each analysis step in order to study the chemical composition as a function of sputter depth.

4.3 Results & Discussion

In figure 4.2 (a) the electron only *JV*-characteristics for BEH-PPV:PS blends with varying fractions of polystyrene are shown. The pristine BEH-PPV electron only device (black line) shows the typical trap limited and therefore low current density as a function of applied voltage. By increasing the fraction of low molecular weight polystyrene the *JV*-characteristics drastically improve. With higher fractions of polystyrene going from 50% (red line) over 75% (green line) to 90% (blue line) by weight the current density increases by one, two and three orders of magnitude, respectively, owing to the already discussed effective elimination of the trap limited nature of charge transport characteristics when diluting the semi-conducting

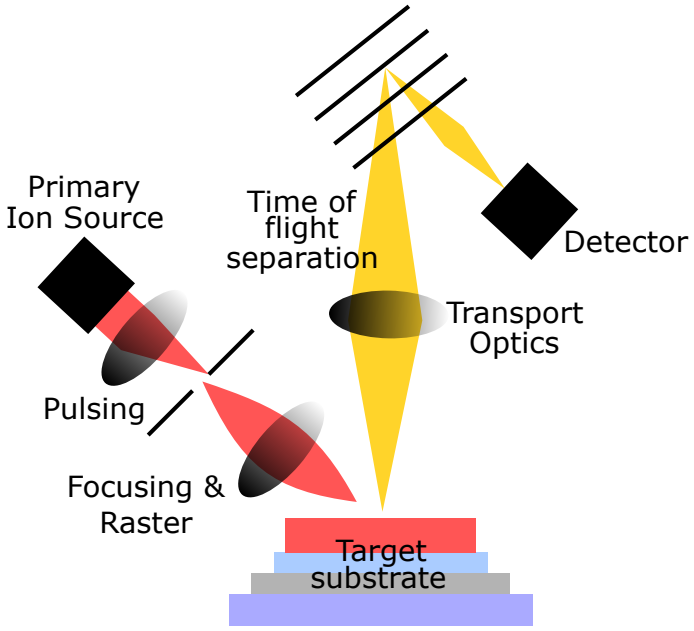

Fig. 4.1 A schematic representation of the ToF-SIMS working principle is shown. The primary ion beam (red) is generated and focused in the pulsing and focus optics. Bombardment of a target surface with primary ions generates emitted secondary ions (yellow) that are transported through a time of flight separator and detected by their mass to charge ratio $\frac{m}{z}$.

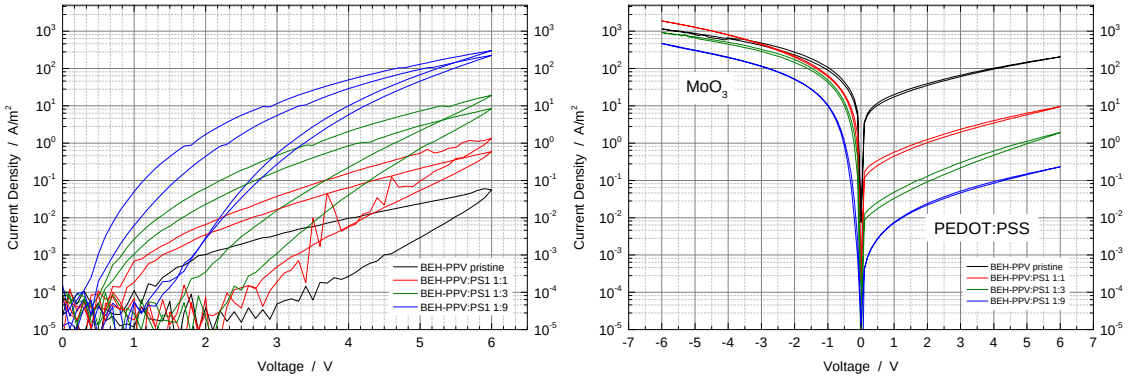

(a) (b)

Fig. 4.2 Current density J as a function of applied voltage V for (a) electron only devices and (b) hole only devices with varying polystyrene fraction in the BEH-PPV:PS1 blend. Device thicknesses were kept constant at around $L \approx 150$ nm.

polymer with an insulating host material. In contrast to that, we have shown in previous chapters that the trap free hole transport does not suffer for the blend systems MEH-PPV:PVK and MEH-PPV:PS, or even improves by dilution in an insulating host (see chapters 2 and 3).

In figure 4.2 (b) a strongly differing picture is shown. The figure shows the *JV*-characteristics of BEH-PPV:PS blend based hole only devices with varying polystyrene fraction following the same weight ratios as mentioned for the electron only devices. The current voltage characteristics of the pristine BEH-PPV hole only device are taken as a reference (shown as black solid line in figure 4.2 (b)). Current injection in the positive voltage range is established via the PEDOT:PSS bottom contact. Current injection in the negative voltage range is established via the MoO_3 top contact. Asymmetry for the current density between the positive and negative voltage range is observed. The current density of the positive voltage range shows lower values, which is typically seen for injection limited contacts when work function of the injecting contact and the HOMO of the material are energetically not aligned, resulting in a non-ohmic contact. This trend continues for the blends with increased polystyrene fraction, showing that injection of positive charge carriers from the PEDOT:PSS contact gets more difficult with higher polystyrene fraction. The current density values of the MoO_3 contact on the other hand show no significant drop as seen for the PEDOT:PSS contact. We hypothesize two possible mechanisms for the observed discrepancy between the current density values. First, as already the reference device shows slight asymmetry, we assume to have non-ohmic charge injection at the PEDOT:PSS contact, although HOMO level and work function of the materials are in matching conditions. This possibility will be discussed in section 4.3.1.

A second hypothesis is possible occurrence of vertical phase separation (stratification) of polystyrene and PPV. It is known [33], that even a miscible blend segregates at an interface due to preferential interaction. This preferential interaction causes the concentration ratio at the surface to be different from the bulk. In this study we can rule out the occurrence of lateral phase separation, as we have measured the surface topology in an AFM analysis shown in figure 4.3 for a 1:0, 1:1, 1:3 and 1:9 blend of BEH-PPV:PS1. All three blend based topologies (figures 4.3 (b) to (d)) show a smooth surface in the same manner as the reference film made from pristine BEH-PPV (figure 4.3 (a)). No recognizable structure is formed as typically seen for phase separated polymer blends [1]. The only possible phase segregation mechanism is then a stratified structure or incomplete stratification with a gradient in composition within the thin film. Our second hypothesis is therefore an over-proportional accumulation of insulating material at the PEDOT:PSS contact due to preferred interaction of polystyrene and PEDOT:PSS. Accumulation of insulating material at the contact can cause percolation issues

[1] One example for lateral phase separation can be found in figure 3.3 in chapter 3.3

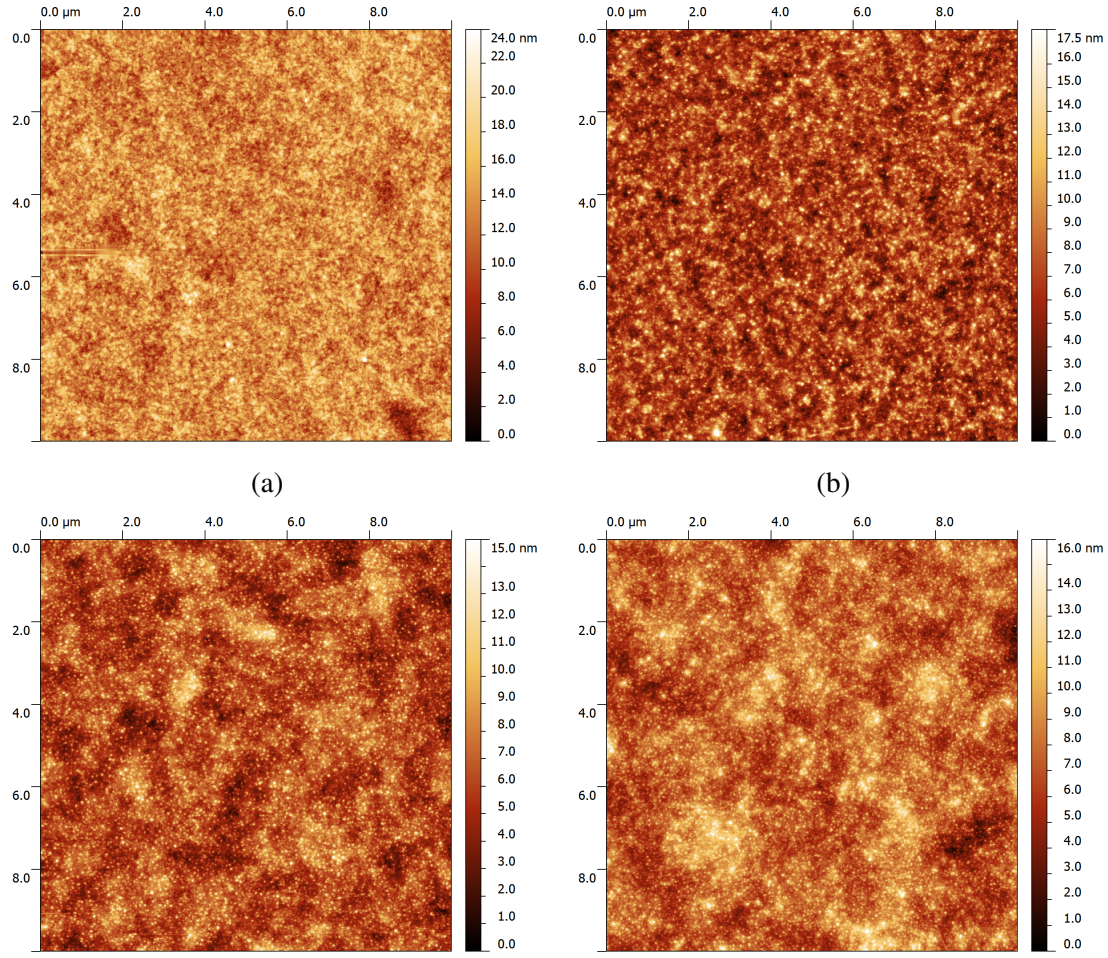

Fig. 4.3 AFM topological images of (a) BEH-PPV, (b) BEH-PPV:PS1 1:1, (c) BEH-PPV:PS1 1:3, (d) BEH-PPV:PS1 1:9. All films were cast from chlorobenzene on top of a PEDOT:PSS film.

in such a way that charge carriers cannot be transferred to the semi-conducting polymer and charge carrier density is drastically reduced forming a physical barrier for hole injection. Further discussion on this hypothesis will be conducted in section 4.3.2.

4.3.1 Work function modification of PEDOT:PSS injection layer by solvents

In this subsection we will discuss how the work function of PEDOT:PSS is affected, when different steps of fabrication of the thin film are performed, such as, drying, activation in the UV/Ozone oven or solvent application. As described in the experimental section 4.2, PEDOT:PSS is spin cast on top of activated ITO. In order to obtain a broader picture, we include the work function analysis of ITO before we evaluate the work function of PEDOT:PSS. Glass substrates covered with ITO electrodes were cleaned as described in the experimental section 4.2. Before subsequent activation in an UV/Ozone oven, the work function of ITO was determined to be as high as $W_{ITO,cleaned} = 4.49$ eV, measured with a Kelvin probe setup according to Hansen and Hansen [26] against highly oriented pyrolytic graphite (HOPG) under ambient conditions. HOPG provides for an extremely stable work function under ambient conditions, *i.e.* a value of $W_{HOPG} = 4.475 \pm 0.005$ eV. Figure 4.4 shows the work function change of ITO as a function of time after the standard cleaning procedure and subsequent activation in an UV/Ozone oven for 15 min. Compared to the non-activated ITO the work function of activated ITO was increased to a value of $W_{ITO,activated} = 5.14$ eV. Within the course of a measurement duration of 40 min W_{ITO} dropped to a value below 5.06 eV. The obtained measurements are in good agreement with previously reported measurements done by Schlaf et al. [67]. Consequently, in order to improve hole injection by the ITO anode to establish ohmic contacts to consecutively spin coated organic semi-conducting layers quick fabrication is advisable and common practice.

Now that we have investigated the properties of the ITO contact, we will have a closer look on the PEDOT:PSS layer that is spin cast on top of the activated ITO. PEDOT:PSS brings further improvements in hole injection as it acts as a buffer and hole transport layer. PEDOT:PSS according to data sheet specification has a work function of 5.1 ± 0.1 eV (Clevios® P VP.AL 4083). PEDOT:PSS has a stable work function as compared to ITO, it flattens surface irregularities of ITO and wetting properties for polymeric solutions based on organic solvents are typically better. In standard device preparation, several organic solvents are used to deposit subsequent layers. In this work we mainly use chlorobenzene because of its aromatic nature and good dissolving properties for most functional polymers, like BEH-PPV or MEH-PPV. Anyway, we will draw the investigation slightly broader and

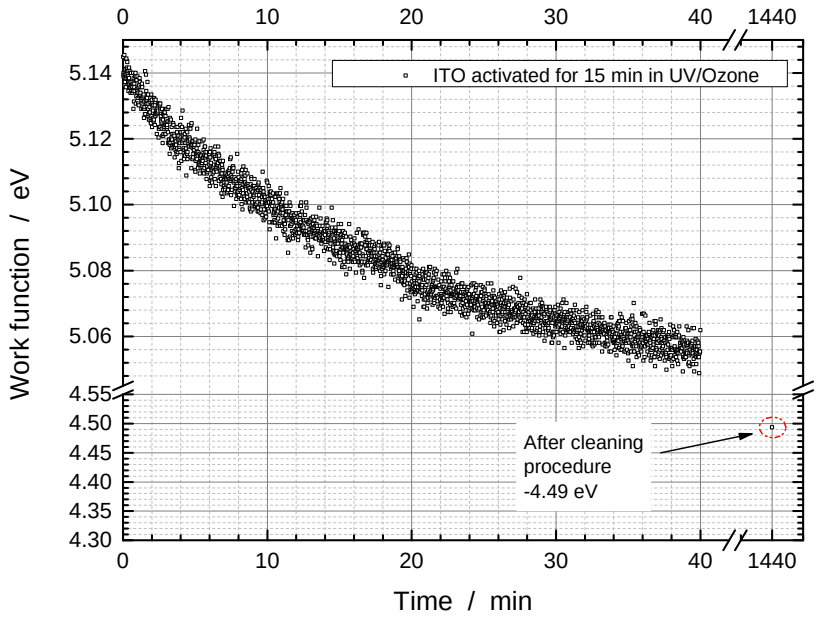

Fig. 4.4 Work function of ITO as a function of time after cleaning and subsequent treatment in an UV/Ozone oven for 15 minutes.

analyze the change of work function of PEDOT:PSS when exposing it to multiple organic solvents, *i.e.* chloroform, chlorobenzene, toluene. In figure 4.5 the measured work function

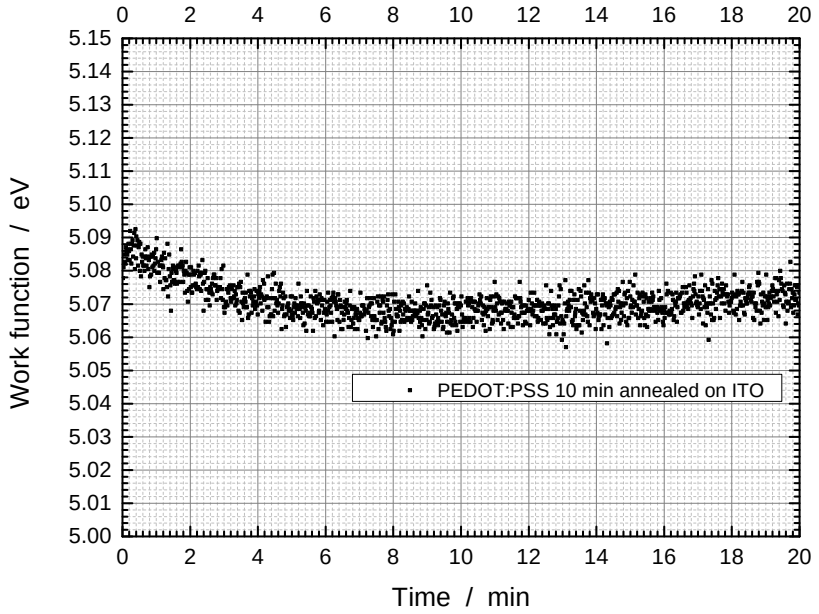

Fig. 4.5 Work function of PEDOT:PSS as a function of time after deposition on UV/Ozone activated ITO and subsequent annealing for 10 minutes at 140° C.

of PEDOT:PSS is shown. The measured work function of this sample will be taken as

reference. The sample is prepared according to the cleaning procedure described in the experimental section 4.2, which is similarly applied for device fabrication. The PEDOT:PSS layer was deposited on UV/Ozone activated ITO and subsequently annealed at 140° C for 10 minutes. Measurements were done under ambient conditions. We observe an initial value for the work function around 5.09 eV that drops within the first 4 minutes to a value of 5.07 eV. After that, it stays almost constant until the end of the measurement after 20 minutes. In the beginning of the Results & Discussion section 4.3 we hypothesized a change in surface functionalization of the PEDOT:PSS induced by the application of organic solvents, such

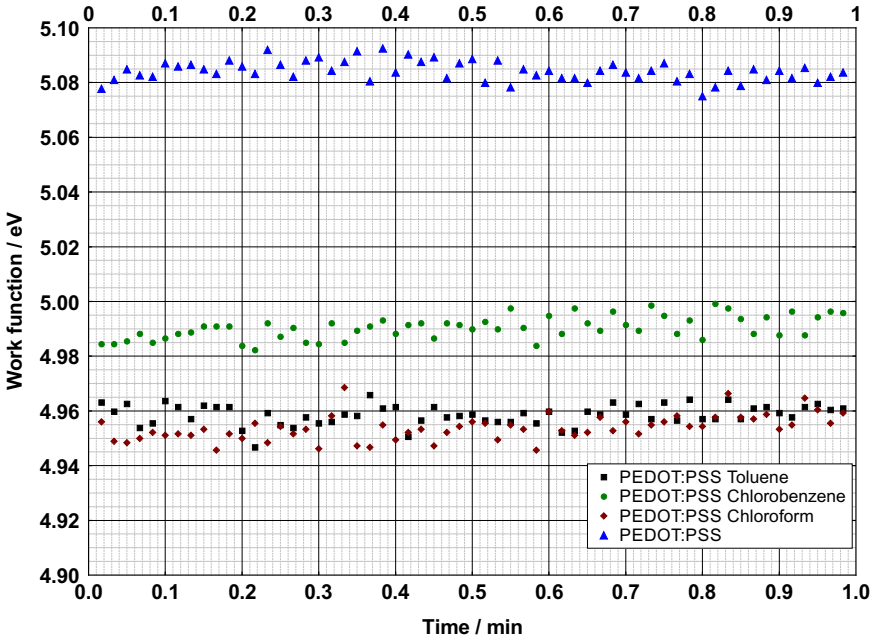

Fig. 4.6 Change in work function of PEDOT:PSS(blue) after spin coating a few drops of chlorobenzene (green), chloroform(red) and toluene(black), respectively.

as chloroform, chlorobenzene and toluene. In order to investigate changes of the work function of PEDOT:PSS we covered the surface of annealed PEDOT:PSS with a few drops of chloroform, chlorobenzene and toluene for 10 seconds, respectively. At the end of solvent application the samples were dried by spinning the samples at 1000 rpm for 90 seconds in a closed spin coater. The work function of treated PEDOT:PSS was measured immediately after the drying process. The resulting values for the work function are shown in figure 4.6 as a function of measurement time. Generally compared to the acquired reference values in figure 4.5, lower values for the work function of all three samples are observed. Chloroform treated PEDOT:PSS shows a work function at a value between $4.95 - 4.96$ eV. Likewise, toluene treated samples show work function values around 4.96 eV.

Chlorobenzene treated PEDOT:PSS samples show slightly higher work function values between $4.98 - 5.00$ eV. Considering the latter values to be closer to the reference value of PEDOT:PSS and also to the HOMO level of BEH-PPV, chlorobenzene based solutions should be favored over the other two solvents, when spin casting BEH-PPV and blend solutions with polystyrene onto PEDOT:PSS. Nonetheless, none of the observed drops in work function of solvent treated PEDOT:PSS can cause massive charge injection issues into the HOMO states of BEH-PPV and is not a sufficient explanation for the huge drop in hole current density as seen in figure 4.2 (b) for blend based HO-devices (red, green and blue lines). Another explanation has to be found to explain the detrimental loss in charge transport capability.

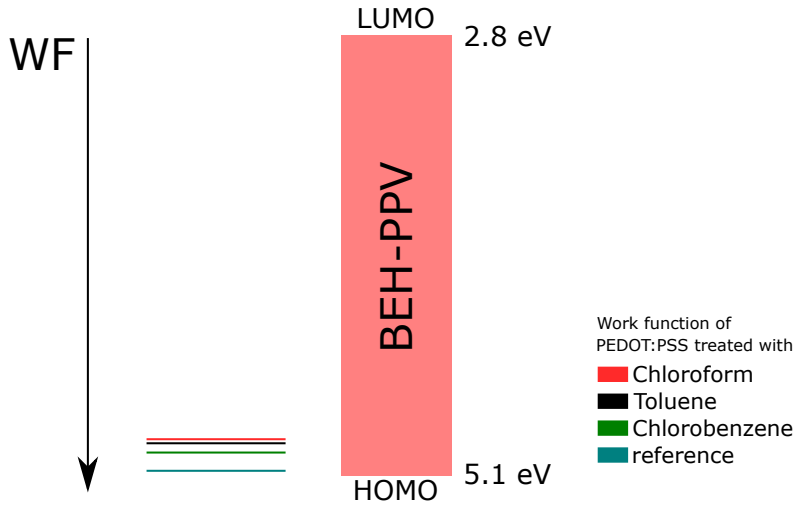

Fig. 4.7 Schematic representation of changed PEDOT:PSS work functions in relation to BEH-PPV band gap.

4.3.2 Depth profiling with ToF-SIMS

In section 4.3.1 we analyzed the work function change of PEDOT:PSS upon solvent application. The work function of PEDOT:PSS was barely affected by treatment with organic solvents, such as chloroform, toluene or chlorobenzene, which in turn means it cannot provide for an explanation for the drastic decrease in hole injection probability. To provide for an alternative hypothesis, we state that during the course of spin coating and solvent evaporation the BEH-PPV:PS1 blend solution experiences incomplete vertical stratification of the blend components in such a way that the polystyrene fraction is higher at the bottom of the blend film at the interface to the PEDOT:PSS layer, the hole injection contact. Kinetically, separation of the components will get immobilized due to the loss of solvent molecules during the drying process. As already discussed in the introduction of this chapter, an accumulation

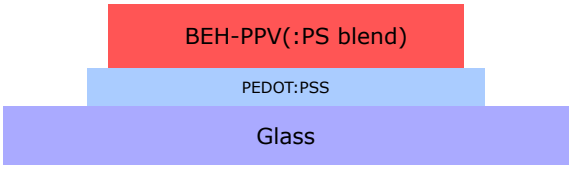

Fig. 4.8 Schematic representation of the polymer (blend) stack used for ToF-SIMS analysis.

of insulating polystyrene will cause a loss of charge density during injection. Percolation pathways for charges in a highly insulating layer are absent.

It is not possible to investigate the chemical composition of the bulk material with the help of an AFM, as it is limited to only acquire topological information of the surface. Instead, we perform mass spectrometric depth analysis with the help of ToF-SIMS (further information given in experimental section 4.2) and in figure 4.1. ToF-SIMS as used in this work is a dynamical chemical depth profiling tool. Primary ions of Bi_3^+ are generated, focused and bombarded onto a solid surface resulting in emission of secondary ions which consist of fragmented components of the surface molecules. The emitted secondary ions are analyzed by their mass to charge ratio $\frac{m}{z}$ in a time-of-flight detector. After analyzing a particular area of interest, a subsequent sputtering step removes a larger area in order to generate a fresh surface for analysis deeper in the bulk. Alternating the analysis step with the sputter step allows the technique to create a chemical depth profile of a specimen.

While the surface of a polymer film is bombarded with primary ions, the molecules of the surface get fragmented to charged smaller molecule units or even atoms, which then are detected as secondary ions in the time of flight detector. Proper interpretation of the mass spectrograms has to be done. As polymers consist of repeating units of a monomer, the most intuitive $\frac{m}{z}$ to look for is a single charged monomeric unit. Additionally, $\frac{m}{z}$ of ionized dimers or fragments of side chains of a polymer can be identified. Ideally, each polymer or smaller organic molecule will have its own *library* of mass to charge patterns in the spectrogram. In order to study additionally the chemical composition as a function of depth, a larger area on the surface is ablated by Argon cluster ion (Ar_{1200}^+) sputtering after each analysis step. The rate of ablation of surface molecules can be measured, where the specific sputter rate of a BEH-PPV layer might be very different to the sputter rate of a PEDOT:PSS layer. Also, the sputter time can be translated into a depth information, when the thicknesses of all layers are known or separately determined by measuring the sputter rates individually. After a cycle of ablation a new surface is created and analyzed with the primary ion bombardment. This procedure is repeated until the bulk and all layers are penetrated. As a result, a chemical $\frac{m}{z}$ information as a function of sputter time is obtained.

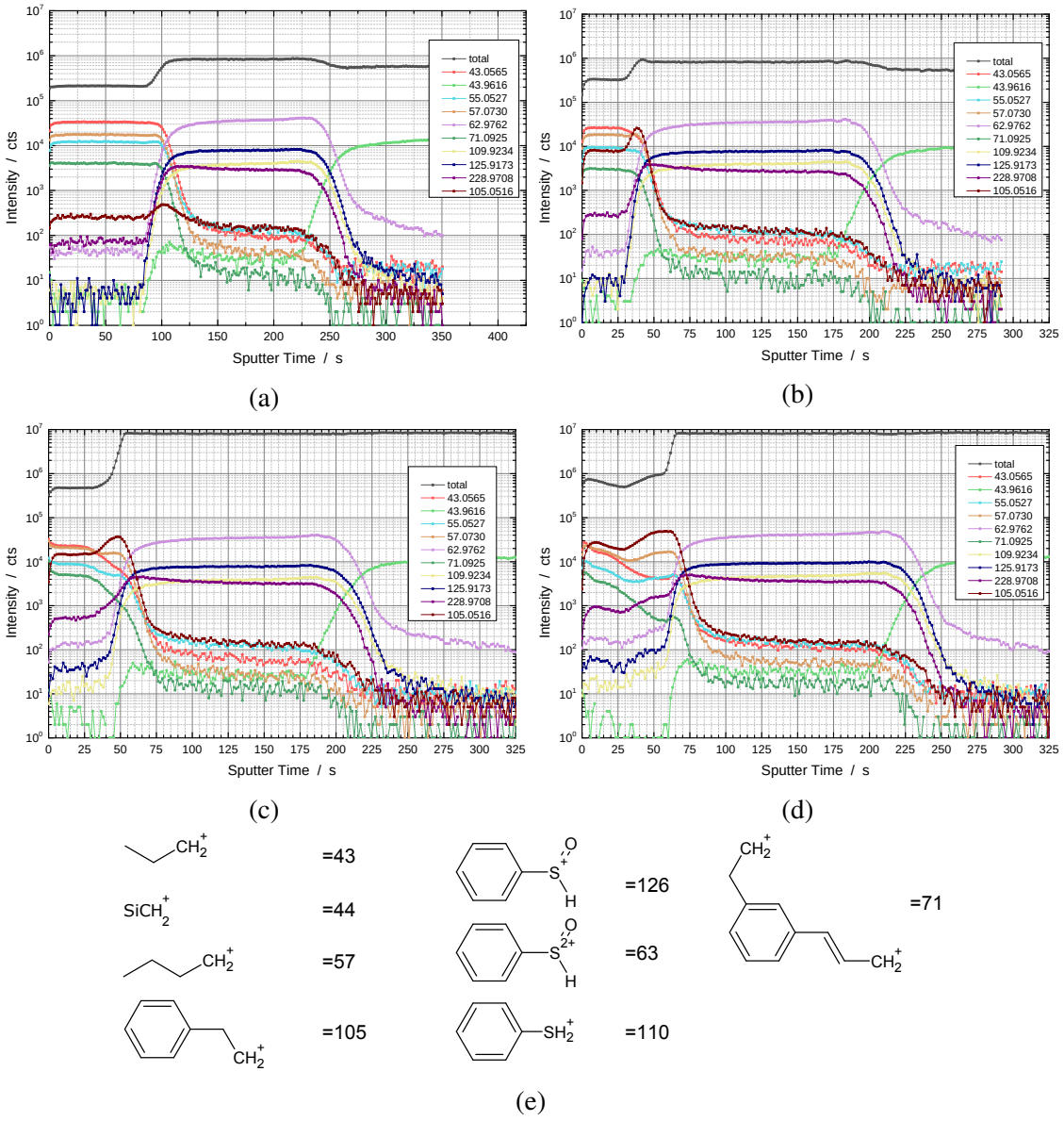

Fig. 4.9 TOF-SIMS depth profiles (detected ions as a function of sputter time) of BEH-PPV and BEH-PPV:PS blend layers on PEDOT:PSS measured in positive polarity. Numbers given in the legend of figure (a) to (d) denote the mass to charge ratios that were detected during ToF-SIMS analysis. Figure (e) shows possible chemical fragments corresponding to the mass to charge ratios given in figures (a) to (d).

We performed the aforementioned depth analysis with ToF-SIMS looking at thin films of BEH-PPV and BEH-PPV:PS1 blends. A schematic representation of the stack used for analysis is shown in figure 4.8. The counter electrodes that are used in HO devices, EO devices or PLEDs are not present.

In figure 4.9 (a) to (d) ToF-SIMS depth profiles of all four ratios (1:0, 1:1, 1:3, 1:9) of BEH-PPV:PS1 blend films on PEDOT:PSS are shown. The black signal denotes the total ion count. The colored signals denote each a different $\frac{m}{z}$. We have found that each consecutive polymer layer has different $\frac{m}{z}$ patterns. Also, we round all mass to charge ratios to integers for simpler reading. The initial layer, that is the BEH-PPV:PS1 layer always contains the $\frac{m}{z}$ 43, 55, 57 and 71. The second layer (PEDOT:PSS) has increased signals at 63, 126, 110 and 229 $\frac{m}{z}$. The last layer is the glass substrate which easily is described by a silicon compound at a $\frac{m}{z}$ of 44. A suggestion for the chemical species of the $\frac{m}{z}$ values is done in figure 4.9 (e). The chemical assignments come with a significant uncertainty as it is a subjective interpretation to possible fragments. The most prominent signals for each chemical compound are found to be 43 for BEH-PPV, a possible side chain fragment of BEH-PPV, 63 for PEDOT:PSS, which is a doubly charged fragment of the styrene sulfonic acid moiety, 44 ($SiCH_2^+$) for the glass substrate and very prominently 105 for polystyrene, which is exactly a positively charged styrene unit. No logical chemical assignments could be found for the $\frac{m}{z}$ values of 55 and 229. The profiles in figure 4.9 (a) allow us to determine the sputter time until different layers and interfaces are reached. For instance, the stable $\frac{m}{z} = 43$ signal rapidly decreases after ≈ 105 sec and the $\frac{m}{z} = 63$ signal increases at this time spot to reach an almost stable plateau until a sputter time of ≈ 230 sec is reached. In parallel we observe an increased total ion signal. Concurrently to the decrease of the $\frac{m}{z} = 63$ signal, the $\frac{m}{z} = 44$ signal increases. By definition in ToF-SIMS, an interface is identified, when the dominating $\frac{m}{z}$ reaches half the initial plateau value counts. In total, we can identify two interfaces, one at a sputter time of 105 sec as the BEH-PPV/PEDOT:PSS interface and the second at a sputter time of 230 sec as the PEDOT:PSS/Glass interface. We measured the thickness of each layer to identify the individual sputter rates. Values are listed in table 4.1.

A significantly high signal for a $\frac{m}{z}$ value of 105, the positively charged styrene unit, is only found in figures 4.9 (b) to (d), which is logical as the reference device analyzed and shown in figure 4.9 (a) does not contain any polystyrene. For the blend based devices depth profiles show an increased $\frac{m}{z} = 105$ signal in the first layer and a highly elevated signal at the transition to the PEDOT:PSS interface. At this point a calculation of the BEH-PPV to PS1 ratio across the blend layer can be done. In order to do so, we compare the integral of the BEH-PPV signal (in this case the $\frac{m}{z} = 43$ signal) with the integral of the PS1 signal

Table 4.1 Layer thicknesses, sputter time and calculated sputter rates for BEH-PPV, BEH-PPV:PS1 blend, PS and PEDOT:PSS films

Layer	Thickness / nm	Sputter time / sec	Sputter rate / $\frac{\text{nm}}{\text{sec}}$
BEH-PPV	84	105	0.800
PEDOT:PSS	56	145	0.386
BEH-PPV:PS1 1:1	77	43	1.790
BEH-PPV:PS1 1:3	132	57	2.315
BEH-PPV:PS1 1:9	184	69	2.666
PS1 (estim., see fig 4.11 (a))	–	–	2.875

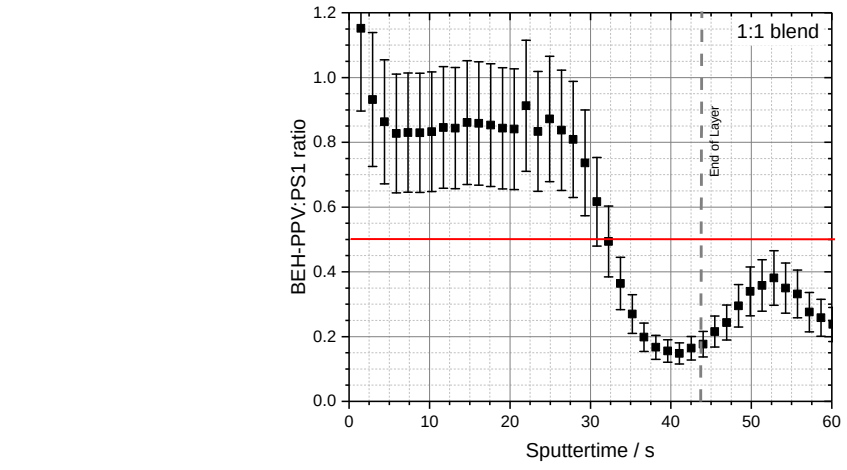

(a)

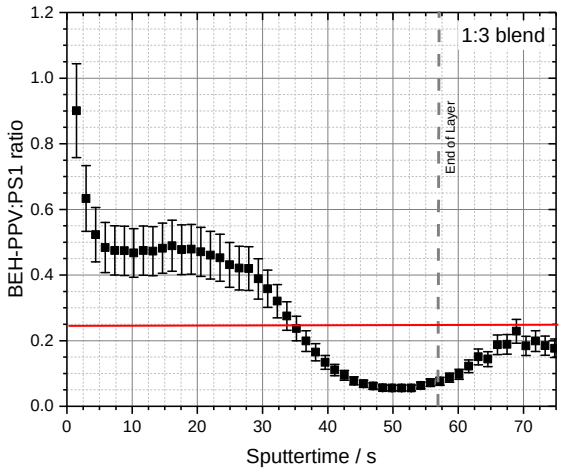

(b)

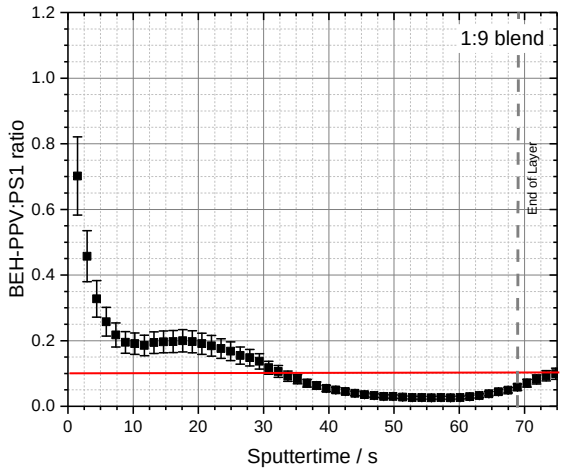

(c)

Fig. 4.10 Calculated composition as a function of sputter time for the blend layers. (a) BEH-PPV:PS1 1:1, (b) BEH-PPV:PS1 1:3 (c) BEH-PPV:PS1 1:9 . The red line in each graph denotes the mean weight ratio of the polymer blend and the dashed grey line denotes the end of the blend layer.

Table 4.2 Calculation of the relative ion sensitivity

Layer	Area $\frac{m}{z} = 43$ / cts · s	Area $\frac{m}{z} = 105$ / cts · s	Sensitivity Ratio
BEH-PPV:PS1 1:1	1054858	539415	3.911
BEH-PPV:PS1 1:3	979758	1189688	3.294
BEH-PPV:PS1 1:9	702524	2163764	3.246

($\frac{m}{z} = 105$) over the first layer. Ideally, the integral ratio should match the individual mean weight ratios for each blend, i.e. 1:1, 1:3, 1:9, respectively.

Unfortunately, all signals have their own absolute sensitivity in the mass spectrogram, therefore the quantitative comparison cannot be done straightforward like that. Instead, a relative sensitivity can be calculated taking the initial ratio into account. Such a calculation was done in table 4.2 in the last column. The sensitivity for a $\frac{m}{z} = 43$ (the BEH-PPV fragment) is approximately 3.5 times higher than for $\frac{m}{z} = 105$ (the styrene unit).

Having calculated the relative sensitivity factor for each blend we can calculate the BEH-PPV to PS1 ratio across the blend layer (as a function of sputter time). An error for the composition can be calculated by taking the variation of the sensitivity factor into account. The results can be found in figure 4.10. Figure 4.10 (a) shows the 1:1 blend layer composition as a function of sputter time. The red line marks the individual mean weight ratio. Figure 4.10 (b) and (c) show analogue results for the 1:3 and 1:9 blends. All three plots show in common, that the BEH-PPV fraction is high close to the top of the layer, where in a hole only device the MoO_3-contact is used to inject holes.

After roughly 30 seconds of sputter time the BEH-PPV fraction drops below the mean weight ratio and the PS1 fraction dominates the composition. In figure 4.10 (b) and (c) the fraction of BEH-PPV drops significantly below 10 %, for the 1:9 blend even below 5 %.

Figure 4.11 (a) shows the sputter rate as a function of PS1 fraction in the blend layer. As the PS1 fraction increases the sputter rate linearly rises from a value of 0.8 nm/sec for the pristine BEH-PPV layer to 2.666 nm/sec for the 1:9 BEH-PPV:PS1 blend layer. By linearly drawing the trend line to a virtual PS1 fraction to 100 % we can estimate the sputter rate of 2.875 nm/sec for a pristine PS1 layer. The latter estimation has to be done, because a spin cast PS1 shows strong dewetting effects and a closed layer is not achievable under practical conditions. Taking the depth profiles in figure 4.9 into account, a construction of the effective layer order is possible. Similar findings were made in Ribeiro et al. [65]. Figure 4.11 (b) shows that except for the pristine BEH-PPV all blend based layers contain a PS1-rich interlayer at the interface with PEDOT:PSS. Moreover, the higher the fraction of PS1 in the initial blend the thicker the PS1-rich interlayer gets.

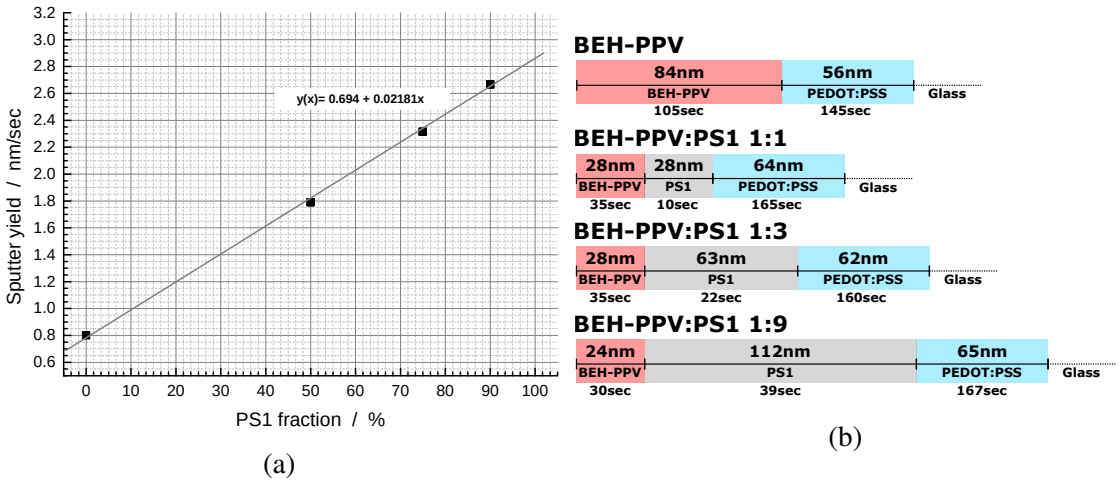

(a) (b)

Fig. 4.11 In (a) sputter rate is plotted as a function of PS1 fraction in the blend layer. A linear fit is applied to estimate the sputter rate for a pure PS1 layer (result in table 4.1). When spin casting PS1 from solution strong dewetting occurs and no closed film is achievable. In (b) a scheme of the layer order is shown as a function of depth or sputter time.

We identified the presence of an insulating PS1-rich interlayer between a BEH-PPV-rich layer and PEDOT:PSS for all blend based devices. Furthermore, we identified possible chemical fragments of each polymer layer in ToF-SIMS analysis as shown in figure 4.9 (e). Injection of holes from the MoO_3 contact follows the *JV* characteristics of an ohmic contact (see fig. 4.2 and only linearly decreases with increasing PS1 fraction in the blend with BEH-PPV. This coincides with the findings made with ToF-SIMS depth profile analysis. All three BEH-PPV:PS1 blends show a BEH-PPV-rich composition close to the air interface, where the MoO_3 contact is typically used as injection contact in HO devices. With further ToF-SIMS analysis closer to the PEDOT:PSS interface, the composition changes to a PS1 dominated state, with fractions of 95 % PS1 and higher for the 1:9 blend. As a result, injection of holes is getting difficult to achieve. The depleting fraction of BEH-PPV results in a low amount of HOMO states the PEDOT:PSS contact can inject holes into. To our understanding this interlayer is the source of the massive hole injection problems as observed in figure 4.2 (b) and acts like a physical barrier for charge injection from the PEDOT:PSS contact. Additionally, percolation pathways for positive charge carriers are almost absent in the PS1-rich interlayer, which results in very bad HO-device performance. The second hypothesis stated in the introduction section of this chapter to our understanding is strongly proven with these findings.

In contrast to HO-devices, EO-devices do not suffer in performance with increased PS1 fraction in the blend layer, it even improves dramatically, as already expected from the previously reported trap dilution effect (see chapter 3). Injection of electrons happens at the

Barium/Aluminum electrode capped "air"-blend interface. No interface to a PEDOT:PSS contact is present for EO-devices. Instead, electrons are extracted at the slightly oxidized aluminum bottom anode contact.

4.3.3 Changing hole injection properties by fluorination with perfluorooctane sulfonic acid

In order to avoid stratification (vertical segregation) in a BEH-PPV:PS1 blend layer, we try to modify the PEDOT:PSS hole injection layer. More specifically, we try to modify the surface energy of the PEDOT:PSS layer in such a way that accumulation of polystyrene at the PEDOT:PSS interface when spin casting a BEH-PPV:PS:chlorobenzene solution on top of it is inhibited or even avoided. Howells et al. mention a method to modify the PEDOT:PSS contact by fluorination with various anionic fluorinated materials, such as perfluorooctane sulfonic acid (FOS) or perfluorinated polymeric ionomers (PFI) in order to increase the work function of the contact and lower the surface energy [27] of PEDOT:PSS. The perfluorinated compound is mixed in excess into PEDOT:PSS with a ratio of 1:6:30 PEDOT:PSS:FOS. Despite the increased fraction of insulating agents, they report superior OPV device performance and see no negative effect on charge transport properties. In the next subsection we want to evaluate the influence of FOS on the segregation behavior of a BEH-PPV:PS1 polymer blend spin cast on top of PEDOT:PSS:FOS.

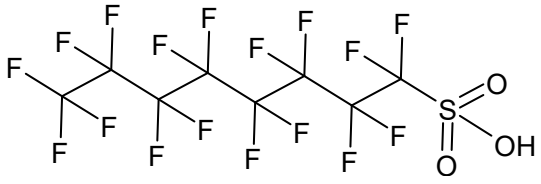

Fig. 4.12 Chemical structure of perfluorooctane sulfonic acid.

In [27] Howells et al. report a great improvement of overall device performance by fluorination of PEDOT:PSS with perfluorooctane sulfonic acid (see chemical structure in figure 4.12). Despite the environmental risk the compound brings, it is still of high interest to investigate the potential influence on PEDOT:PSS properties. On PEDOT:PSS as used in standard application we observed incomplete surface directed vertical phase demixing (incomplete stratification), identified by ToF-SIMS analysis. The accumulation of PS1 at the interface between the BEH-PPV:PS1 and PEDOT:PSS led to a dramatic decrease of charge injection in HO-devices as seen in figure 4.2 (b). With the addition of FOS into PEDOT:PSS we intend to avoid the accumulation of PS1 into a PS1-rich interlayer at the

interface to PEDOT:PSS:FOS as shown in figure 4.13 and as such to establish an improved contact between the HTL and the BEH-PPV:PS1 blend.

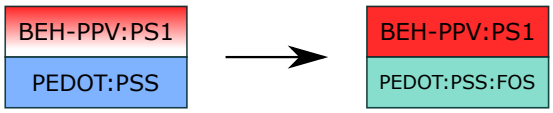

Fig. 4.13 Desired change of BEH-PPV:PS1 blend morphology by introducing FOS into the underlying PEDOT:PSS layer. Red regions are high in BEH-PPV content and white regions are high in PS1 content.

We first want to try to replicate the reported work function change of PEDOT:PSS when fluorinated with FOS. Therefore a measurement of the macroscopic W was done with a Kelvin-Probe setup. For completeness, we compare it to the already measured work function of PEDOT:PSS in figure 4.5, which equals to a value of 5.07 eV.

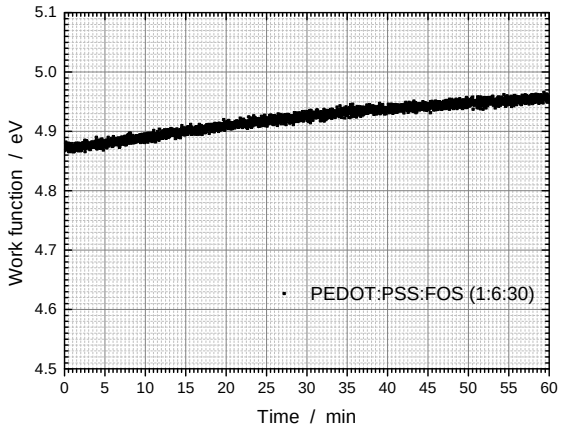

Fig. 4.14 The work function of a freshly prepared PEDOT:PSS:FOS layer in the ratio 1:6:30 is measured versus measurement time.

Figure 4.14 demonstrates the acquired work function of PEDOT:PSS:FOS 1:6:30 as a function of measurement time. In direct contrast to the reported values (approx. 5.7 eV) by Howells et al., we observed a much lower W_{FOS} at around 4.87 eV that increased to a value of 4.96 eV after 60 min of measurement time. This is somewhat surprising, as we had expected an overall increase of the work function by fluorination in the same manner. However, in this study we want to investigate the chemical influence on surface directed phase dynamics and explicitly do not expect to have increased charge injection limitations even with work function values around 4.9 eV for PEDOT:PSS:FOS. The perfluorooctane sulfonic acid, typically used as repelling surfactant, drastically changes surface properties and exhibits chemical orthogonality to almost any other compound. This gives the opportunity to

avoid compositional changes in polymer blends caused by surface driven attraction of one of the blend components, exemplary seen for the reported BEH-PPV:PS1 blend.

The easiest way to investigate the influence of surface functionalization through FOS in this case is to built hole only devices based on the fluorinated PEDOT:PSS (PEDOT:PSS:FOS 1:6:30) and compare those to reference hole only devices with the standard PEDOT:PSS contact. The fluorination would have direct influence on the current voltage characteristics as the composition of the blend would change drastically. In figure 4.15 current density versus voltage characteristics of these devices are displayed. The black line denotes a

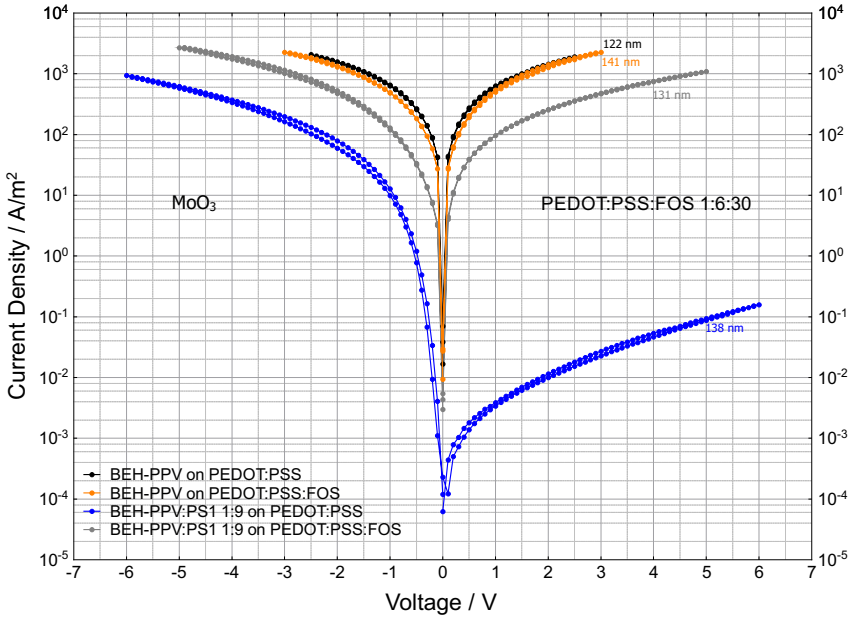

Fig. 4.15 Comparison of current density versus applied voltage of BEH-PPV and BEH-PPV:PS1 1:9 blend hole only devices on PEDOT:PSS (black and blue) and on PEDOT:PSS:FOS (orange and grey).

pristine BEH-PPV PEDOT:PSS based hole only device, the orange line represents the JV-characteristics of a BEH-PPV PEDOT:PSS:FOS based HO device. The blue and grey curves are JV-characteristics of BEH-PPV:PS1 1:9 blend based HO devices with standard and fluorinated PEDOT:PSS, respectively. The pristine BEH-PPV HO devices show almost no difference between the fluorinated and non-fluorinated contact giving a generally high current density in the 10^3 A/m^2 range at elevated voltages. The BEH-PPV:PS1 1:9 PEDOT:PSS based HO device (blue) shows asymmetry of about 10^4 A/m^2 between the MoO_3 and PEDOT:PSS contact, due to the PS1-rich barrier interlayer at the PEDOT:PSS contact. At the MoO_3 contact ohmic injection of holes due to the BEH-PPV-rich interlayer is possible and results in current densities of about 10^3 A/m^2 at 6 V. In direct contrast to this, only very

small asymmetry is observed for the PEDOT:PSS:FOS based BEH-PPV:PS1 1:9 HO device. The current density values reach high values at around 10^3 A/m^2 and higher at elevated voltages. We interpret this increase in current density and the absence of strong asymmetry as a result of improved and homogeneous composition of the subsequently spin cast blend layer. Ultimately, the excess addition of FOS into the PEDOT:PSS contact improves device performance of HO device drastically. This result gives room for future investigation on alternative compounds that finally lead to improved charge transport properties of polymer blend based semi conducting devices such as OLEDs, OPVs and OFETs.

4.4 Conclusions & Outlook

In this chapter we demonstrated that it is of high importance to investigate the phase dynamics of polymer blends when using them in electrical devices such as PLED. Charge injection may be limited by many different sources. At first we assumed a misalignment of the $W_{PEDOT:PSS}$ with the HOMO level of BEH-PPV in a BEH-PPV:PS blend, when PEDOT:PSS is treated with common organic solvent, such as in regular solution casting. This hypothesis could be falsified by Kelvin-Probe measurements. The change in work function of PEDOT:PSS by treatment with organic solvents, like chlorobenzene, chloroform or toluene, is smaller than initially assumed. As a consequence, we investigated the bulk phase composition of the BEH-PPV:PS1 blend with the help of ToF-SIMS analysis. More particularly, we pointed out that PS1 accumulates at the interface with PEDOT:PSS, which, to our understanding, originates from a surface driven interaction. Polystyrene seems to favor the vicinity of the PEDOT:PSS surface over the air interface, which in return drives the blend during solution processing into a layer with a compositional gradient along the vertical axis. The accumulation of polystyrene at the PEDOT:PSS interface limits the occurrence of percolation pathways through the blend layer and limits positive charge carrier injection into the blend layer. In earlier studies we have seen that for PPV:insulator blend based electrical devices electron trapping is massively reduced, when both components are intimately mixed. Due to the found vertical composition gradient, demonstration of similar results for the shown BEH-PPV:PS1 blend is somewhat more demanding. To address for that, we modified the surface properties of PEDOT:PSS by addition of FOS in excess. Hole-only devices made from BEH-PPV:PS1 blends on top of PEDOT:PSS:FOS as hole injection contact massively improved in performance. Thus, current densities values in these devices were almost as high as for pristine BEH-PPV/PEDOT:PSS based HO devices and four orders of magnitude higher than before.

Despite the delicate handling of perfluorooctane sulfonic acid, the outcome of the findings may be a valid approach to tune phase composition through modification of the surface properties of PEDOT:PSS to drive more polymer blends into a phase regime of intimate mixing during solution casting and to achieve trap reduction.

Chapter 5

Influence of chain end density on electron transport behavior in BEH-PPV

This chapter contains contributions from Schönbein, A., Michels, J.J. and Blom, P.W.M..

5.1 Introduction

Charge transport in organic semiconductors nowadays is well understood. Different models exist that describe the transport behavior of charges in polymeric semiconductors. One prominent model is the Extended Gaussian Disorder Model (EGDM), which was derived from the Gaussian Disorder model introduced by Bässler in 1993. The model from 1993 included the field dependency of charge transport in disordered semiconductors and extended the space charge limited current originally described by Mott and Gurney [56], see 2.1 for further information on the SCLC. Additionally, the EGDM introduced the charge density dependency [62] of the charge carrier mobility. Charge transport, independent from charge carrier, can be sufficiently well described with this model and was well used in the last one and a half decade. Despite the fact that charge transport is well understood, the origin of limitations for charge transport are still under high debate. Unlike electron transport, hole transport in pristine disordered polymeric semiconductors is mainly trap free and but still rather low as compared to inorganic semiconductors, due to the high degree of disorder. Limitations for charge transport originate from structural disorder and, at least equally important, from intrinsic and extrinsic impurities. Finding the origin of intrinsic impurities and defects follows logic assumptions of possible side reactions and on chain contamination during the synthesis of a semi conducting polymer. For instance, one can name remaining halogens as an on chain impurity that limits charge transport through a high affinity of

Table 5.1 BEH-PPV selection with varying polymer length

Polymer	Internal Name	$\overline{M}_w$/g/mol	$\overline{M}_n$/g/mol	D
BEH-PPV-50K	BEH-PPV-40-72	202404	52353	3.87
BEH-PPV-120K	BEH-PPV-41	798547	123772	6.45
BEH-PPV-500K	BEH-PPV-45	1840750	521300	3.53

localizing electrons on the chain. External impurities may be introduces during synthesis as well. Namely, chain ends may terminate during a radical polymerization with a radical scavenger or impurities that act similarly. These chain ends typically have a high electron affinity. For a semi conducting polymer this means a chain end is not only a conjugation break, but also an energetically deep state for charge carriers forming a trap. Additionally, impurities with high electron affinity, such as oxygen or water, or even complexes of these [80], may act as external contamination that forms as a deep energetic state called a trap and is likewise a very prominent candidate. In this chapter we want to investigate the role of chain end defects, more specifically, the density of end groups as possible candidates for limited electron transport in polymeric semiconductors. Specifically, we chose BEH-PPV in three different chain lengths ranging from a number average molar mass ($\overline{M}_n$) of 52 kg/mol over 123 kg/mol to 521 kg/mol, see table 5.1. As this polymer is synthesized in house in a radical polymerization via the Gilch route [21], we had the possibility to compare differently sized, but similarly prepared BEH-PPV polymers in a systematic study. During the radical polymerization process chain ends may get terminated with aldehyde groups that are known to have high electron affinity. We hypothesize that those aldehyde groups have significant influence on electron transport in the chosen BEH-PPV polymers.

5.1.1 Estimation of defect density caused by chain ends

We can estimate the expected defect density caused by chain ends. In order to do so, we take the number average molar mass $\overline{M}_n$ of each polymer and calculate in equation 5.1 the chain end density, with $\rho_{polymer}$ as the physical density of BEH-PPV, q the number of chain ends per chain and N_A as the Avogadro constant. In our example several strongly simplifying assumptions are made. First, we assume to have two chain ends on each polymer which implicates to have a linear polymer with no side branches. Second, we assume that every end group acts as an electronic defect state. Third, we ignore at this point all extrinsic impurities that might get introduced during synthesis and also act as electronic defect states. And fourth, we assume the physical density of BEH-PPV be equal to that of polystyrene with a value of 1050 $\frac{\mathrm{kg}}{\mathrm{mol}}$.

Table 5.2 Estimation of chain end densities for the chosen BEH-PPV polymers

Polymer	$\overline{M}_n$ / g/mol	N_{ends} / m^{-3}
BEH-PPV-50K	52353	$2.42 \cdot 10^{25}$
BEH-PPV-120K	123772	$1.02 \cdot 10^{25}$
BEH-PPV-500K	521300	$2.43 \cdot 10^{24}$

$$N_{ends} = \frac{\rho_{polymer} \cdot q}{\overline{M}_n} \cdot N_A \tag{5.1}$$

With the values given in table 5.1 the calculated chain end densities N_{ends} are given in table 5.2.

As already seen by $\overline{M}_n$ the amount of end groups reduces with increasing polymer length. The calculated end group density for BEH-PPV-50K increases almost tenfold compared to BEH-PPV-500K. Effectively, a tenfold increase of chain ends should have a significant influence on charge transport, assuming the chain ends to be electron trapping sites.

5.2 Experimental

The polymers poly(2,5-bis(2'-ethylhexyloxy)-1,4-phenylene vinylene) (BEH-PPV) were synthesized in house via the Gilch route [21]. The reaction follows a radical polymerization via a halogen-p-quinodimethan intermediate in THF as solvent and potassium-*tert*-butanolate as the reaction base. More details on the kinetics of the reaction can be found in the paper of Schönbein et al. [68]. All molecular weights were measured against polystyrene standards in the in house gel permeation chromatography setup.

Device preparation was done under nitrogen protected glove box atmosphere. For hole only device preparation pre-patterned ITO-glass substrates were cleaned in neutral soap, ultrasonicated in acetone and isopropanol and subsequently rinsed in de-ionized water. To finalize the cleaning procedure, the substrates were dried and activated in a UV/Ozone oven. After activation, PEDOT:PSS (Heraeus Clevios P VP 4083) was spin cast from aqueous solution to yield a roughly 65 nm thick hole injection layer. BEH-PPV was spin cast on top of the PEDOT:PSS layer from chlorobenzene solution to yield a layer at around 100 nm thickness (exact thicknesses are given in the Results & Discussion section). In order to complete HO device preparation, deep work function MoO_3 contacts (10 nm) were evaporated at a base pressure of approximately 10^{-7} mbar from a thermal boat. A 100 nm

thick aluminum protection and connection layer was evaporated subsequently on top of the MoO_3 contact. Electron only (EO) device preparation was done similarly. Aluminum bottom contacts were evaporated on cleaned glass substrates through a shadow mask. The substrates were oxidized for 10 min under ambient atmosphere to form the natural Al_2O_3 layer. BEH-PPV was spin cast successively on top. A low work function material, barium was evaporated through a shadow mask to form the top injection contact. And finally aluminum was evaporated on top to protect the barium contacts from fast oxidation.

5.3 Results and Discussion

Charge transport for holes and electrons in principle is considered to be equal [13]. The huge difference in JV-characteristics for holes and electrons originates from the presence of shallow and deep trap states within the energetic band gap of the material. The traps limit electron transport severely, where electron transport scales with V^6 and is several orders of magnitude lower than the hole transport. When all electron traps are filled, like in doped systems, or in field effect transistors, where charge densities are considerably higher than in diodes, electron and hole migration is equal. Effectively this means, when we analyze charge transport for electrons, we can use the transport characteristics of holes and add trap states to the same in order to model electron transport. This is the procedure we start our investigation. As a first step we study the charge transport properties in BEH-PPV hole only devices, see subsection 5.3.1 and extend the results to electron only device modelling, see subsection 5.3.2.

5.3.1 Modelling of Hole only devices with the Extended Gaussian Disorder Model

In figure 5.2 we demonstrate the JV-characteristics of HO devices made from (a) BEH-PPV-50K, (b) BEH-PPV-120K and (c) BEH-PPV-500K polymer. Experimentally measured values for the current densities are given as points and simulated values are shown in solid lines. The different colored plots stand for different temperatures. The simulated lines are calculated using the EGDM model proposed by Pasveer et al. [62]. All three polymers have very similar hole transport characteristics, as the hole transport in BEH-PPV is not known to be limited by charge trapping. We note, all three polymers have a lattice constant at around 1.4 nm. The width of the Gaussian distribution of transport states is equal for all three polymers at $\sigma = 0.1$ eV. For polymeric semiconductors such a low σ is interpreted as relatively low disorder compared to other polymers of the same class, to name a few: MEH-PPV,

CN-PPV, MDMO-PPV. The low disorder can be explained with the chemical structure, that is a symmetrically substituted semiconducting backbone of poly(phenylenevinylene) chain with ethylhexyloxy side chains (figure 5.1).

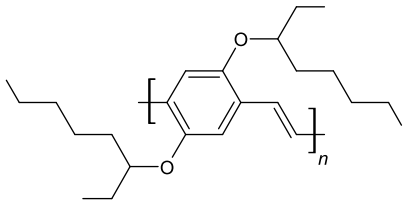

Fig. 5.1 Chemical structure of BEH-PPV.

The structural symmetry allows for comparably good alignment of the molecules and therefore improved hopping of electrons between conjugated sites. The overall benefit is a reduced turn on voltage in PLEDs and higher mobility in FETs.

The hole mobilities of all three polymers are in the same order of magnitude, which means that charge transport is equally good in all of them. The mobility for BEH-PPV-50K is slightly lower at a value of $1.08 \cdot 10^{-9} \frac{\mathrm{m}^2}{\mathrm{Vs}}$ than for the other two polymers, which range at $3.5 \cdot 10^{-9} \frac{\mathrm{m}^2}{\mathrm{Vs}}$ and $4.1 \cdot 10^{-9} \frac{\mathrm{m}^2}{\mathrm{Vs}}$, respectively. This phenomenon can be explained with a higher disorder that may be introduced during preparation of the polymeric thin film. These values are strongly supported by values reported in the literature by Tanase et al. [77]. For the room temperature simulation (black) we see a deviation from the simulated curve. This phenomenon occurs when the devices sees high current densities. In that regime of the device we measure the series resistance of the contacts that limit the device performance. At lower temperature this effect is strongly reduced and the characteristics of the BEH-PPV thin film dominates the current density values again. We can use the results of hole transport characteristics to model electron transport and investigate the density of trapping sites to ultimately compare the trap density N_t with the end group density N_{ends}.

5.3.2 Modelling of Electron only devices with the Extended Gaussian Disorder Model

Hereafter, the current density versus voltage plots for electron only devices made of the three different polymers are plotted. The EO devices are scanned iteratively to higher voltages as on the back scan deep trap states are scanned instead of the real electron transport. In order to model the transport characteristics of electron only devices we need to take the envelope of all scans as the JV curve and model this behavior. The experimental results are shown in dots, whereas the simulation is shown as a solid black line for each EO device.

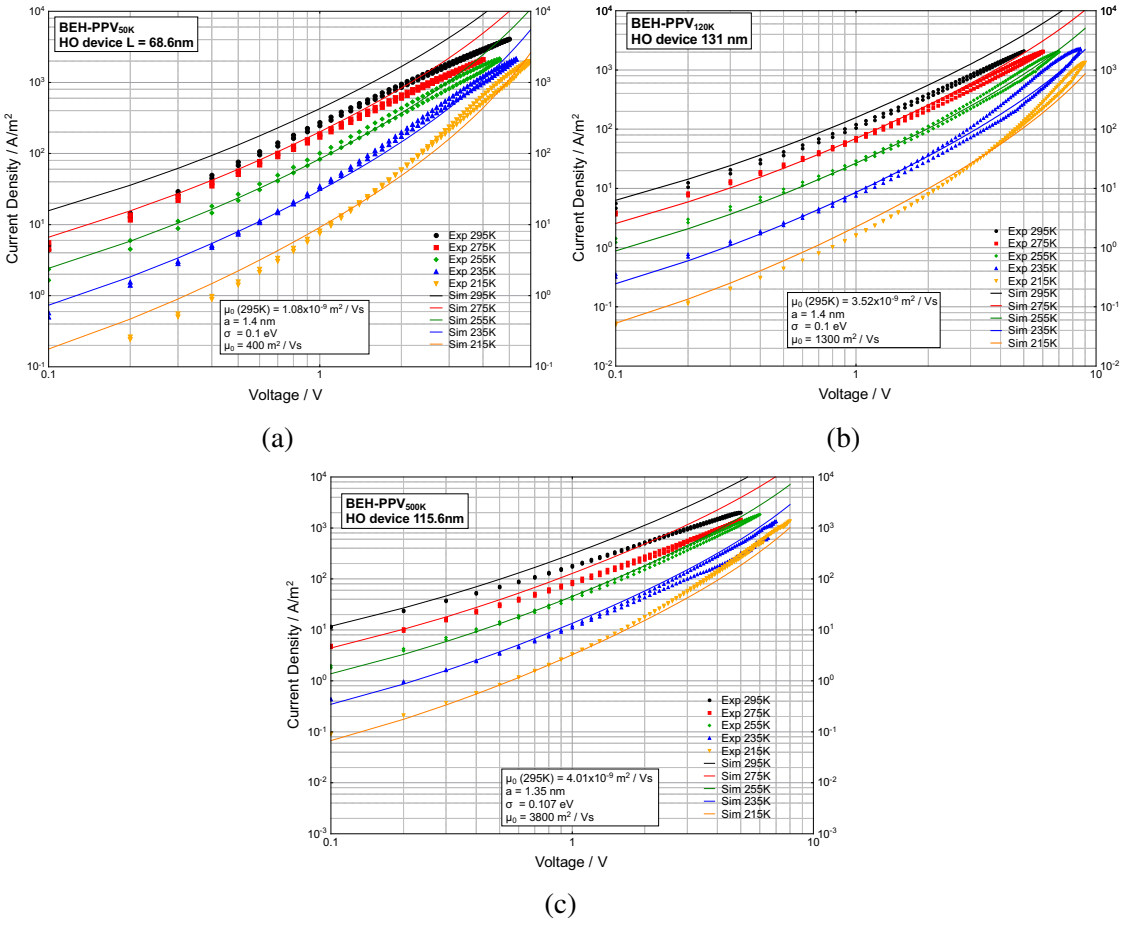

Fig. 5.2 Experimental and (EGDM) modelled hole transport behavior of BEH-PPV with (a) $M_n = 52$ kg/mol, (b) $M_n = 123$ kg/mol and (c) $M_n = 521$ kg/mol at five different temperatures.

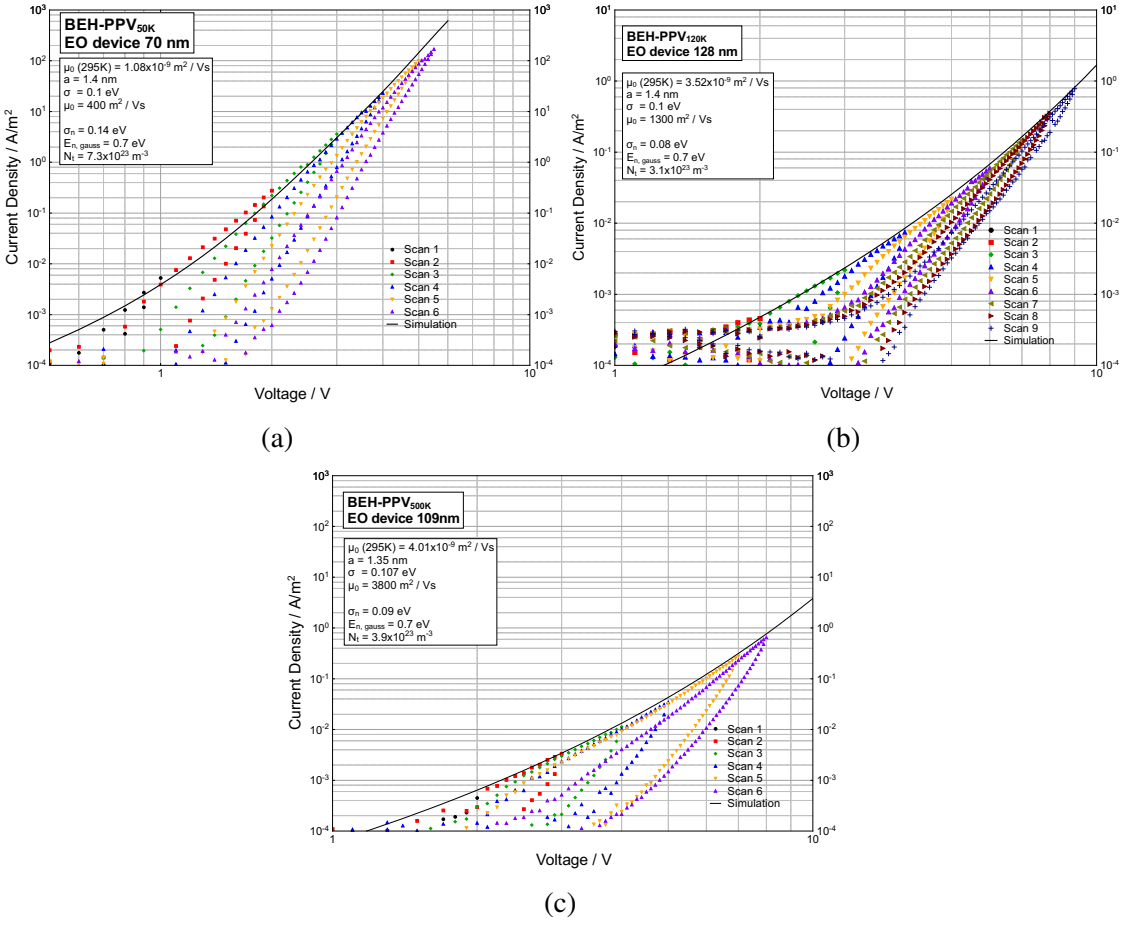

Fig. 5.3 Experimental and (EGDM) modelled electron transport behavior of BEH-PPV with (a) $M_n = 52$ kg/mol, (b) $M_n = 123$ kg/mol and (c) $M_n = 521$ kg/mol.

The electron trapping behavior is modelled with a constant trap depth at 0.7 eV below the LUMO level of the polymer. BEH-PPV-120K and BEH-PPV-500K show no significant difference between each other. Both have a narrow width of Gaussian distributed electron traps, $\sigma = 0.08$ eV and $\sigma = 0.09$ eV respectively. The density of trap states equals to $3.1 \cdot 10^{23}$ m^{-3} and $3.9 \cdot 10^{23}$ m^{-3}, respectively. Comprehensively, BEH-PPV-120K and BEH-PPV-500K do not differ from each other significantly and have almost the same transport characteristics. BEH-PPV-50K shows a higher width $\sigma = 0.13$ eV and increased trap density of $7.3 \cdot 10^{23}$ m^{-3}. Again, in our point of view the latter behavior cannot be correlated to increased amount of chain ends, but rather to a different preparation history due to lower viscosity. Also here, trap depth and Gaussian distribution lies within previously reported values [40] for BEH-PPV.

5.3.3 Comparison between chain end density and trap density

From the results shown in sections 5.3.1 and 5.3.2 we cannot conclude a significant influence of chain end density to trapping characteristics. We can see that the lower molecular weight BEH-PPV-50K has slightly differing charge transport characteristics as compared to BEH-PPV-120K and BEH-PPV-500K, but all investigated values lie within previously reported values.

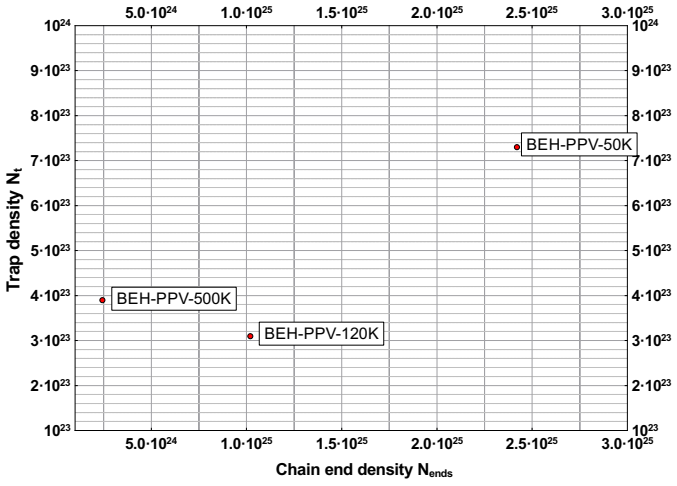

Fig. 5.4 Electron trap density N_t plotted against polymer chain end density N_{ends}.

In figure 5.4 we compare the chain end density N_{ends} with the electron trap density N_t. To our opinion we cannot see any correlation between both values for all three compared polymers and conclude that though chain end densities lie within a range of 10^{25} m^{-3} the trap density is two orders of magnitude lower. Experimentally, we falsified the initially stated

hypothesis that chain ends have a significant influence on charge transport behavior in PPV based semiconductors. The origin of trap states might rather be due to external impurities introduced during the synthesis of the polymers, such as the proposed oxygen water complex mentioned by Tseng et al. [80].

5.4 Conclusions

In this work, no significant relation between polymer molecular weight (M_n and M_w) and electron trap density could be found. The reason might be the limited availability molecular weights of BEH-PPV polymers. But more likely, the chain end density does not play a significant role as compared to external impurities such as the proposed oxygen water complex, that is introduced unintentionally during synthesis of the polymer. From preparation point of view we recommend to synthesize rather short functional polymers in the range of 100 kg/mol. The low viscosity of such polymers and therefore easier handling is beneficial for device preparation. Also during synthesis, chain length control is easier for shorter polymers as well as subsequent purification.

References

[1] Abbaszadeh, D., Kunz, A., Wetzelaer, G. A. H., Michels, J. J., Craciun, N. I., Koynov, K., Lieberwirth, I., and Blom, P. W. M. (2016). Elimination of charge carrier trapping in diluted semiconductors. *Nature Materials*, 15(6):628–633.

[2] Abbaszadeh, D., Wetzelaer, G. A. H., Nicolai, H. T., and Blom, P. W. M. (2014). Exciton quenching at PEDOT:PSS anode in polymer blue-light-emitting diodes. *J. Appl. Phys.*, 116(22):224508.

[3] ACD (2017). Calculated using ACD ChemLab Freeware.

[4] Barton, A. (2017). *CRC Handbook of Solubility Parameters and Other Cohesion Parameters: Second Edition*. CRC Press.

[5] Bässler, H. (1993). Charge transport in disordered organic photoconductors a monte carlo simulation study. *physica status solidi (b)*, 175(1):15–56.

[6] Bernanose, A. and Marquet, G. (1954). Électroluminescence du carbazol par les champs électriques alternatifs ; caractérisation de l'électrophotoluminescence organique. *Journal de Chimie Physique*, 51:255 – 259.

[7] Blom, P. W. M., de Jong, M. J. M., and Vleggaar, J. J. M. (1996). Electron and hole transport in poly(p-phenylene vinylene) devices. *Appl. Phys. Lett.*, 68(23):3308.

[8] Brazovskii, S., Kirova, N., and Matveenko, S. (1984). The peierls effect in conducting polymers. *Zhurnal Eksperimental'noi i Teoreticheskoi Fiziki*, 86:743–757.

[9] Brédas, J.-L., Beljonne, D., Coropceanu, V., and Cornil, J. (2004). Charge-transfer and energy-transfer processes in π-conjugated oligomers and polymers: A molecular picture. *Chemical Reviews*, 104(11):4971–5004. PMID: 15535639.

[10] Burroughes, J. H., Bradley, D. D. C., Brown, A. R., Marks, R. N., Mackay, K., Friend, R. H., Burns, P. L., and Holmes, A. B. (1990). Light-emitting diodes based on conjugated polymers. *Nature*, 347(6293):539–541.

[11] Campbell, A. J., Bradley, D. D. C., and Antoniadis, H. (2001). Quantifying the efficiency of electrodes for positive carrier injection into poly(9,9-dioctylfluorene) and representative copolymers. *J. Appl. Phys.*, 89(6):3343.

[12] Campbell, I. H., Hagler, T. W., Smith, D. L., and Ferraris, J. P. (1996). Direct measurement of conjugated polymer electronic excitation energies using metal/polymer/metal structures. *Phys. Rev. Lett.*, 76(11):1900–1903.

[13] Chua, L.-L., Zaumseil, J., Chang, J.-F., Ou, E. C.-W., Ho, P. K.-H., Sirringhaus, H., and Friend, R. H. (2005). General observation of n-type field-effect behaviour in organic semiconductors. *Nature*, 434(7030):194–199.

[14] Conwell, E. M. (1956). Impurity band conduction in germanium and silicon. *Phys. Rev.*, 103:51–61.

[15] Cossiello, R. F., Akcelrud, L., and Atvars, T. D. Z. (2005). Solvent and molecular weight effects on fluorescence emission of meh-ppv. *Journal of the Brazilian Chemical Society*, 16(1):74–86.

[16] Craciun, N. I., Zhang, Y., Palmaerts, A., Nicolai, H. T., Kuik, M., Kist, R. J. P., Wetzelaer, G. A. H., Wildeman, J., Vandenbergh, J., Lutsen, L., Vanderzande, D., and Blom, P. W. M. (2010). Hysteresis-free electron currents in poly(p-phenylene vinylene) derivatives. *Journal of Applied Physics*, 107(12):124504.

[17] Emerson, J. A., Toolan, D. T. W., Howse, J. R., Furst, E. M., and Epps, T. H. (2013). Determination of solvent–polymer and polymer–polymer flory–huggins interaction parameters for poly(3-hexylthiophene) via solvent vapor swelling. *Macromolecules*, 46(16):6533–6540.

[18] Flory, P. (1953). *Principles of Polymer Chemistry*. Baker lectures 1948. Cornell University Press: Ithaca.

[19] Flory, P. J. (1942). Thermodynamics of high polymer solutions. *The Journal of Chemical Physics*, 10(1):51–61.

[20] Gartstein, Y. N. and Conwell, E. M. (1995). High-field hopping mobility in molecular systems with spatially correlated energetic disorder. *Chemical Physics Letters*, 245(4):351–358.

[21] Gilch, H. G. and Wheelwright, W. L. (1966). Polymerization of α-halogenated p-xylenes with base. *Journal of Polymer Science Part A-1: Polymer Chemistry*, 4(6):1337–1349.

[22] Gong, X., Wang, S., Moses, D., Bazan, G. C., and Heeger, A. J. (2005). Multilayer polymer light-emitting diodes: White-light emission with high efficiency. *Advanced Materials*, 17(17):2053–2058.

[23] Graessley, W. W., Krishnamoorti, R., Reichart, G. C., Balsara, N. P., Fetters, L. J., and Lohse, D. J. (1995). Regular and irregular mixing in blends of saturated hydrocarbon polymers. *Macromolecules*, 28(4):1260–1270.

[24] Hall, R. N. (1952). Electron-hole recombination in germanium. *Phys. Rev.*, 87:387–387.

[25] Hansen, C. (1999). *Hansen Solubility Parameters, a User's Handbook*. CRC Press New York.

[26] Hansen, W. N. and Hansen, G. J. (2001). Standard reference surfaces for work function measurements in air. *Surface Science*, 481(1):172 – 184.

[27] Howells, C. T., Marbou, K., Kim, H., Lee, K. J., Heinrich, B., Kim, S. J., Nakao, A., Aoyama, T., Furukawa, S., Kim, J.-H., Kim, E., Mathevet, F., Mery, S., Samuel, I. D. W., Al Ghaferi, A., Dahlem, M. S., Uchiyama, M., Kim, S. Y., Wu, J. W., Ribierre, J.-C., Adachi, C., Kim, D.-W., and André, P. (2016). Enhanced organic solar cells efficiency through electronic and electro-optic effects resulting from charge transfers in polymer hole transport blends. *J. Mater. Chem. A*, 4:4252–4263.

[28] Hu, W. (2012). *Polymer physics: a molecular approach*. Springer Science & Business Media.

[29] Huggins, M. L. (1942). Thermodynamic properties of solutions of long-chain compounds. *Annals of the New York Academy of Sciences*, 43(1):1–32.

[30] Hwang, W. and Kao, K. C. (1972). A unified approach to the theory of current injection in solids with traps uniformly and non-uniformly distributed in space and in energy, and size effects in anthracene films. *Solid-State Electronics*, 15(5):523–529.

[31] J. Brandrup, Edmund H. Immergut, E. A. G., editor (1999). *Polymer Handbook*. Wiley, 4th edition.

[32] Jones, R. A. L. (1999). *Polymers at surfaces and interfaces*. Cambridge University Press.

[33] Jones, R. A. L., Norton, L. J., Kramer, E. J., Bates, F. S., and Wiltzius, P. (1991). Surface-directed spinodal decomposition. *Phys. Rev. Lett.*, 66:1326–1329.

[34] Kasparek, C. and Blom, P. W. M. (2017). Solution-processed multilayer polymer light-emitting diode without intermixing. *Applied Physics Letters*, 110(2):023302.

[35] Kasparek, C., Rohloff, R., Michels, J. J., Crăciun, N. I., Wildeman, J., and Blom, P. W. M. (2017). Solubility and charge transport in blends of poly-dialkoxy-p -phenylene vinylene and UV-cross-linkable matrices. *Advanced Electronic Materials*, 3(5):1600519.

[36] Kasparek, C., Rörich, I., Blom, P. W. M., and Wetzelaer, G.-J. A. H. (2018). Efficiency of solution-processed multilayer polymer light-emitting diodes using charge blocking layers. *Journal of Applied Physics*, 123(2):024504.

[37] Kemerink, M., van Duren, J. K. J., Jonkheijm, P., Pasveer, W. F., Koenraad, P. M., Janssen, R. A. J., Salemink, H. W. M., and Wolter, J. H. (2003). Relating substitution to single-chain conformation and aggregation in poly(p-phenylene vinylene) films. *Nano Letters*, 3(9):1191–1196.

[38] Kouijzer, S., Michels, J. J., van den Berg, M., Gevaerts, V. S., Turbiez, M., Wienk, M. M., and Janssen, R. A. J. (2013). Predicting morphologies of solution processed polymer:fullerene blends. *Journal of the American Chemical Society*, 135(32):12057–12067.

[39] Kubo, K. and Ogino, K. (1971). Osmotic pressures of polystyrene, poly-p-chlorostyrene and poly-o-chlorostyrene solutions. *Bulletin of the Chemical Society of Japan*, 44(4):997–1000.

[40] Kuik, M., Koster, L., Dijkstra, A., Wetzelaer, G., and Blom, P. (2012). Non-radiative recombination losses in polymer light-emitting diodes. *Organic Electronics*, 13(6):969–974.

[41] Kunz, A., Blom, P. W. M., and Michels, J. J. (2017). Charge carrier trapping controlled by polymer blend phase dynamics. *J. Mater. Chem. C*, 5:3042–3048.

[42] Lampert, M. A. (1956). Simplified theory of space-charge-limited currents in an insulator with traps. *Phys. Rev.*, 103:1648–1656.

[43] Langevin, P. (1903). Recombinaison et mobilites des ions dans les gaz. *Ann. Chim. Phys*, 28(433):122.

[44] Lechner, M., Gehrke, K., and Nordmeier, E. (2014). *Makromolekulare Chemie: Ein Lehrbuch für Chemiker, Physiker, Materialwissenschaftler und Verfahrenstechniker*. Springer Berlin Heidelberg.

[45] Lu, L., Zheng, T., Wu, Q., Schneider, A. M., Zhao, D., and Yu, L. (2015). Recent advances in bulk heterojunction polymer solar cells. *Chemical Reviews*, 115(23):12666–12731. PMID: 26252903.

[46] Maranas, J. K., Mondello, M., , Grest, G. S., Kumar, S. K., Debenedetti, P. G., , and Graessley*, W. W. (1998). Liquid structure, thermodynamics, and mixing behavior of saturated hydrocarbon polymers. 1. cohesive energy density and internal pressure. *Macromolecules*, 31(20):6991–6997.

[47] Mark, P. and Helfrich, W. (1962). Space-charge-limited currents in organic crystals. *Journal of Applied Physics*, 33(1):205–215.

[48] Markov, D. E., Tanase, C., Blom, P. W. M., and Wildeman, J. (2005). Simultaneous enhancement of charge transport and exciton diffusion in poly(*p*-phenylene vinylene) derivatives. *Phys. Rev. B*, 72:045217.

[49] Martens, H. C. F., Blom, P. W. M., and Schoo, H. F. M. (2000). Comparative study of hole transport in poly(p-phenylene vinylene) derivatives. *Phys. Rev. B*, 61:7489–7493.

[50] Meerholz, K. (2005). Enlightening solutions. *Nature*, 437(7057):327–328.

[51] Mette, H. and Pick, H. (1953). Elektronenleitfähigkeit von anthracen-einkristallen. *Zeitschrift für Physik*, 134(5):566–575.

[52] Michels, J. J. and Moons, E. (2013). Simulation of surface-directed phase separation in a solution-processed polymer/PCBM blend. *Macromolecules*, 46(21):8693–8701.

[53] Miller, A. and Abrahams, E. (1960). Impurity conduction at low concentrations. *Phys. Rev.*, 120:745–755.

[54] Miyaura, N. and Suzuki, A. (1995). Palladium-catalyzed cross-coupling reactions of organoboron compounds. *Chemical Reviews*, 95(7):2457–2483.

[55] Mott, N. F. (1956). On the transition to metallic conduction in semiconductors. *Canadian Journal of Physics*, 34(12A):1356–1368.

[56] Mott, N. F. and Gurney, R. W. (1940). *Electronic Processes in Ionic Crystals*. Oxford: Clarendon Press, 1st edition.

[57] Müller, M. (1999). Miscibility behavior and single chain properties in polymer blends: a bond fluctuation model study. *Macromolecular Theory and Simulations*, 8(4):343–374.

[58] Nicolai, H. T., Kuik, M., Wetzelaer, G. A. H., de Boer, B., Campbell, C., Risko, C., Brédas, J. L., and Blom, P. W. M. (2012). Unification of trap-limited electron transport in semiconducting polymers. *Nature Materials*, 11(10):882–887.

[59] Nicolai, H. T., Mandoc, M. M., and Blom, P. W. M. (2011). Electron traps in semiconducting polymers: Exponential versus Gaussian trap distribution. *Phys. Rev. B*, 83(19).

[60] Onuki, A. and Nishimori, H. (1991). Anomalously slow domain growth due to a modulus inhomogeneity in phase-separating alloys. *Phys. Rev. B*, 43:13649–13652.

[61] Paik, U., Lee, S., and Park, J.-G. (2008). Effect of physicochemical properties of solvents on microstructure of conducting polymer film for non-volatile polymer memory. *Journal of Semiconductor Technology and Science*, 8(1):46–50.

[62] Pasveer, W. F., Cottaar, J., Tanase, C., Coehoorn, R., Bobbert, P. A., Blom, P. W. M., de Leeuw, D. M., and Michels, M. A. J. (2005). Unified description of charge-carrier mobilities in disordered semiconducting polymers. *Phys. Rev. Lett.*, 94(20).

[63] Perevedentsev, A., Aksel, S., Feldman, K., Smith, P., Stavrinou, P. N., and Bradley, D. D. C. (2014). Interplay between solid state microstructure and photophysics for poly(9,9-dioctylfluorene) within oriented polyethylene hosts. *Journal of Polymer Science Part B: Polymer Physics*, 53(1):22–38.

[64] Pope, M., Kallmann, H. P., and Magnante, P. (1963). Electroluminescence in organic crystals. *The Journal of Chemical Physics*, 38(8):2042–2043.

[65] Ribeiro, A. H., Fakih, A., van der Zee, B., Veith, L., Glaser, G., Kunz, A., Landfester, K., Blom, P. W. M., and Michels, J. J. (2020). Green and stable processing of organic light-emitting diodes from aqueous nanodispersions. *J. Mater. Chem. C*, 8:6528–6535.

[66] Schaefer, C., Michels, J. J., and van der Schoot, P. (2016). Structuring of thin-film polymer mixtures upon solvent evaporation. *Macromolecules*, 49(18):6858–6870.

[67] Schlaf, R., Murata, H., and Kafafi, Z. (2001). Work function measurements on indium tin oxide films. *Journal of Electron Spectroscopy and Related Phenomena*, 120(1):149 – 154.

[68] Schönbein, A.-K., Wagner, M., Blom, P. W. M., and Michels, J. J. (2017). Quantifying the kinetics of the gilch polymerization toward alkoxy-substituted poly(p-phenylene vinylene). *Macromolecules*, 50(13):4952–4961.

[69] Scott, R. L. (1949). The thermodynamics of high polymer solutions. v. phase equilibria in the ternary system: Polymer 1—polymer 2—solvent. *The Journal of Chemical Physics*, 17(3):279–284.

[70] Shibayama, M., Stein, R. S., and Han, C. C. (1985). Study of miscibility and critical phenomena of deuterated polystyrene and hydrogenated poly(vinyl methyl ether) by small-angle neutron scattering. *Macromolecules*, 18(11):2179–2187.

[71] Shirakawa, H., Louis, E. J., MacDiarmid, A. G., Chiang, C. K., and Heeger, A. J. (1977). Synthesis of electrically conducting organic polymers: halogen derivatives of polyacetylene,(ch) x. *Journal of the Chemical Society, Chemical Communications*, (16):578–580.

[72] Shockley, W. and Read, W. T. (1952). Statistics of the recombinations of holes and electrons. *Phys. Rev.*, 87:835–842.

[73] Spreitzer, H., Becker, H., Kluge, E., Kreuder, W., Schenk, H., Demandt, R., and Schoo, H. (1998). Soluble phenyl-substituted PPVs—new materials for highly efficient polymer LEDs. *Advanced Materials*, 10(16):1340–1343.

[74] Sworakowski, J. (1970). On the origin of trapping centres in organic molecular crystals. *Molecular Crystals and Liquid Crystals*, 11(1):1–11.

[75] Tanaka, H. (2000). Viscoelastic phase separation. *Journal of Physics: Condensed Matter*, 12(15):R207–R264.

[76] Tanase, C., Meijer, E. J., Blom, P. W. M., and de Leeuw, D. M. (2003). Unification of the hole transport in polymeric field-effect transistors and light-emitting diodes. *Phys. Rev. Lett.*, 91:216601.

[77] Tanase, C., Wildeman, J., and Blom, P. W. M. (2005). Luminescent poly(p-phenylenevinylene) hole-transport layers with adjustable solubility. *Advanced Functional Materials*, 15(12):2011–2015.

[78] Tang, C. W. and VanSlyke, S. A. (1987). Organic electroluminescent diodes. *Applied Physics Letters*, 51(12):913–915.

[79] Tompa, H. (1949). Phase relationships in polymer solutions. *Transactions of the Faraday Society*, 45:1142.

[80] Tseng, H.-E., Peng, K.-Y., and Chen, S.-A. (2003). Molecular oxygen and moisture as traps in poly[2-methoxy-5-(2'-ethylhexyloxy)-1,4-phenylene vinylene]: locations and detrapping by chain relaxation. *Applied Physics Letters*, 82(23):4086–4088.

[81] van Breemen, A., Zaba, T., Khikhlovskyi, V., Michels, J., Janssen, R., Kemerink, M., and Gelinck, G. (2015). Surface directed phase separation of semiconductor ferroelectric polymer blends and their use in non-volatile memories. *Advanced Functional Materials*, 25(2):278–286.

[82] van Franeker, J. J., Westhoff, D., Turbiez, M., Wienk, M. M., Schmidt, V., and Janssen, R. A. J. (2015). Controlling the dominant length scale of liquid–liquid phase separation in spin-coated organic semiconductor films. *Advanced Functional Materials*, 25(6):855–863.

[83] Xu, Y., Peng, J., Jiang, J., Xu, W., Yang, W., and Cao, Y. (2005). Efficient white-light-emitting diodes based on polymer codoped with two phosphorescent dyes. *Applied Physics Letters*, 87(19):193502.

[84] Zhang, Y., de Boer, B., and Blom, P. W. M. (2010). Trap-free electron transport in poly(*p*-phenylene vinylene) by deactivation of traps with *n*-type doping. *Phys. Rev. B*, 81:085201.